Parameterizing isopycnal mixing via kinetic energy backscatter in an eddy-permitting ocean model

Matthew Pudig[1], Wenda Zhang[2], K. Shafer Smith[1], and Laure Zanna[1]

[1]New York University
[2]Princeton University

September 16, 2025

Abstract

Representing mesoscale turbulence in eddy-permitting ocean models raises challenges for climate simulations; in such models, eddies and their associated energy and transport effects are resolved either marginally or only over parts of the domain. Kinetic energy backscatter parameterizations have recently shown promise as both a momentum \textit{and} a buoyancy closure for partially resolved mesoscale turbulence—energizing eddies which can themselves maintain accurate large-scale stratification by slumping steep isopycnals. However, it has not been systematically explored whether such backscatter parameterizations can also serve as a closure for tracer mixing along isopycnals. Here, we present simulations using GFDL-MOM6 in an idealized basin-scale configuration to assess whether isopycnal mixing is improved, at 1/2° and 1/4° eddy-permitting resolutions, through the addition of a backscatter parameterization. We assess the representation of isopycnal mixing principally through diagnosing the three-dimensional structure of isopycnal diffusivities via a multiple tracer inversion method. Isopycnal mixing via backscatter alone shows significant improvement and closely resembles a 1/32° eddy-resolving simulation. Backscatter-parameterized mixing also outperforms simulations with no mesoscale parameterization or with an isopycnal diffusion parameterization alone, with the latter damping the tracer signature of partially resolved eddy variability. Simulations that vary the magnitude of backscatter show that increases in isopycnal diffusivities largely track increases in eddy energy. Our results suggest that parameterizing backscatter can plausibly capture key mesoscale physics in a unified framework: the inverse cascade of kinetic energy, the slumping of steep isopycnals, and the along-isopycnal mixing of tracers.

Journal of Advances in Modeling Earth Systems

RESEARCH ARTICLE

Parameterizing isopycnal mixing via kinetic energy backscatter in an eddy-permitting ocean model

Matthew P. Pudig[1], **Wenda Zhang**[3], **K. Shafer Smith**[1], **Laure Zanna**[1,2]

[1]Center for Atmosphere Ocean Science, Department of Mathematics, Courant Institute of Mathematical Sciences, New York University, New York, NY, USA [2]Center for Data Science, New York University, New York, NY, USA [3]Program in Atmospheric and Oceanic Sciences, Princeton University, Princeton, NJ, USA

Key Points:

- Eddy-permitting simulations with no mesoscale parameterization exhibit isopycnal mixing biases in a basin-scale ocean model
- Eddies energized via backscatter can generate realistic isopycnal mixing without additional isopycnal tracer diffusion
- Comparisons to traditional isopycnal tracer diffusion suggest that parameterizing backscatter is preferred in an eddy-permitting regime

Correspondence to:
Matthew Pudig,
matthew.pudig@nyu.edu

Citation:
Your citation here.

Abstract

Representing mesoscale turbulence in eddy-permitting ocean models raises challenges for climate simulations; in such models, eddies and their associated energy and transport effects are resolved either marginally or only over parts of the domain. Kinetic energy backscatter parameterizations have recently shown promise as both a momentum *and* a buoyancy closure for partially resolved mesoscale turbulence—energizing eddies which can themselves maintain accurate large-scale stratification by slumping steep isopycnals. However, it has not been systematically explored whether such backscatter parameterizations can also serve as a closure for tracer mixing along isopycnals. Here, we present simulations using GFDL-MOM6 in an idealized basin-scale configuration to assess whether isopycnal mixing is improved, at 1/2° and 1/4° eddy-permitting resolutions, through the addition of a backscatter parameterization. We assess the representation of isopycnal mixing principally through diagnosing the three-dimensional structure of isopycnal diffusivities via a multiple tracer inversion method. Isopycnal mixing via backscatter alone shows significant improvement and closely resembles a 1/32° eddy-resolving simulation. Backscatter-parameterized mixing also outperforms simulations with no mesoscale parameterization or with an isopycnal diffusion parameterization alone, with the latter damping the tracer signature of partially resolved eddy variability. Simulations that vary the magnitude of backscatter show that increases in isopycnal diffusivities largely track increases in eddy energy. Our results suggest that parameterizing backscatter can plausibly capture key mesoscale physics in a unified framework: the inverse cascade of kinetic energy, the slumping of steep isopycnals, and the along-isopycnal mixing of tracers.

Plain Language Summary

Turbulent ocean currents ("eddies") are an important component of Earth's ocean and climate system. Eddies play a major role in turbulently mixing quantities such as temperature, salinity, and oxygen along surfaces of constant density in the ocean, known as isopycnals. However, eddies are only marginally resolved by state-of-the-art numerical ocean and climate models. Marginally resolved eddies are not energetic enough, which can lead to weak large-scale currents as well as inaccurate temperature, salinity, and oxygen distributions. In this study, we show that making eddies more energetic, in a manner consistent with ocean dynamics, can improve the representation of along-isopycnal mixing in a numerical model that marginally resolves eddies. The improved along-isopycnal mixing in this model compares well to that in a high-resolution simulation where eddies are fully resolved. Our results suggest that energizing eddies may help to improve the representation of along-isopycnal mixing in more realistic global ocean and climate models.

1. Introduction

Mesoscale turbulence—with a horizontal scale of order 10–100 km, varying as a function of latitude, depth, and stratification—is a ubiquitous feature of Earth's ocean (Chelton et al., 2011; Storer et al., 2022). It plays critical roles in driving the ocean's large-scale state (e.g., J. Marshall et al., 2017; Whalen et al., 2018); setting water mass distributions (e.g., Danabasoglu et al., 1994; Thompson et al., 2014); transporting heat, salt, carbon, and other tracers (e.g., England & Rahmstorf, 1999; Resplandy et al., 2011; Gnanadesikan et al., 2015b; Stewart & Thompson, 2015; Griffies et al., 2024); and modulating ocean ecosystems (e.g., Gower et al., 1980; Lévy et al., 2015; Uchida et al., 2020; Couespel et al., 2021). As the ocean is strongly stratified in density, turbulent stirring at the mesoscale and the resultant homogenization of oceanic tracers ("mixing") occur preferentially along surfaces of constant neutral density ("isopycnal") (Iselin, 1939; Montgomery, 1940;

Abernathey et al., 2022). Isopycnal mixing is largely unresolved in coarse-resolution global ocean models (1° or coarser), as is the case for other mesoscale processes. Accounting for the net effects of these processes via parameterizations is leading order for ensuring model fidelity (Fox-Kemper et al., 2019; Hewitt et al., 2020). As modern global ocean models increasingly adopt a horizontal grid spacing that "permits" the mesoscale—that is, only marginally or only over parts of the domain—there is a pressing need to revisit the mesoscale parameterizations designed for coarse resolutions; in this "eddy-permitting" regime, these parameterizations may no longer be appropriate (e.g., Hallberg, 2013), while the absence of any parameterization may contribute to model biases (e.g., Griffies et al., 2015). In this study, we address the problem of parameterizing isopycnal mixing in such a regime.

In coarse-resolution ocean models, isopycnal mixing is typically parameterized by a rotated diffusion operator, introduced by Solomon (1971) and Redi (1982), oriented to align with local isopycnals with a prescribed isopycnal diffusion ("Redi") coefficient κ_{Redi}; this ensures mixing across isopycnals remains small thereby minimizing the "Veronis effect" (Veronis, 1975; McDougall & Church, 1986; Gough & Lin, 1995). The appropriate magnitude for κ_{Redi}, however, is poorly constrained, and differences in its magnitude have potentially significant impacts on climate-relevant simulations (e.g., Sijp & England, 2009; Gnanadesikan et al., 2013, 2015a, 2017; Jones & Abernathey, 2019; Chouksey et al., 2022). In coupled climate model simulations, varying κ_{Redi} between 400 m^2 s^{-1} and 2400 m^2 s^{-1} has been shown to induce global sea surface temperature changes of roughly 1°C and regional variations as large as 7°C (Pradal & Gnanadesikan, 2014), as well as a roughly 15% difference in the uptake of historical anthropogenic carbon (Gnanadesikan et al., 2015b). An appropriate spatial structure for κ_{Redi} may also be a source of uncertainty in coarse-resolution ocean models, where introducing three-dimensional spatial structure into κ_{Redi} has been shown to reduce tracer biases and alter the global overturning circulation (Holmes et al., 2022). Uncertainty around appropriate values for κ_{Redi} is due in part to the widely varying observational estimates for isopycnal diffusivities from tracer release experiments (Ledwell et al., 1998; Tulloch et al., 2014; Zika et al., 2020; Bisits et al., 2023), float dispersion (Lumpkin & Flament, 2001; LaCasce, 2008; Balwada et al., 2016), and satellite altimetry (Abernathey & Marshall, 2013; Klocker & Abernathey, 2014). Estimates range from local values of order 10,000 m^2 s^{-1} in energetic western boundary current regions (Cole et al., 2015) to globally averaged values of order 10 m^2 s^{-1} (Groeskamp et al., 2017). In sum, specifying an appropriate magnitude and spatial structure for isopycnal diffusion is a source of uncertainty in coarse-resolution global ocean models. Further uncertainty is introduced when ocean models adopt eddy-permitting resolutions, as it is unclear whether isopycnal diffusion remains an appropriate parameterization: should κ_{Redi} simply be scaled down as horizontal resolution is increased and eddies become more resolved (e.g., Kjellsson & Zanna, 2017; Kiss et al., 2020)? Or should the parameterization be turned off altogether once eddies are deemed sufficiently resolved (e.g., Delworth et al., 2012; Adcroft et al., 2019)? The present study instead examines a possible alternative parameterization for isopycnal mixing in the eddy-permitting regime.

The other essential effect of mesoscale turbulence parameterized at coarse resolutions is the adiabatic slumping of steep isopycnals—mimicking the unresolved restratifying effect of baroclinic instability, the primary generation mechanism for mesoscale eddies. This is typically parameterized by the Gent-McWilliams (GM) parameterization (Gent & McWilliams, 1990; Gent et al., 1995), and in coarse-resolution simulations GM is essential for maintaining accurate large-scale stratification and circulation (Danabasoglu et al., 1994; Gent, 2011). The scheme involves the prescription of a GM coefficient κ_{GM}, with units of a diffusivity, and typically the GM and Redi schemes are implemented together (Griffies, 1998), with some models making the choice that $\kappa_{\mathrm{GM}} = \kappa_{\mathrm{Redi}}$ despite theory and modeling results suggesting they should in general differ (Smith & Marshall, 2009; Abernathey et al., 2013; Vollmer & Eden, 2013). At eddy-permitting resolutions, however, it has long been recognized that GM can have unwanted effects, damping partially resolved mesoscale flows (Hallberg, 2013), although approaches to remedy this have been proposed (Mak et al., 2023).

Because of this lack of a clear path forward with the extant coarse-resolution parameterizations, an increasing amount of attention has been directed towards developing parameterizations specific to the eddy-permitting regime. In particular, when the mesoscale is marginally resolved and a viscous dissipative closure is used (generally necessary for numerical stability to ensure dissipation of enstrophy, but not energy, at the grid scale), there can exist a *spurious* depletion of resolved eddy kinetic energy (EKE) (Jansen & Held, 2014). This is due to a lack of scale separation between the eddy and viscous scales, resulting in a depletion of eddy energy close to the grid scale and thus reduced energy at all scales because of an incompletely resolved inverse cascade. One promising method to remedy this spurious energy dissipation is the use of a prognostic budget for subgrid mesoscale eddy kinetic energy (MEKE) (Cessi, 2008; Eden & Greatbatch, 2008; D. Marshall & Adcroft, 2010; Jansen et al., 2019), which can then be recycled to the resolved scales to mimic the energy "backscatter" from small to large scales associated with an inverse cascade (Jansen & Held, 2014; Jansen et al., 2015; Klöwer et al., 2018; Juricke et al., 2019; Jansen et al., 2019; Juricke et al., 2020; Yankovsky et al., 2024). Early proposals for an energy budget-based backscatter scheme employed GM concurrently, alongside the biharmonic viscous closure and a negative harmonic viscosity to represent backscatter (Jansen et al., 2019). In this case, GM served as a source for subgrid MEKE as GM models the conversion of mean available potential energy (APE) to EKE. Recent work has suggested, however, that backscatter alone can achieve both the EKE and APE effects of the unresolved mesoscale turbulence in an eddy-permitting regime (Yankovsky et al., 2024). Yankovsky et al. (2024) found specifically, using a basin-scale ocean model in an idealized configuration, that a backscatter parameterization could both sufficiently elevate resolved EKE and, through energizing eddies that then extract mean APE, relax overly steep isopycnals with GM turned off altogether. These results thus suggest that a backscatter parameterization can plausibly replace the need for GM in an eddy-permitting regime. However, they do not address whether such a backscatter parameterization also eliminates the need for an isopycnal diffusion parameterization, as suggested by Redi (1982).

The primary goal of this study is to determine whether a kinetic energy backscatter parameterization can generate sufficient isopycnal mixing, thereby eliminating the need for supplemental isopycnal diffusion, in the eddy-permitting regime. Secondary goals include evaluating whether backscatter-driven isopycnal mixing outperforms a traditional isopycnal diffusion parameterization as well as quantifying biases that arise when no mesoscale parameterization is used at these resolutions. Towards the first goal, we test the hypothesis that no supplemental isopycnal diffusion parameterization is necessary when resolved eddies are sufficiently energized via an appropriate backscatter parameterization. We test this hypothesis using an idealized adiabatic ocean model (Marques et al., 2022), designed to serve as a testbed for mesoscale parameterization, with the backscatter scheme detailed in Yankovsky et al. (2024). The results we present suggest three main conclusions when compared to a high-resolution reference simulation: (i) that eddy-permitting simulations with no mesoscale parameterization show subdued levels of isopycnal mixing and consequent biases in tracer distributions relative to the reference simulation, (ii) that a backscatter parameterization can generate realistic isopycnal mixing to match the reference simulation, and (iii) that a traditional isopycnal diffusion parameterization is largely undesirable at eddy-permitting resolutions as it damps the tracer signature of resolved eddy variability. This study thus presents a proof of concept for a mesoscale backscatter parameterization that unifies the key physics one hopes to parameterize at eddy-permitting resolutions: a well-resolved inverse cascade, the slumping of steep isopycnals, and the along-isopycnal mixing of tracers.

In section 2, we introduce the model and backscatter parameterization, and outline the method used to diagnose the three-dimensional structure of isopycnal diffusivities in simulations with this model. Section 3 evaluates the simulations, comparing 1/2° and 1/4° eddy-permitting simulations to a 1/32° eddy-resolving simulation. Section 4 concludes and discusses the results in the context of guiding parameterization development for global ocean models.

2. Methods

2.1. Model configuration

We use the GFDL Modular Ocean Model version 6 (MOM6) in the NeverWorld2 (NW2) configuration, detailed in Marques et al. (2022). NW2 is a hydrostatic, Boussinesq, and fully adiabatic configuration with an isopycnal vertical coordinate of 15 layers. The model domain is a 60°–wide sector, extending from 70°S to 70°N, with a southern reentrant channel representing the Southern Ocean. The model is forced by a meridionally-varying, zonally- and temporally-constant wind stress at the surface (Figure 1a). The model geometry includes idealized continental shelves on all sides of the domain (except in the channel) as well as a topographic ridge extending through the middle of the domain—a simplified mid-Atlantic ridge—and a semi-circular ridge centered in the channel's western opening—a simplified Scotia Arc (Figure 1b).

The NW2 configuration solves the stacked shallow-water equations, which describe equations of motion for the horizontal velocity $\mathbf{u}_n \equiv u_n\mathbf{i} + v_n\mathbf{j}$ and thickness h_n in layers $1 \leq n \leq N$ (here $N = 15$) of constant

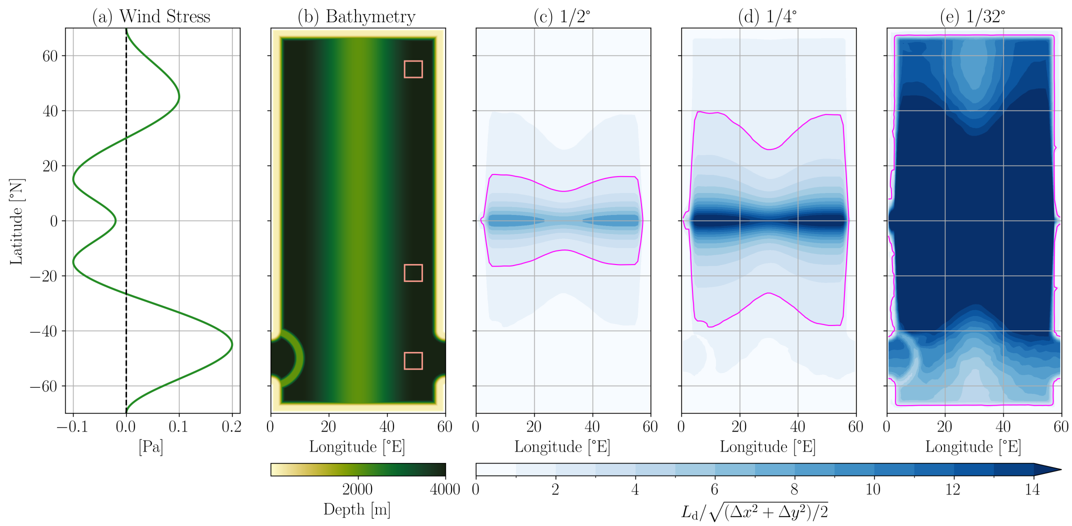

Figure 1: NeverWorld2 model configuration summary. (a) Zonal wind stress forcing. (b) Bathymetry. The boxes in (b) are regions where vertical structures are analyzed in Figure 8. (c–e) The ratio $L_\mathrm{d}/\sqrt{(\Delta x^2 + \Delta y^2)/2}$, where L_d is the first baroclinic Rossby deformation radius and $\Delta x, \Delta y$ are, respectively, the zonal and meridional grid spacings for (c) 1/2°, (d) 1/4°, and (e) 1/32° horizontal resolutions. The pink isoline in (c–e) indicates where $L_\mathrm{d}/\sqrt{(\Delta x^2 + \Delta y^2)/2} = 2$, which is an approximate cut-off criterion for whether mesoscale eddies are resolved (Hallberg, 2013).

density ρ_n (suppressing layer index n herein). In vector-invariant form, these equations are

$$\partial_t \mathbf{u} + (f + \zeta)\mathbf{k} \times \mathbf{u} + \nabla(K + M) = \mathbf{F}_v + \mathbf{F}_h, \tag{1}$$

$$\partial_t h + \nabla \cdot \big(h\mathbf{u}\big) = 0. \tag{2}$$

Here, $\nabla \equiv \nabla_\rho = \mathbf{i}\partial_x|_\rho + \mathbf{j}\partial_y|_\rho$ is the two-dimensional horizontal gradient operator at constant density; f is the Coriolis parameter; ζ is the relative vorticity; K is the kinetic energy per unit mass; M is the shallow-water Montgomery potential; $\mathbf{F}_v$ represents vertical stresses, including the surface wind stress, a background kinematic vertical viscosity, and a bottom stress following a quadratic drag law; and $\mathbf{F}_h$ represents horizontal stresses, including a biharmonic viscosity and, if present, a negative harmonic viscosity to represent backscatter (detailed in Section 2.2). Further details on the NW2 configuration, including specific parameter choices, can be found in Marques et al. (2022).

An evolution equation is also solved for tracer concentration c_n in each layer (again suppressing layer index n), which in its concentration-conserving, thickness-weighted form (Griffies et al., 2020; Loose et al., 2023) is

$$\partial_t(hc) + \nabla \cdot (h\mathbf{u}c) = 0. \tag{3}$$

In this study, we consider only passive tracers whose dynamics do not feed back on the flow. If an isopycnal diffusion parameterization is used then it is added to the right hand side of Equation (3) with diffusion coefficient κ_Redi (see Section 2.4); otherwise, implicit (numerical) diffusion that arises from discretizing the advection term serves to dissipate tracer variance at the grid scale.

2.2. Backscatter parameterization

The backscatter parameterization, designed to reenergize mesoscale turbulence at eddy-permitting resolution, is strictly only a closure in the momentum equation (Equation 1). The main thrust of this study is to evaluate whether, by energizing eddies, backscatter also enhances tracer mixing along isopycnals, thus potentially obviating the need for an additional eddy closure in the tracer equation (Equation 3).

The parameterization is identical to that detailed in Yankovsky et al. (2024) except for the choice of prescribed vertical structure (Equation 8). We thus describe only its salient features as well as the novel vertical structure parameterization used here; the reader is referred to Yankovsky et al. (2024) for further details. The horizontal stresses in Equation (1) comprise two terms; namely,

$$\mathbf{F}_h = -\nabla \cdot \left[\nu_4 \nabla (\nabla^2 \mathbf{u})\right] + \nabla \cdot (\nu_2 \nabla \mathbf{u}). \tag{4}$$

The dissipative biharmonic viscosity $\nu_4 > 0$ is set via a Smagorinsky scheme (Griffies & Hallberg, 2000; Marques et al., 2022). The harmonic viscosity ν_2, which is negative to represent backscatter, is set by

$$\nu_2(x,y,z,t) = -c_{\rm bs}\sqrt{2e(x,y,t)}L_{\rm mix}(x,y,t)\phi(x,y,z,t). \tag{5}$$

The nondimensional constant $c_{\rm bs} > 0$ is used to tune the parameterization (see Section 2.4). The vertically averaged subgrid mesoscale eddy kinetic energy (MEKE) $e = e(x,y,t)$ informs the local magnitude of backscatter and is set via a prognostic MEKE budget following a similar proposal of Jansen et al. (2019), namely

$$\partial_t e = \dot{e}_{\rm smag} - \dot{e}_{\rm bs} - \dot{e}_{\rm diss} - \dot{e}_{\rm adv}, \tag{6}$$

where $\dot{e}_{\rm smag}$ is the energy removed from the resolved flow by the biharmonic Smagorinsky viscosity, $\dot{e}_{\rm bs}$ is the energy returned to the resolved flow by the negative harmonic viscosity, $\dot{e}_{\rm diss}$ is the frictional dissipation of MEKE by quadratic drag, and $\dot{e}_{\rm adv}$ represents horizontal transport of MEKE parameterized as advection by the vertically averaged resolved flow and diffusion (see Jansen et al., 2019).

The subgrid eddy mixing length $L_{\rm mix} = L_{\rm mix}(x,y,t)$ in Equation (5) is defined as

$$L_{\rm mix} = \min(L_\Delta, L_{\beta^*}), \tag{7}$$

where L_Δ is the local horizontal grid spacing and $L^2_{\beta^*} = \sqrt{2e}/\beta^*$ is a subgrid Rhines scale that takes into account both planetary and topographic vorticity gradients, i.e., $\beta^* = |\beta\mathbf{j} - (f_0/H)\nabla H|$, where $\beta = \partial_y f$ and H is the local depth (Figure 1b); taking the minimum of several candidate mixing length scales is motivated by Jansen et al. (2015) (see also the discussion in Nummelin & Isachsen, 2024).

The subgrid eddy vertical structure $\phi = \phi(x,y,z,t)$ in Equation (5) is based on surface quasi-geostrophic dynamics following Zhang et al. (2024), with

$$\phi(x,y,z,t) = e^{c_{\rm exp} z_s / L_{\rm mix}}, \tag{8}$$

where $c_{\rm exp}$ is a nondimensional constant used to tune the surface-intensification of the vertical structure (see Section 2.4), $z_s(z) = -\int_z^0 N(z')/|f|dz'$ is a stretched vertical coordinate (N is the buoyancy frequency) and $L_{\rm mix}$ is from Equation (7). This formulation differs slightly to that presented in Zhang et al. (2024) in its definition of the "energy containing wavenumber," which here is taken to be the inverse of $L_{\rm mix}$ (multiplied by $c_{\rm exp}$). This vertical structure parameterization is the main difference to the simulations presented in Yankovsky et al. (2024), who used a vertical structure based on an equivalent barotropic mode. We choose to use the vertical structure parameterization of Zhang et al. (2024) as (i) it leads to slightly better overall results in our parameterized simulations, and (ii) it is the vertical structure being implemented for use in a backscatter parameterization in GFDL's ESM4.5.

2.3. Diagnosing isopycnal diffusivities

We evaluate the effect of this backscatter parameterization on tracers by diagnosing the three-dimensional structure of isopycnal diffusivities associated with eddy tracer fluxes and mean tracer gradients. Doing so in an isopycnal model leads naturally to the thickness-weighted average (TWA) formulation (e.g., Andrews, 1983; de Szoeke & Bennett, 1993; Young, 2012; Loose et al., 2023; Jansen et al., 2024). Diagnosing diffusivities from the resultant flux-gradient statistics is also a non-trivial task in numerical models. Here, we employ the Method of Multiple Tracers to diagnose robust estimates of isopycnal diffusivities in our simulations (Plumb & Mahlman, 1987; Bratseth, 1998; Bachman & Fox-Kemper, 2013; Fox-Kemper et al., 2013; Abernathey et al., 2013; Bachman et al., 2015; Wei & Wang, 2021; Zhang & Wolfe, 2022).

2.3.1. Defining the thickness-weighted average

Denoting $\overline{(\cdot)}$ as an appropriate Reynolds averaging operator (defined in Section 3.2) and averaging the thickness-weighted tracer equation (Equation (3)) naturally gives rise to the TWA, defined as

$$\hat{c} \equiv \frac{\overline{hc}}{\overline{h}}, \tag{9}$$

with eddy terms defined as deviations from this average

$$c'' \equiv c - \hat{c}. \tag{10}$$

The TWA tracer equation is then

$$\partial_t\left(\overline{h}\hat{c}\right) + \nabla \cdot \left(\overline{h}\hat{\mathbf{u}}\hat{c}\right) = -\nabla \cdot \left(\overline{h}\mathbf{F}^c\right), \tag{11}$$

where

$$\mathbf{F}^c \equiv \widehat{\mathbf{u}''c''} \tag{12}$$

is the eddy tracer flux in a thickness-weighted framework. The TWA is key to retaining the eddy tracer flux within the divergence. Mean and eddy tracer variance equations that follow from Equation (11) are presented in Appendix A.

2.3.2. Defining the mixing tensor

A common assumption when studying and parameterizing eddy fluxes is that the eddy tracer flux (Equation (12)) can be written as a mixing tensor K times the mean tracer gradient, i.e.,

$$\widehat{\mathbf{u}''c''} \equiv -\mathsf{K}\nabla\hat{c}, \quad \mathsf{K} \in \mathbb{R}^{2\times 2}. \tag{13}$$

If K is symmetric and positive-definite then the effect of Equation (13) in Equation (11) is that of down-gradient diffusion along isopycnals, which is the effect targeted by typical isopycnal diffusion parameterizations (Redi, 1982). In general, K is not symmetric and positive-definite; however, it can always be uniquely decomposed into symmetric and antisymmetric parts

$$\mathsf{K} = \mathsf{S} + \mathsf{A}, \tag{14}$$

where $\mathsf{S} = \left(\mathsf{K} + \mathsf{K}^{\mathrm{T}}\right)/2$ and $\mathsf{A} = \left(\mathsf{K} - \mathsf{K}^{\mathrm{T}}\right)/2$. This decomposition is physically meaningful as it can be shown (see Appendix A) that the flux associated with the antisymmetric part $\mathbf{F}^c_{\mathsf{A}} \equiv -\mathsf{A}\nabla\hat{c}$ has no effect on tracer variance (see also Griffies, 1998); this flux is often referred to as reversible "stirring." This is in contrast to the flux associated with the symmetric part $\mathbf{F}^c_{\mathsf{S}} \equiv -\mathsf{S}\nabla\hat{c}$ which acts as a global sink of mean tracer variance (see Appendix A), thus behaving like irreversible "mixing." Irreversible mixing is the effect targeted by typical isopycnal mixing parameterizations. Thus the primary focus in this study will be on the symmetric part S.

The symmetry of S implies it can be orthogonally diagonalized as

$$\mathsf{S} = \mathsf{U}\mathsf{D}\mathsf{U}^{\mathrm{T}}, \tag{15}$$

where the orthonormal columns of U are the eigenvectors of S and

$$\mathsf{D} = \begin{bmatrix} \kappa_1 & 0 \\ 0 & \kappa_2 \end{bmatrix}, \tag{16}$$

where κ_1 and κ_2 are the eigenvalues of S with $\kappa_1 \geq \kappa_2$ by definition. The eigenvalues κ_1 and κ_2 represent isopycnal diffusivities along orthogonal mixing directions defined by the columns of U. In this study, we "measure" the diffusivities and directions in our simulations by diagnosing K from Equation (13), the method for which we discuss next.

2.3.3. Diagnosing the mixing tensor

To diagnose the four entries of K by inverting Equation (13) requires two equations—two tracers advected by the same flow (e.g., Plumb & Mahlman, 1987). However, the use of only two tracers can cause the diagnosed K to depend strongly on the particular tracer distributions or to become ill-conditioned (Bratseth, 1998); for instance, if one of the tracer gradients vanishes then inverting Equation (13) becomes indeterminate. This motivates the Method of Multiple Tracers as a way to minimize these effects and to diagnose a robust, tracer-independent mixing tensor.

We consider the simultaneous advection of m passive tracers $c = c_j$ for $j = 1, \dots, m$, each with its own mean gradient $\nabla \hat{c}_j$. It is assumed that the same mixing tensor in Equation (13) applies to all tracers and thus depends only on the underlying flow, i.e., $\widehat{\mathbf{u}'' c_j''} = -\mathsf{K}\nabla \hat{c}_j$ for all j. If $\mathsf{F} \in \mathbb{R}^{2\times m}$ is a flux matrix with columns $\widehat{\mathbf{u}'' c_j''}$ and $\mathsf{G} \in \mathbb{R}^{2\times m}$ is a gradient matrix with columns $\nabla \hat{c}_j$, then the flux-gradient relationship for each tracer can be combined into a single matrix equation

$$\mathsf{F} = -\mathsf{K}\mathsf{G}. \tag{17}$$

For $m > 2$, Equation (17) is an overdetermined system of equations whose best-fit, least-squares solution is given by

$$\mathsf{K} \simeq \mathsf{K}_{\text{lsq}} = -\mathsf{F}\mathsf{G}^{\dagger} \tag{18}$$

where $(\cdot)^{\dagger}$ is the pseudoinverse. The symmetric part is computed similarly, i.e., $\mathsf{S} \simeq \mathsf{S}_{\text{lsq}} = (\mathsf{K}_{\text{lsq}} + \mathsf{K}_{\text{lsq}}^{\mathrm{T}})/2$.

In summary, by combining flux-gradient information from many tracers advected by the same flow, an optimal estimate for K (Equation (18)) can be diagnosed with low errors in the least-squares sense (see Appendix B) and the dependency of K on the particular tracer distributions is reduced (see Zhang & Wolfe, 2022).

The mean tracer gradients are maintained in statistically steady state through the addition of a slow restoring in the tracer equation (Equation (3)), so that

$$\partial_t(hc) + \nabla \cdot (h\mathbf{u}c) = \frac{1}{\tau} h\left(c^* - c\right), \tag{19}$$

where τ is a prescribed time scale and c^* is a prescribed target profile. This ensures that once the turbulent flow reaches statistically steady state, eddy fluxes will continuously feed off the mean gradients that each tracer has been reorganized into. The restoring time scales are slow with respect to typical eddy turnover times. Here we use two time scales and four target profiles; namely,

$$\tau \in \left\{2, 6\right\} \text{ years,}$$
$$c^* \in \left\{ \sin(2\pi x), \cos(2\pi x), \cos(\pi y), y\right\},$$

where x and y are normalized longitude and latitude coordinates; each tracer varies between -1 and 1. The combinations from these two sets results in $m = 8$ unique tracers, each with its own mean gradient, which makes Equation (17) overdetermined and available for pseudoinversion. Finally, to account for the effect that the weak restoring has on the flux-gradient relationship (Equation (13)), we here also incorporate the correction to Equation (18) described in Section 5.2 of Bachman et al. (2015).

2.4. Simulations

The simulations considered in this study are summarized in Table 1. A 1/32° reference simulation (ref) is "eddy-resolving" over most of the domain, except over the shelves along the edge of the domain (Figure 1e). All other simulations are "eddy-permitting" over most of the domain (Figure 1c, d), with horizontal grid spacings of 1/2° (p5) and 1/4° (p25). The eddy-permitting simulations use either no mesoscale parameterization (noBS), isopycnal tracer diffusion (noBS-Redi), or the backscatter parameterization outlined in Section 2.2 (BS). Except for the horizontal grid spacing, time step, and choice of mesoscale parameterization, all model parameters are the same across the simulations.

Simulation	Grid [°]	Backscatter	κ_{Redi} max, volume-mean [$m^2\ s^{-1}$]	c_{bs}	c_{exp}
p5noBS	1/2	No	0	—	—
p5BS	1/2	Yes	0	4	2.5
p5noBS-Redi	1/2	No	2400, 893	—	—
p25noBS	1/4	No	0	—	—
p25BS	1/4	Yes	0	2	1.75
p25noBS-Redi	1/4	No	2400, 516	—	—
ref	1/32	No	0	—	—

Table 1: Main simulations performed in this study. "Grid" refers to the horizontal grid spacing. "Backscatter" (BS) refers to whether the backscatter parameterization of Section 2.2 is used. If isopycnal tracer diffusion is used, its maximum value is given by "κ_{Redi} max"; this value is then scaled horizontally and vertically (see Section 2.4). If the backscatter parameterization is used, the tuning coefficients are given by c_{bs} (Equation (5)) and c_{exp} (Equation (8)).

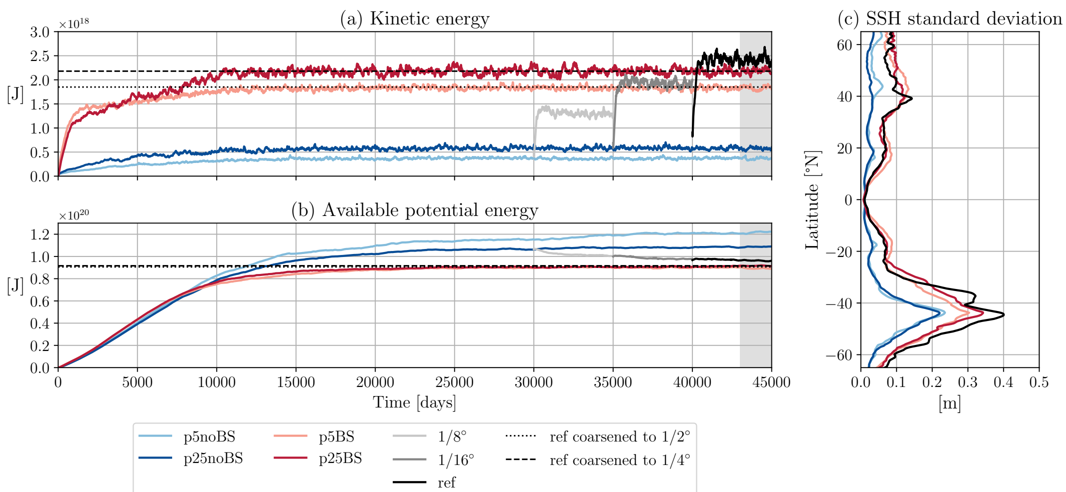

Figure 2: (a, b) Time series of globally integrated (a) kinetic energy and (b) available potential energy for the main simulations outlined in Table 1. The 1/8° and 1/16° simulations are not included in Table 1 as they are performed only as part of the spin-up of the 1/32° (ref) simulation (see text). The gray shading represents the 2,000–day window used for analysis throughout this study. (c) Zonally averaged sea surface height (SSH) standard deviation with respect to a 2,000–day climatology.

In the noBS-Redi simulations, the parameterized isopycnal tracer diffusivity has a maximum value of 2,400 $m^2\ s^{-1}$, a value based on the diagnosed diffusivities in the ref simulation (see Section 3.2). This maximum value is reduced horizontally by a step function resolution criterion (Hallberg, 2013)—set to zero where the mesoscale is deemed resolved (within the pink isoline in Figure 1) and unscaled otherwise—and vertically by a locally computed equivalent barotropic mode, a structure often used in observational and modeling studies (e.g., Adcroft et al., 2019; Groeskamp et al., 2020; Holmes et al., 2022). As tracers are passive in the NW2 configuration, isopycnal tracer diffusion does not affect the flow, and thus velocities and stratification are identical between the noBS and noBS-Redi simulations at each resolution. The noBS-Redi simulations will therefore only be considered in Sections 3.4 and 3.5 where passive tracer-only results are discussed.

Following Yankovsky et al. (2024), the backscatter simulations were tuned so that the globally integrated KE and APE simultaneously match those of the coarsened ref simulation (Figure 2a, b) via the parameterization's two main tuning parameters: c_{bs} (Equation (5)) and c_{exp} (Equation (8)); the values are given in Table 1. Other flow metrics were also checked when tuning, including the KE distribution throughout the domain as well as the stratification, especially in the reentrant channel (see Section 3.1). The values of c_{bs} differ to those in Yankovsky et al. (2024) as here we employ a different vertical structure for backscatter. However, they are consistent with these authors' analysis where the transition from 1/2° to 1/4° required a roughly halved c_{bs}

coefficient. In the regime where L_{mix} (Equation (7)) is set by the grid scale, then the vertical structure (Equation (8)) is more surface-intensified at 1/4° than at 1/2°, which is also consistent with the recommendations of Yankovsky et al. (2024). Finally, we employ the backscatter shut-off criterion described in Yankovsky et al. (2024): here, whenever the biharmonic viscosity ν_4 reaches 0.45 of its CFL limit, the viscous-source and backscatter-sink terms in the MEKE budget (Equation (6)) are turned off (until ν_4 settles back below the shut-off criterion). This mitigates a positive feedback cycle that can emerge between the biharmonic viscosity and harmonic negative viscosity (see Yankovsky et al., 2024); its use ensures numerical stability and obviates the need to substantially reduce the time step. Like the other tuning parameters, this value was chosen empirically when tuning.

The 1/2° and 1/4° simulations were spun up from rest for 45,000 days, which was sufficiently long for there to be minimal drift in globally integrated KE and APE (Figure 2a, b). More intensive diagnostics were saved over the final 2,000–day window, which will be the period used for analysis throughout the study. The spin-up procedure for the 1/32° simulation follows that described in Marques et al. (2022). First, a 1/8° simulation is branched from the 1/4° unparameterized simulation after 30,000 days by interpolating interface height and tracer fields, and setting velocities and transports to zero; the 1/8° simulation is run for 5,000 days with mechanical equilibrium quickly re-achieved. This procedure is then repeated at 1/16° and at 1/32°. The globally integrated KE and APE of the 1/32° simulation show minimal drift by the end of this procedure (Figure 2a, b).

3. Results

3.1. Evaluating the backscatter parameterization

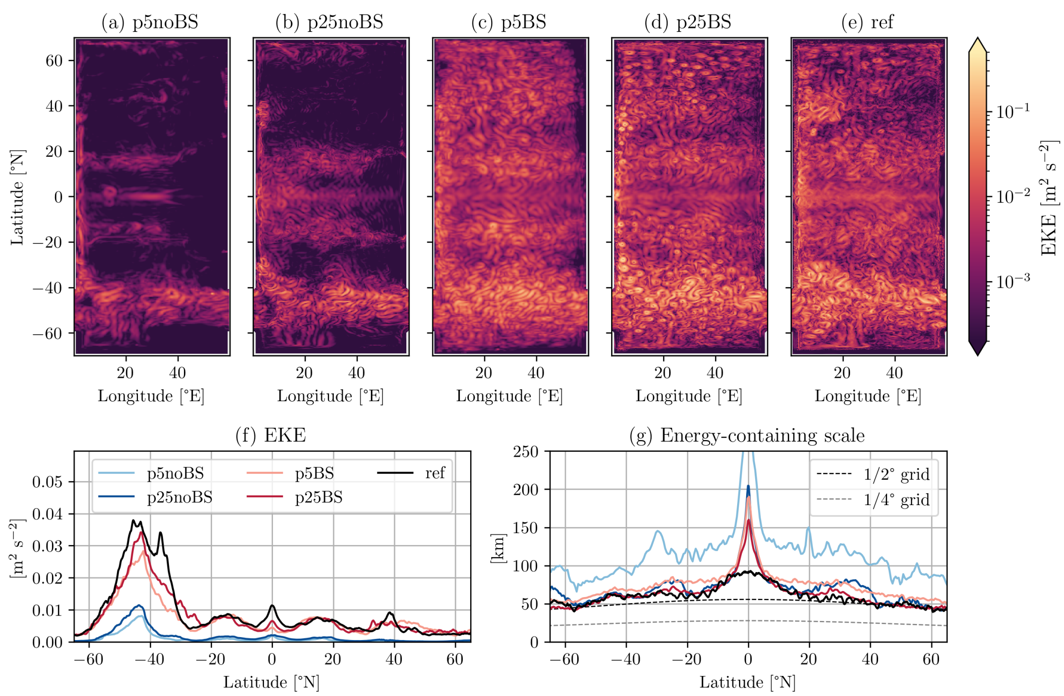

Figure 3: (a–e) Snapshots of depth-averaged EKE (on a log color scale) in the (a) p5noBS, (b) p25noBS, (c) p5BS, (d) p25BS, and (e) ref simulations (see Table 1). (f) Time-, depth-, and zonally averaged EKE in the same simulations. (g) Energy-containing scale (Equation (22)) in the same simulations; grid spacing is computed as $\sqrt{(\Delta x^2 + \Delta y^2)/2}$ following Hallberg (2013).

In this first analysis section, we briefly evaluate the effect of the backscatter parameterization on energetics and stratification, before focussing on tracer mixing in the following sections. We first examine the distribution of depth-averaged EKE. Denoting $(\cdot)'$ as a deviation from a 2,000–day time average $\overline{(\cdot)}^t$, then EKE is here defined as

$$\text{EKE} \equiv \frac{1}{2}\|\mathbf{u}'\|^2, \quad \mathbf{u}' \equiv \mathbf{u} - \overline{\mathbf{u}}^t, \tag{20}$$

and is computed from 10–day snapshots. Depth-averages are defined as

$$\overline{f}^z \equiv \frac{\sum_n h_n f_n}{\sum_n h_n} \tag{21}$$

for any field $f = f_n(x, y, t)$ (recall n is the layer index). Throughout much of the domain, depth-averaged EKE is an order of magnitude or larger in the backscatter simulations over unparameterized simulations (Figure 3); these results are similar to those in Yankovsky et al. (2024). Depth-averaged EKE in the channel ("Southern Ocean") is more commensurate across the simulation but is still between three to four times smaller in both p5noBS and p25noBS than in the p5BS, p25BS, and ref simulations (Figure 3f).

Although eddy activity is improved in the backscatter simulations, the lateral scale of eddies appears too large at 1/2° resolution (p5BS) (Figure 3c). To demonstrate this quantitively, we compute the energy-containing scale L_e from the sea surface height (SSH) deviation η'_SSH (e.g., Zhang & Wolfe, 2022; Yankovsky et al., 2024) via

$$L_\text{e} = \sqrt{\frac{\overline{\eta'^2_\text{SSH}}^t}{\overline{|\nabla \eta'_\text{SSH}|^2}^t}}. \tag{22}$$

When eddies are present, L_e is a good approximation to the peak of the surface kinetic energy spectrum (Zhang & Wolfe, 2022) and is thus indicative of the lateral eddy scale. However, in the limit of minimal eddy activity, L_e can become very large where spatial gradients become small, as occurs here for the p5noBS simulation. Figure 3g demonstrates that the eddy scale is larger in p5BS than in ref, especially in mid- and high northern latitudes. Overly large eddies also manifest as an overly large SSH standard deviation (Figure 2c). We hypothesize that the eddy scale is too large at 1/2° resolution since smaller eddies are too close to the grid scale (Figure 3g) and are dissipated by the biharmonic viscosity. This issue is mitigated at 1/4° resolution (p25BS), where the eddy scale is more in line with the ref simulation.

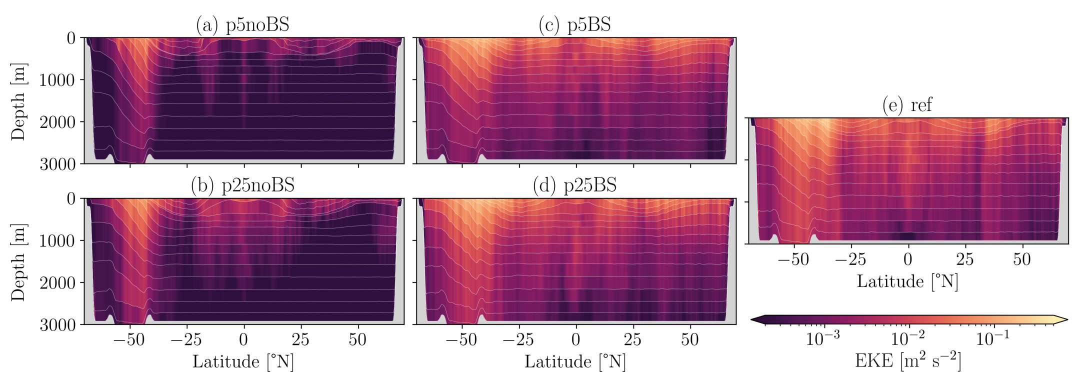

Figure 4: Snapshots of zonally averaged EKE (on a log color scale) in the (a) p5noBS, (b) p25noBS, (c) p5BS, (d) p25BS, and (e) ref simulations (see Table 1). Thin white lines show zonally averaged isopycnal interfaces; gray shading shows bathymetry.

We next consider the zonally averaged vertical structure of EKE. The EKE is too weak at depth in the unparameterized simulations (Figure 4a, b); the exception is in the Southern Ocean zonal jet where EKE, although still too weak, penetrates to depth more accurately, consistent with the findings of Yankovsky et al. (2022). In the p5BS simulation, EKE is too weak in the Southern Ocean at depths below roughly 1,500 m compared to the ref simulation (Figure 4c, e). However, throughout the rest of the domain, the vertical structure of EKE is largely in line across the p5BS, p25BS, and ref simulations. This suggests that backscatter is helping to liberate energy being trapped in higher baroclinic modes, which occurs when the baroclinic energy cycle is

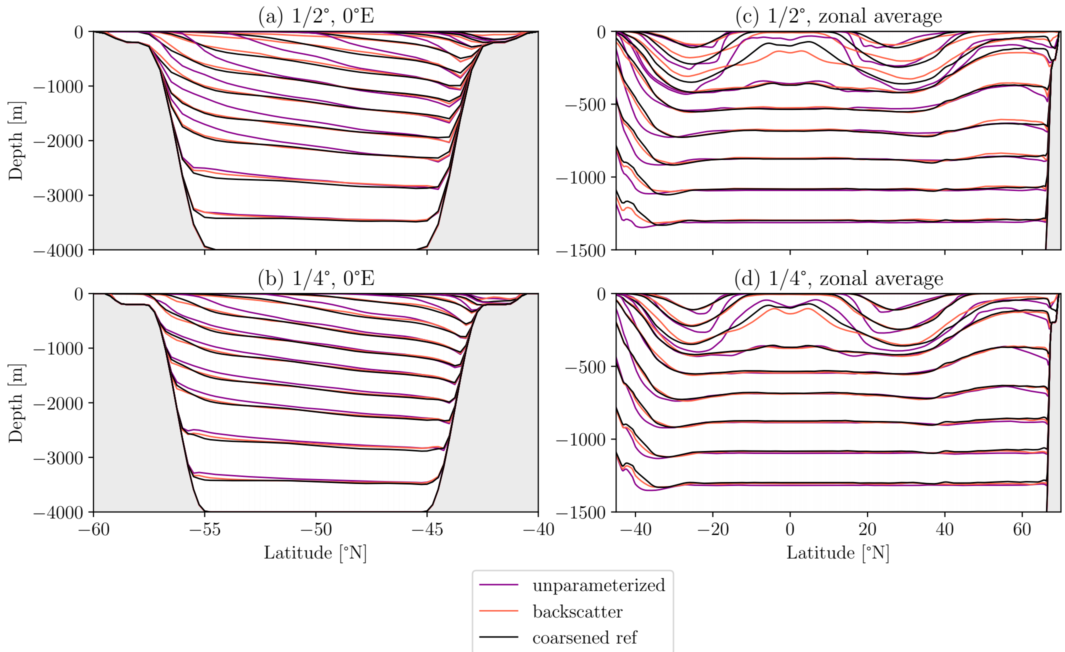

Figure 5: Time-averaged isopycnal interfaces in unparameterized (purple), backscatter (pink) and ref (black) simulations; gray shading shows bathymetry. (a–b) Meridional section over the reentrant channel at 0°E in (a) 1/2° simulations (p5noBS and p5BS) and (b) 1/4° simulations (p25noBS and p25BS). (c–d) Zonal average shown between 45°S and 70°N in (c) 1/2° simulations (p5noBS and p5BS) and (d) 1/4° simulations (p25noBS and p25BS). The ref simulation has been coarsened from 1/32° to either 1/2° (a, c) or 1/4° (b, d).

poorly resolved (Kjellsson & Zanna, 2017; Yankovsky et al., 2022), thereby allowing more barotropic eddies to form.

Finally, we evaluate the mean stratification in the simulations. Isopycnals are generally overly steep in the unparameterized simulations (Figure 5) due to the poorly resolved energy cycle of baroclinic eddies, which extract mean APE and convert it to EKE. A lack of mean APE extraction results in excessively steep isopycnals. Isopycnals in the backscatter simulations are closer to the ref simulation due to higher EKE and thus more efficient mean APE extraction (Figure 5). However, at 1/2° resolution (p5BS) the isopycnals are in some cases overly flat with respect to the ref simulation, largely in the upper ocean (Figure 5c). This is consistent with the eddies in this simulation being too large (Figure 3g), with larger baroclinic eddies being more efficient at extracting mean APE (Larichev & Held, 1995). The locations of the isopycnal outcrops in the Southern Ocean are inaccurate in the unparameterized simulations, whereas the outcrop locations in the backscatter simulations are closer to the ref simulation, which has consequences for Southern Ocean ventilation (see Section 3.5).

In summary, the backscatter parameterization leads to both elevated eddy activity, manifesting as larger EKE and larger SSH variability, as well as improved mean stratification over simulations without a backscatter parameterization, which have subdued eddy activity and overly steep isopycnals. Following the interpretation of Yankovsky et al. (2024), this joint effect of backscatter to both energize eddies and, thereby, lead to accurate large-scale stratification suggests that no additional GM-like thickness diffusion parameterization is necessary in these simulations. In the following sections, we seek to determine whether this backscatter parameterization also has a positive effect on along-isopycnal tracer mixing, suggesting that no additional Redi-like isopycnal diffusion parameterization is needed.

3.2. Diagnosed isopycnal diffusivities

In this section, we assess the results of the Method of Multiple Tracer (MMT) inversion outlined in Section 2.3.3, which diagnoses two isopycnal diffusivities and associated mixing directions. The averaging operator $\overline{(\cdot)}$ in the MMT inversion (Equations (9) and (10)) is a combination of online time averaging over a 2,000–day window and offline spatial coarsening onto a 2° × 2° grid. The diffusivities and mixing directions are thus defined on this 2° × 2° grid. Eddy products are computed by assuming the averaging operator obeys standard Reynolds assumptions, i.e., $\widehat{\mathbf{u}''c''} = \widehat{\mathbf{u}c} - \hat{\mathbf{u}}\hat{c}$ (see Section 2.3.1). Note that the simulations with isopycnal tracer diffusion (p5noBS-Redi and p25noBS-Redi) are not discussed here.

3.2.1. Spatial distribution of diffusivities

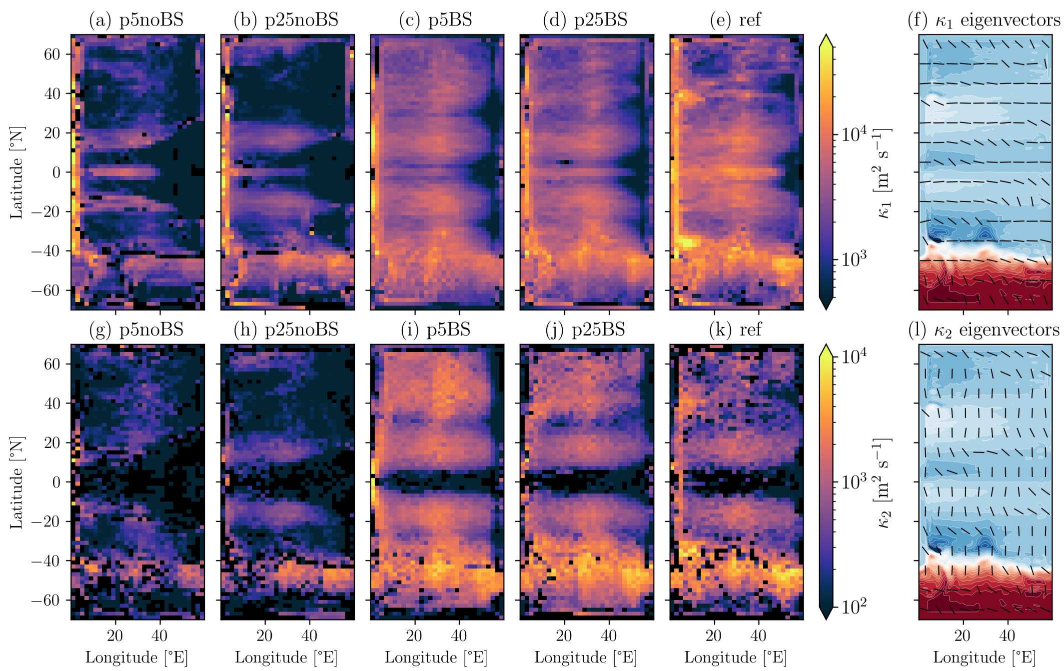

Figure 6: Depth-averaged isopycnal diffusivities and eigenvectors (mixing directions) from the Method of Multiple Tracers inversion (see Section 2.3.3). (a–e) κ_1 (on a log color scale) in the (a) p5noBS, (b) p25noBS, (c) p5BS, (d) p25BS, and (e) ref simulations. (f) Eigenvectors associated with κ_1 in the ref simulation (the other simulations are similar), and the time-mean barotropic stream function is shown in contours. (g–l) As in (a–f) but for κ_2. Negative values of κ_1 and κ_2 are plotted in black. Note that the colorbar limits differ for κ_1 and κ_2. The eigenvectors in (f, l) are shown on a coarser grid than the diffusivities for ease of viewing.

Figure 6 shows the depth-averaged isopycnal diffusivities κ_1 and κ_2 (Equation (15)) as well as their mixing directions (eigenvectors). The larger diffusivity κ_1 generally has its mixing direction aligned with the mean flow, while κ_2 is generally directed across it (Figure 6f, l). That κ_1 tends to represent an along-mean flow diffusivity suggests that its larger values may be the result of mean flow-induced shear dispersion (Taylor, 1953; Smith, 2005). Similarly, that κ_2 represents an across-mean flow diffusivity suggests that it may be affected by mean flow suppression (Ferrari & Nikurashin, 2010; Groeskamp et al., 2020). These hypotheses are tested in Section 3.2.2.

Similar to EKE (see Section 3.1), depth-averaged isopycnal diffusivities are subdued in the p5noBS and p25noBS simulations over much of the domain compared to the p5BS, p25BS, and ref simulations, and are smaller in many regions by an order of magnitude or more (Figure 6). In the backscatter and ref simulations, depth-averaged diffusivities are generally $\mathcal{O}$(100–1,000) m^2 s^{-1} and tend to be larger on or downstream of the meridional ridge. Diffusivities are elevated in the energetic western boundary current regions at ±40°N in the ref simulation as well as in a mixing hotspot in the channel downstream of the ridge at roughly 50°E; this is less pronounced in the backscatter simulations, which showed weaker EKE in these regions (Figure 3). In contrast, diffusivities are larger in the p5BS simulation than in the ref simulation at northern mid- and high latitudes. This may stem from the overly large eddies in this region (Figure 3g): from a mixing length argument, eddies with larger lateral scales but commensurate energy levels will generate larger diffusivities.

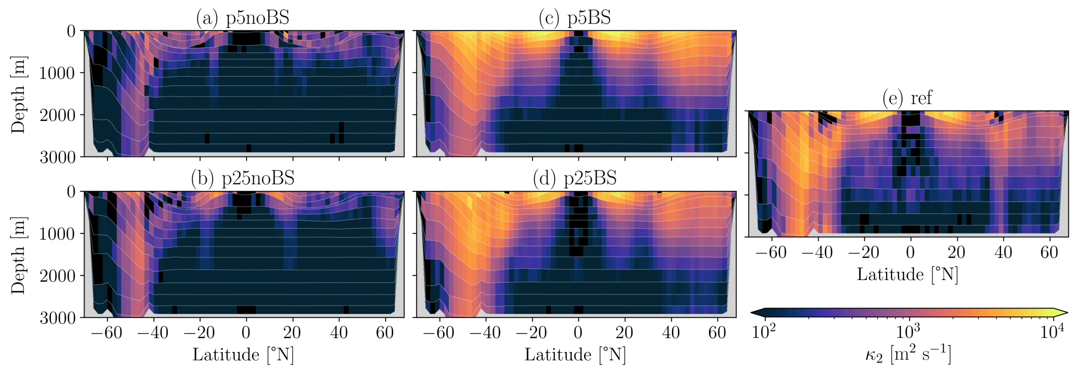

Figure 7: Zonally averaged isopycnal diffusivity κ_2 (on a log color scale) in the (a) p5noBS, (b) p25noBS, (c) p5BS, (d) p25BS, and (e) ref simulations. Thin white lines show zonally and time-averaged isopycnal interfaces (coarsened to the same horizontal grid as the diffusivities); gray shading shows bathymetry. Negative values are plotted in black.

We next examine the zonally averaged vertical structure of the diffusivities, focussing on the mostly meridionally directed κ_2 diffusivity (Figure 7). In the unparameterized simulations, the vertical damping of mixing largely follows the vertical damping of EKE (cf. Figures 4 and 7). In the backscatter simulations, the vertical structure of mixing is remarkably similar to the ref simulation in the subtropics. However, in the ref simulation there are subsurface maxima in the Southern Ocean zonal jet and in the western boundary current region (roughly 40°N), whereas the diffusivity appears more surface-intensified in the backscatter simulations, particularly in p5BS.

Figure 8 shows the vertical structures of κ_1 and κ_2 averaged over three regions highlighted in Figure 1b: in the southeastern subtropics, in the northeastern subpolar region, and in the Southern Ocean. In all regions, the magnitude of κ_1 is generally too low in p5BS and p25BS compared to ref, especially in the Southern Ocean region (Figure 8a, b, c). Agreement in magnitude is generally stronger in κ_2, with excellent similarity in the subtropical region in both magnitude and e-folding depth (Figure 8d). However, as noted in the previous paragraph, there are differences in the vertical structures of κ_2, particularly between the p5BS and ref simulations in the subpolar and Southern Ocean regions shown in Figure 8. We next test possible hypotheses to explain (i) the enhancement of κ_1 and (ii) the surface suppression of κ_2 in the ref simulation; our main goal is to explain the differences between the backscatter and ref simulations.

3.2.2. Shear dispersion enhancement and mean flow suppression

Mixing length theory proposes that an eddy diffusivity $\mathcal{K}$ be written as

$$\mathcal{K} \equiv \Gamma u_{\mathrm{rms}} \ell, \tag{23}$$

where Γ is the mixing efficiency, u_{rms} is the root-mean-square (rms) eddy velocity, and ℓ is an eddy mixing length. Here, we assume that $\Gamma = 0.35$ (e.g., Klocker & Abernathey, 2014; Groeskamp et al., 2020), that the eddy velocity is given by the time-averaged and vertically-dependent EKE (Equation (20)), i.e.,

$$u_{\mathrm{rms}}(x, y, z) = \sqrt{2\,\overline{\mathrm{EKE}}^{t}}, \tag{24}$$

that the eddy mixing length is given by the vertically-independent energy-containing scale (Equation (22)), i.e., $\ell = L_{\mathrm{e}}$, and that $\mathcal{K}$ represents a background eddy diffusivity.

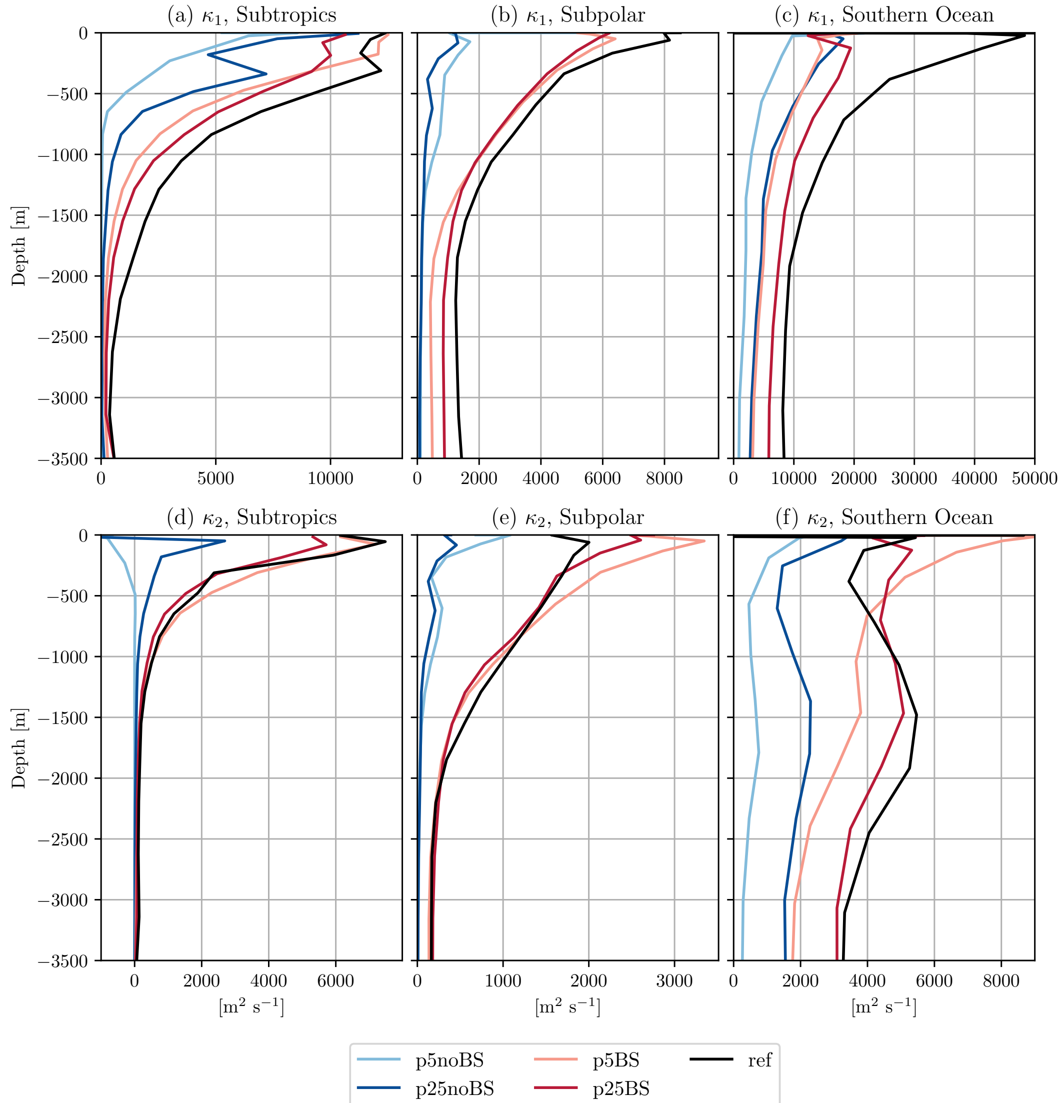

Figure 8: Vertical structure of (a–c) κ_1 and (d–f) κ_2. Regions shown (see boxes in Figure 1b) are (a, d) subtropics, averaged over (46°E to 52°E, −22°N to −16°N); (b, e) subpolar, averaged over (46°E to 52°E, 52°N to 58°N); and (c, f) Southern Ocean averaged over (46°E to 52°E, −54°N to −48°N). Averages over the regions are thickness-weighted averages (Equation (9)) using the time-mean thickness $\overline{h}$ (which is necessary where layer thicknesses vary over the spatial region); negative diffusivities are included in the average.

We first assess why κ_1 tends to be larger in the ref simulation than in the backscatter simulations. Shear dispersion (Taylor, 1953) suggests that a diffusivity in the along-mean flow direction $\mathcal{K}_{\parallel}$ should be enhanced over a background diffusivity, with the prediction (up to a scaling constant)

$$\mathcal{K}_{\parallel} \equiv \frac{\mathcal{U}^2 \ell_{\mathcal{U}}^2}{\mathcal{K}}, \tag{25}$$

where $\mathcal{U}$ is a scale for the mean flow magnitude and $\ell_{\mathcal{U}}$ is a length scale for the mean flow shear. Smith (2005) showed this prediction to hold reasonably accurately in jet-dominated two-dimensional turbulence. We therefore compute Equation (25) with depth-averaged fields by defining a mean flow scale and a shear length scale as

$$\mathcal{U}^2 \equiv \left\langle \left(\overline{u}^{z,t}\right)^2 + \left(\overline{v}^{z,t}\right)^2 \right\rangle, \quad \ell_{\mathcal{U}}^2 \equiv \frac{\mathcal{U}^2}{\left\langle \left(\partial_y \overline{u}^{z,t}\right)^2 + \left(\partial_x \overline{v}^{z,t}\right)^2 \right\rangle}, \tag{26}$$

where $\overline{(\cdot)}^{z,t}$ is a depth- and time-average and $\langle\cdot\rangle$ is a spatial coarsening onto a 2° × 2° grid. We also use the depth-averaged mixing length diffusivity $\langle\overline{\mathcal{K}}^{z}\rangle$ in Equation (25). Figure 9 shows the result plotted against $\overline{\kappa_1}^{z}$ averaged over the three regions in Figure 8. The prediction is imperfect, especially in the subtropics region, which is possibly related to the neglect of vertical variations in the flow. However, the results suggest, at least in the subpolar and Southern Ocean regions, that enhanced dispersion along strong barotropic shear flows may contribute to the increases in κ_1 across the resolutions.

We next assess whether mean flow suppression theory can explain the differences in the vertical structure of κ_2, in particular, between p5BS and ref, which showed larger discrepancies (Figure 8e, f). Such theory (Ferrari & Nikurashin, 2010; Klocker et al., 2012) proposes that the diffusivity in the across-mean flow direction $\mathcal{K}_\perp$ be suppressed over a background diffusivity in the presence of mean flows. We write the result of Ferrari and Nikurashin (2010) in the general form

$$\mathcal{K}_\perp \equiv S_\perp \mathcal{K}, \tag{27}$$

where

$$S_\perp \equiv \frac{1}{1 + \gamma^{-2} k_e^2 \left(c_{w,\parallel} - U_\parallel\right)^2} \tag{28}$$

is the suppression factor in the cross-stream direction. Here, γ is an eddy decorrelation rate, which we assume to be depth-independent and is found by a least squares approach similar to previous studies (e.g., Klocker et al., 2012; Groeskamp et al., 2020; Zhang & Wolfe, 2022); k_e is an eddy wavenumber, here computed as $k_\mathrm{e} = 1/\ell_\mathrm{e}$, where ℓ_e is the energy-containing scale (Equation (22)); and $c_{w,\parallel}$ and $U_\parallel$ are, respectively, the eddy phase speed and time-averaged flow projected onto the eigenvector associated with κ_1 (recall that this is orthogonal to the direction associated with κ_2). The eddy phase velocity is calculated using the long planetary Rossby wave dispersion relation, Doppler-shifted by the depth- and time-averaged flow as suggested by Klocker and Marshall (2014), so that

$$\mathbf{c}_w = \overline{\mathbf{u}}^{z,t} - \beta L_\mathrm{d}^2 \mathbf{i}. \tag{29}$$

We then project the time-averaged flow $\overline{\mathbf{u}}^{t}$ and $\mathbf{c}_w$ onto the eigenvector associated with κ_1 to calculate $U_\parallel$ and $c_{w,\parallel}$, respectively. From this construction, the only depth-varying component of Equation (28) comes from $U_\parallel$. As noted above, γ is found via a least squares approach by minimizing the vertical integral of the squared difference between profiles of κ_2 and $\mathcal{K}_\perp$. This is done for each profile in each region shown in Figure 8 (results were similar if γ was instead found by fitting the averaged profile in each region). We show only the results for the subpolar and Southern Ocean regions in Figure 9 as Equation (27) was not a good model for κ_2 in the subtropics region (not shown).

The suppressed diffusivity $\mathcal{K}_\perp$ generally captures the vertical structure of κ_2 in both the subpolar and Southern Ocean regions in the upper 1,000 m (Figure 9), though performs less well at depths below this (see Zhang & Wolfe, 2022). In the subpolar region, the mixing length diffusivity $\mathcal{K}$ is similar to both $\mathcal{K}_\perp$ and κ_2. This demonstrates that, in this region, the differences in κ_2 between the backscatter and ref simulations arise largely from differences in the eddy scale and EKE. In contrast, in the Southern Ocean region, $\mathcal{K}_\perp$ is systematically smaller than κ_2 at the surface, and is increasingly so as resolution increases. In this region, the mean flow $U_\parallel$ at the surface is in fact slightly stronger in p5BS than in ref (not shown), so differences between these simulations arise from the $\gamma^{-2}k_\mathrm{e}^2$ prefactor (Equation (28)). The eddy decorrelation time scale from the fitting procedure is found to be $\gamma^{-1} = 3.6, 4.7$, and 5.5 days, and the energy-containing scale is $k_\mathrm{e}^{-1} = 60, 55$, and 58 km in the p5BS, p25BS, and ref simulations, respectively. The $\gamma^{-2}k_\mathrm{e}^2$ prefactor is thus indeed smaller in p5BS than in ref. Ferrari and Nikurashin (2010) suggest that γ^{-1} is proportional to the eddy strain rate $\left(k_\mathrm{e}^2 \mathrm{EKE}\right)^{-1/2}$. However, computing γ^{-1} as such using the energy-containing scale (Equation (22)) and EKE here implies the opposite tendency, i.e., γ^{-1} decreases as resolution increases (not shown), largely since the

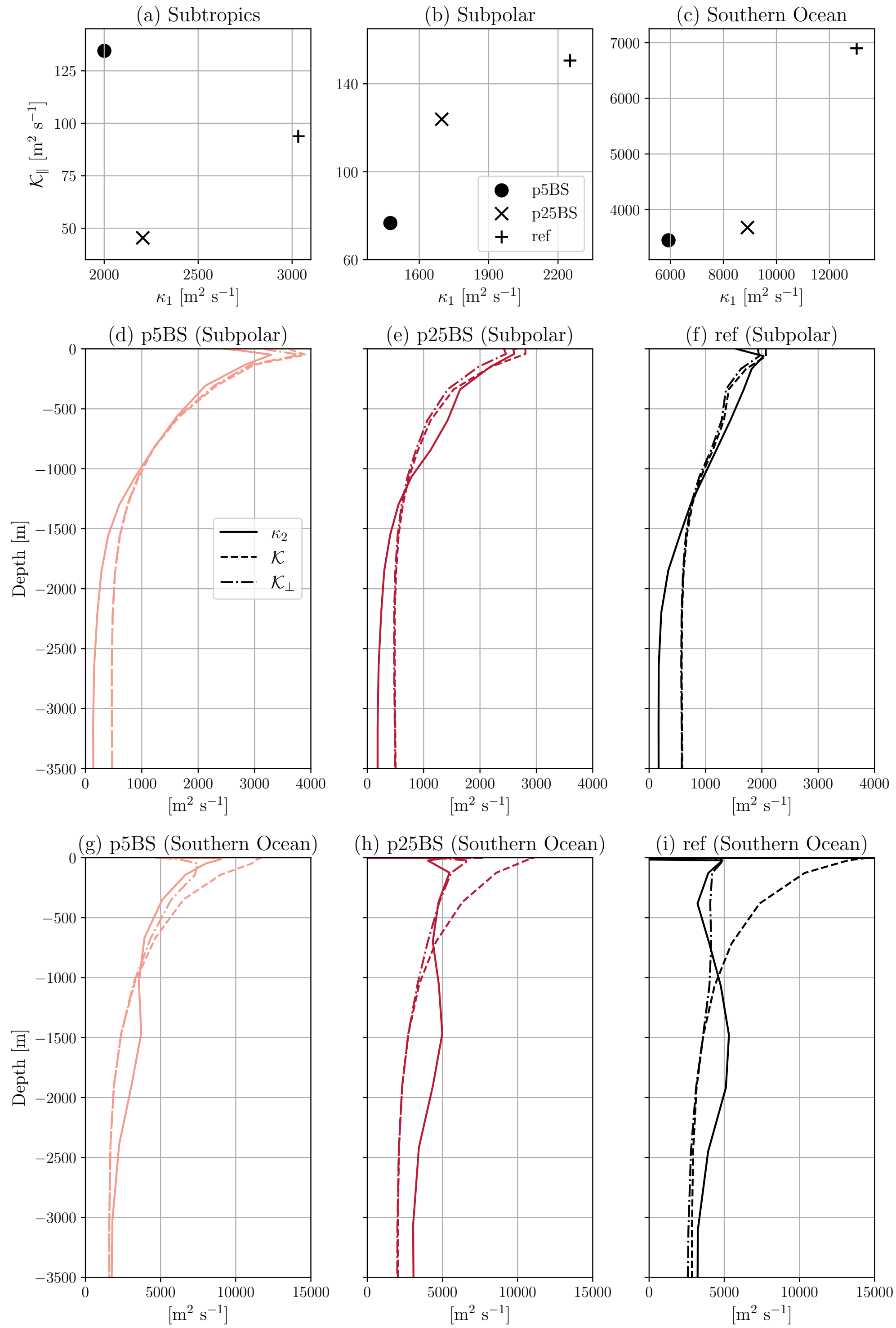

Figure 9: (a–c) Depth-averaged shear dispersion diffusivity (Equation (25)) against depth-averaged κ_1, averaged over the same three regions as in Figure 8. (d–f) Vertical structure of κ_2 (solid), mixing length diffusivity $\mathcal{K}$ (Equation (23); dashed) and suppressed mixing length diffusivity $\mathcal{K}_{\perp}$ (Equation (27); dashdot) in the subpolar region in the (d) p5BS, (e) p25BS, and (f) ref simulations (cf. Figure 8b, e). (g–i) As in (d–f) except in the Southern Ocean region (cf. Figure 8c, f).

eddies become more energetic as resolution increases (Figure 6f). This discrepancy between the time scale estimated from fitting and the time scale estimated from the eddy strain rate may come from the assumption that mixing is dominated by the energy-containing scale, as the true mixing length may be different (Thompson & Young, 2006; Klocker et al., 2012). Mixing is also likely driven by an increasingly multichromatic eddy field as resolution (and thus the number of scales that contribute to mixing) increases, which may modify estimates based on a single scale (Chen et al., 2014). A detailed examination of these effects and the dependencies on elements of the parameterization is left for future work, as it is beyond the scope of the present study. However, we take it to be an interesting empirical result that the mixing suppression function from Ferrari and Nikurashin (2010) is able to explain the smaller degree of surface suppression in p5BS relative to ref, possibly due to larger eddies that decorrelate more quickly.

3.2.3. Statistical distribution of diffusivities

An additional question to address is how backscatter modifies the statistical distribution of the isopycnal diffusivities throughout the domain. Backscatter leads to improvements over unparameterized simulations, shifting the distributions of κ_1 and κ_2 towards larger values and more closely matching the ref simulation (Figure 10). Neither the p5BS nor p25BS simulation matches the extremes in the tail of the κ_1 distribution in the ref simulation, which is possibly related to horizontal shear flows that are weaker or unresolved at coarser resolutions as suggested by the analysis in the previous section (Figure 9). The κ_2 distributions show much closer agreement between the p5BS, p25BS, and ref simulations (Figure 10b), which is reflected in their near-equal globally averaged values (Figure 10d). Although κ_1 is smaller in the backscatter simulations, typical isopycnal diffusion parameterizations act isotropically within the isopycnal plane. These near-equal global values of κ_2 thus suggest that no supplemental isopycnal diffusion is desirable in the backscatter simulations, at least in the global average.

3.3. Sensitivity to backscatter strength

In this section, we determine the sensitivity of isopycnal mixing to the strength of the parameterized backscatter. Here, we deviate from the main simulations summarized in Table 1 and assess a set of simulations that vary the magnitude of c_{bs} (Equation (5)), which modulates the amplitude of the negative viscosity. We show only simulations at 1/4° resolution; results were similar at 1/2° resolution (not shown). The particular emphasis is on how the isopycnal diffusivities vary as a function of eddy energy and length scales as c_{bs} is varied.

The results of the 1/4° simulations are summarized in Figure 11. Globally integrated KE increases as c_{bs} increases (Figure 11a), although the changes in KE become smaller for larger values of c_{bs}. Globally integrated APE decreases as c_{bs} increases (Figure 11a) since a more active eddy field extracts APE more effectively from the mean flow, thereby flattening isopycnals (Figure 5). The magnitudes of the isopycnal diffusivities generally increase as c_{bs} increases (Figure 11d), and these increases follow a similar pattern to increases in the EKE (Figure 11c). Notably, the energy-containing scale (Equation (22)) does not vary in a systematic fashion as c_{bs} varies (not shown), which is implied by the isopycnal diffusivities increasing at roughly the same rate as eddy velocities. If the energy-containing scale of the eddies increased as c_{bs} increased, then diffusivities would likely increase at a faster rate than eddy velocities from mixing length arguments (see Equation (23)). That the energy-containing scale does not change dramatically suggests it is more constrained by large-scale processes such as bottom drag and stratification, which are not modified as strongly by changes in c_{bs} compared to the strong changes in EKE. We note that we have not investigated the effects of changes in the vertical structure via c_{exp} (Equation (8)), which influences the resultant stratification (Yankovsky et al., 2024). Nevertheless, our results indicate that, at least with the present backscatter scheme, the strength of isopycnal mixing is strongly controlled by the strength of eddy energy as modulated by the magnitude of the backscatter.

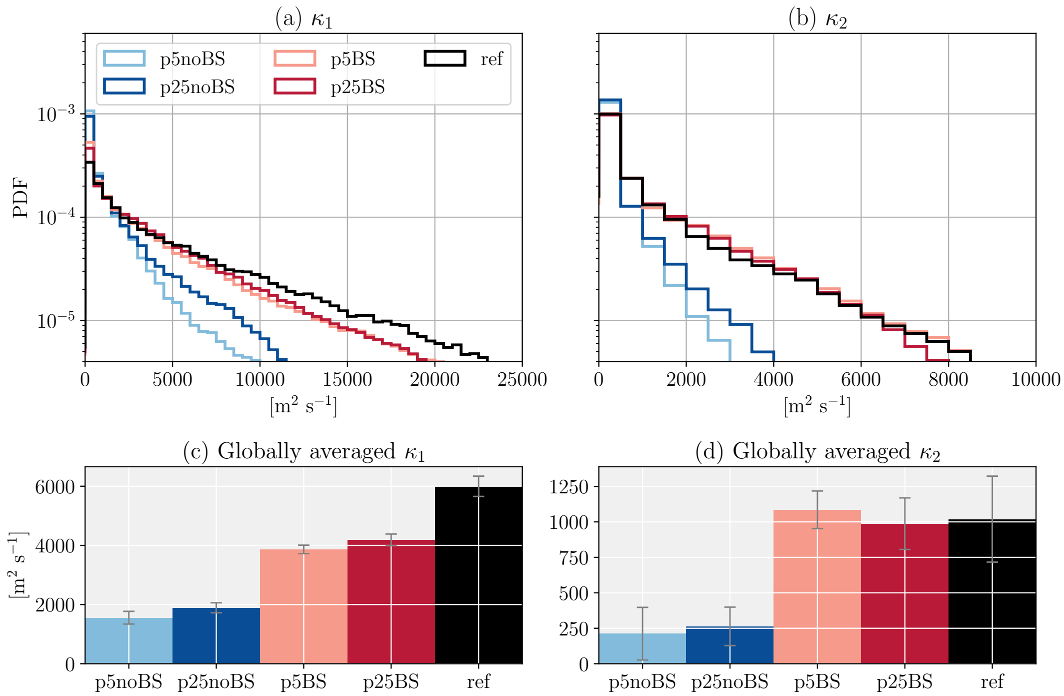

Figure 10: (a–b) Histograms (plotted as probability densities) of (a) κ_1 and (b) κ_2 for the p5noBS, p25noBS, p5BS, p25BS, and ref simulations; histograms are computed by linearly interpolating the diffusivities onto a uniform vertical grid with 25 m spacing and then binning into 500 $\mathrm{m}^2\ \mathrm{s}^{-1}$ bins, with only positive values shown. (c–d) Globally averaged values of (c) κ_1 and (d) κ_2 for the same simulations; averages are taken over positive values only. Error bars in (c, d) denote $\pm\sigma$, where σ is the estimated standard deviation from the least squares inversion (see Appendix B.)

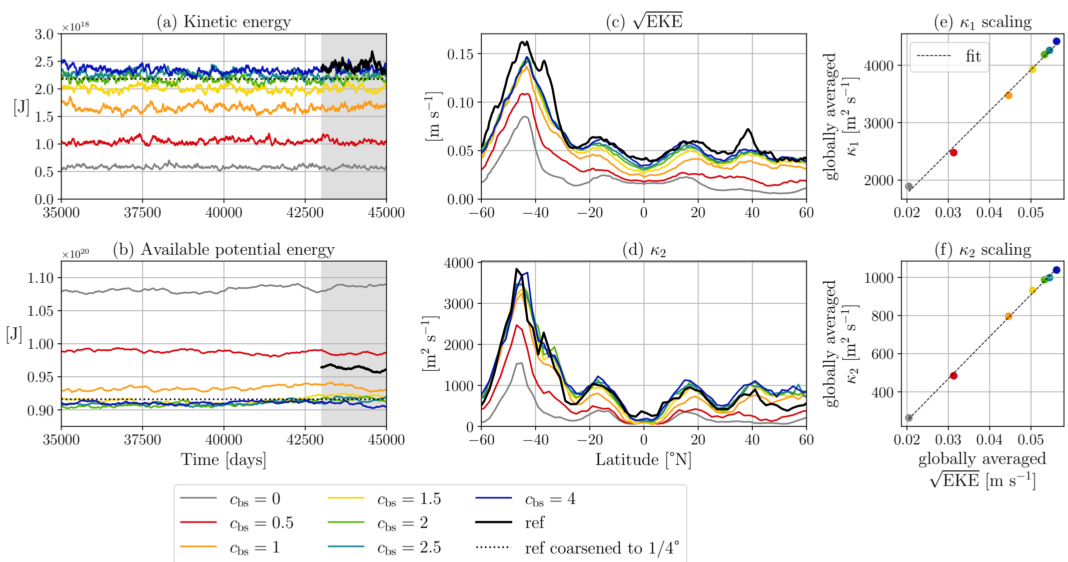

Figure 11: Summary of simulations varying c_{bs}. (a, b) Time series of globally integrated (a) kinetic energy and (b) available potential energy; the gray shading is the 2,000–day window used for analysis through this study. (c, d) Zonally and depth-averaged (c) time-averaged eddy velocity scale $\sqrt{\mathrm{EKE}}$ and (d) κ_2. (e, f) Globally averaged (e) κ_1 and (f) κ_2 against the globally and time-averaged eddy velocity scale.

3.4. Tracer biases

In this section, we return to the main simulations (Table 1) and examine how improved isopycnal mixing from backscatter impacts tracer biases relative to the ref simulation. We here also seek to compare the effect of backscatter-driven isopycnal mixing to the effect of parameterized isopycnal diffusion. The isopycnal diffusion simulations (Redi) are described in Section 2.4 and summarized in Table 1.

Figure 12 shows depth-averaged snapshots of one of the tracers used in the MMT inversion. The unparameterized simulations (Figure 12a, d) show stronger gradients in the tracer where restoring gradients are largest (at 15°E and 45°E in Figure 12) compared to the ref simulation. This is a consequence of the subdued eddy activity which, if present, would act to mix away these gradients. Adding isopycnal diffusion improves mean biases by diffusing overly large gradients (Figure 12b, e, h) [note that the impact of the abrupt resolution function is seen in Figure 12, but a smooth transition is not necessarily more suitable (Hallberg, 2013)]. However, with isopycnal diffusion these mean bias reductions are at the expense of variance biases, as diffusion also washes away the tracer signature of the partially resolved eddy variability (Figure 12h). The backscatter simulations, by enhancing the eddy activity that stirs tracers, show reductions in both mean and variance biases with respect to the ref simulation (Figure 12c, f, h). That backscatter improves both mean and variance biases suggests that it is a preferable parameterization for tracer mixing in an eddy-permitting regime. The mean bias reductions from isopycnal diffusion might be improved through tuning of the tracer diffusion coefficient, a different choice of resolution function or a different prescribed vertical structure. However, the worsening of variance biases is likely a general result whenever some eddy variability is resolved and isopycnal diffusion applied to total resolved fields is added. It is possible that a splitting procedure, such as that proposed by Mak et al. (2023) for the GM parameterization, could be applied to a Redi parameterization and lead to better results in this sense. However, how to implement such a procedure (see Mak et al., 2023) and comparisons to the approach we take here is beyond the scope of our study and is left for future work.

3.5. Ventilation tracer

In this final analysis section, we assess the impact of the backscatter parameterization on ocean ventilation. Eddy-driven isopycnal mixing plays an important role in ventilating the interior ocean, especially in the Southern Ocean where isopycnals outcrop at the surface, providing an adiabatic pathway from the ocean surface into the interior (Morrison et al., 2022). We have shown there to be differences in how our simulations represent both outcrop locations and the strength of isopycnal mixing in the Southern Ocean region of the model (Sections 3.1 and 3.2). To investigate the effect of these differences, we performed an idealized ventilation tracer experiment with a similar configuration to previous studies (e.g., England, 1995; Abernathey & Ferreira, 2015; Balwada et al., 2018).

The ventilation tracer is initialized first everywhere to 0. At every time step, it is then set to a value of 1 if the center of an isopycnal layer in a grid cell lies above a prescribed constant depth of 100 m. Otherwise, it is passively stirred into the interior. This experiment was performed over the 2,000–day window once the flow in each simulation had already reached statistically steady state (Figure 2), and output is saved as 5–day averages.

The results of this experiment are summarized in Figure 13. It is readily seen that in all simulations the ventilation tracer is taken up at the surface and mixed into the interior by eddy stirring alone (there is no diapycnal mixing in the model), which is indicated by values of tracer spanning the range between 0 and 1. The uppermost layers, which are mostly shallower than the 100 m depth value, are almost saturated with tracer after 2,000 days, while eddy stirring ventilates deeper layers more slowly. The highlighted isopycnal layer (Figure 13a–g) is the first layer to outcrop only in the Southern Ocean (i.e., it does not also outcrop in the northern part of the domain) and examining the tracer on this layer provides a clear picture of Southern Ocean ventilation in these simulations (Figure 13h, i).

Tracer concentration grows more slowly in the p5noBS and p25noBS simulations, which is a result of the subdued eddy activity that stirs the tracer into the interior (Figure 13h). This is mostly a result of subdued eddy stirring rather than incorrect outcropping, as confirmed by the simulations with added isopycnal tracer diffusion, which have the identical underlying flow and stratification to the corresponding unparameterized

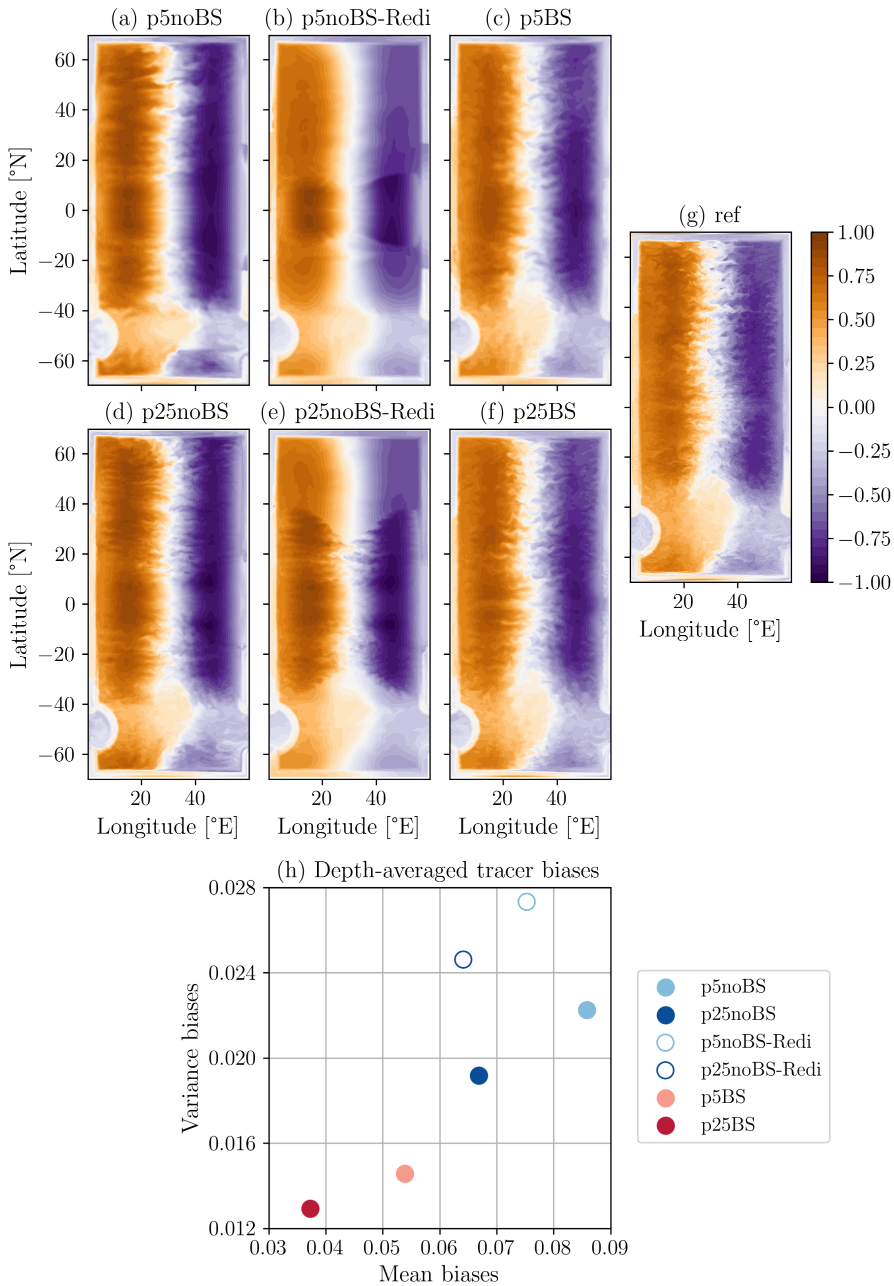

Figure 12: (a–g) Snapshots of depth-averaged tracer restored to target profile $c^* = \cos(2\pi x)$ with restoring time scale $\tau = 6$ years (see Section 2.3.3) in the (a) p5noBS, (b) p5noBS-Redi, (c), p5BS, (d) p25noBS, (e), p25noBS-Redi, (f) p25BS, and (g) ref simulations. (h) Depth-averaged biases averaged over all tracers in the MMT inversion (see Section 2.3.3). For each tracer for each simulation: mean biases are computed by depth-averaging, then time-averaging, and then taking the root-mean-square of the difference between the given simulation and the ref simulation coarsened to either 1/2° or 1/4°; variance biases are computed by depth-averaging, then taking the temporal standard deviation, and then taking the root-mean-square of the difference between the given simulation and the ref simulation coarsened to either 1/2° or 1/4°. An average is then taken over all tracers in each simulation to obtain the values in (h).

simulation: p5noBS-Redi and p25noBS-Redi show growth in tracer concentration on this layer more in line with the ref simulation. However, this victory is pyrrhic as these simulations exhibit too high tracer con-

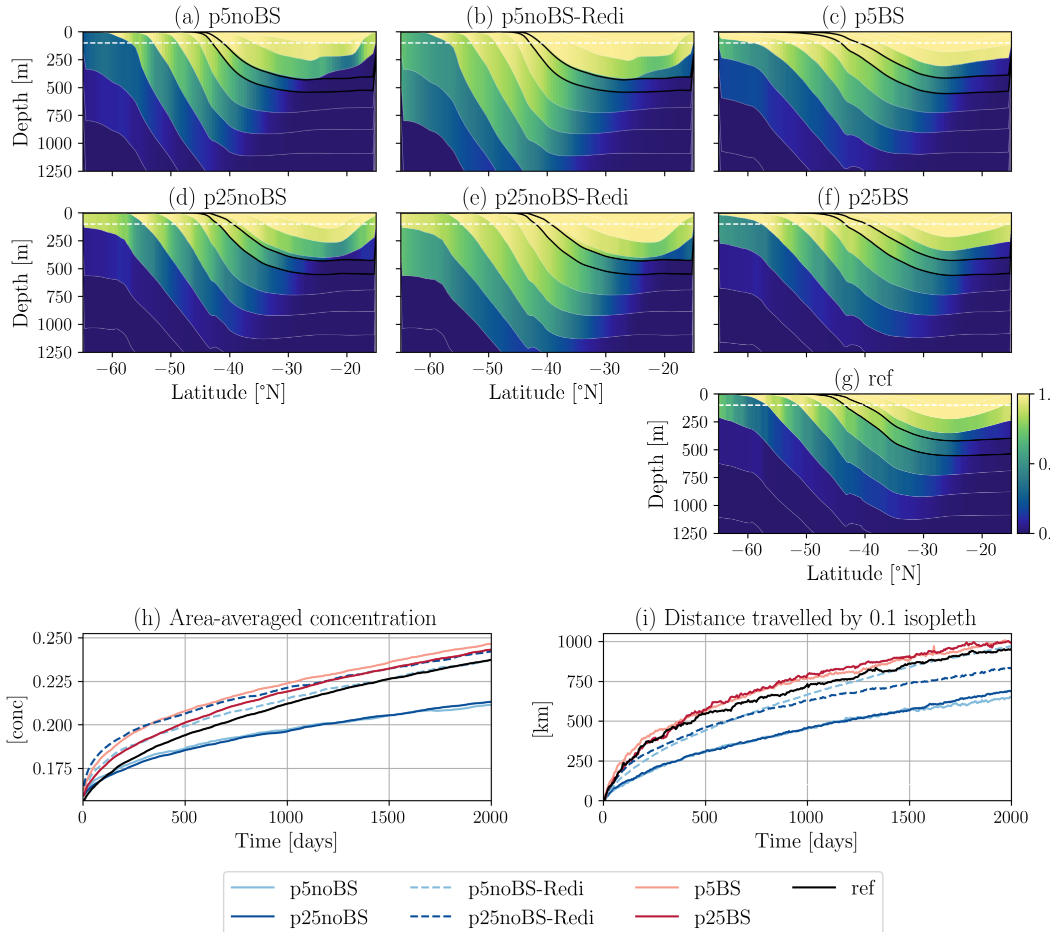

Figure 13: (a–g) Zonally averaged ventilation tracer after 2,000 days shown between −65°N and −15°N in the (a) p5noBS, (b) p5noBS-Redi, (c) p5BS, (d) p25noBS, (e) p25noBS-Redi, (f) p25BS, and (g) ref simulations. Thin white lines show zonally averaged isopycnal interfaces, and the black contoured isopycnal is the first layer to outcrop only in the Southern Ocean. Quantities on this layer are shown in (h–i): (h) the area-averaged tracer concentration and (i) the average meridional distance travelled by the 0.1 isopleth of the tracer.

centration on the deeper outcropping layers (Figure 13b, e) due to an inaccurate vertical structure for the parameterized diffusivity; this might be mitigated by a different choice of vertical structure (see Section 2.4). The p5BS and p25BS simulations show the closest resemblance to the ref simulation in terms of both growth over time and the vertical distribution of the tracer (Figure 13c, f, g, h).

The northward advance of the 0.1 tracer isopleth gives a clear indication of tracer *mixing* across the simulations (Figure 13i). The 0.1 isopleth advances into the interior more slowly for the unparameterized simulations, showing a bias of roughly 300 km after 2,000 days. Adding isopycnal tracer diffusion generally reduces this bias, although the effect of the horizontal resolution function is clearly seen in the p25noBS-Redi simulation at roughly 1,000 days, where the procession slows. The backscatter simulations show the closest resemblance to the ref simulation overall, although slightly overestimate the mean distance travelled after 2,000 days by about 30 km. These results are consistent with the findings of Abernathey and Ferreira (2015), where higher eddy activity (in their case due to stronger winds) drives enhanced ventilation through intensified isopycnal mixing.

4. Summary and discussion

We have evaluated the effect of a kinetic energy backscatter parameterization on isopycnal mixing at eddy-permitting resolutions in a basin-scale configuration of MOM6. In this study, the backscatter parameterization is formulated as a negative harmonic viscosity in the momentum equations, whose magnitude is informed by a local prognostic subgrid energy budget, and acts to reenergize eddies that are spuriously dissipated by a biharmonic viscosity. Importantly, the backscatter parameterization is not combined with additional GM or Redi parameterizations for eddy-driven overturning and eddy-induced along-isopycnal tracer diffusion, respectively. We have assessed the representation of isopycnal mixing by diagnosing the three-dimensional structure of isopycnal diffusivities via a multiple tracer inversion method.

The main results are summarized here:

1. Simulations with no mesoscale parameterization in this model, at both 1/2° and 1/4° resolutions, show subdued isopycnal mixing (Figure 6) and consequent tracer biases (Figures 12 and 13), largely as a result of subdued eddy activity (Figure 3). In these simulations, the globally integrated kinetic energy is roughly four times smaller than a coarsened 1/32° simulation (Figure 2a), and the predominantly meridional diffusivity is similarly four times too small on the global average compared to the 1/32° simulation (Figure 10d). Isopycnals are also too steep in the unparameterized simulations, due to a poorly resolved baroclinic energy cycle, which leads to inaccurate outcrop locations in the reentrant channel that mimics the Southern Ocean in the model (Figure 5).

2. Simulations employing the backscatter parameterization show elevated isopycnal diffusivities, which largely track the increases in eddy kinetic energy (compare Figures 3 and 6, and Figures 4 and 7). When compared to the 1/32° reference simulation, the results overall suggest that no supplemental isopycnal diffusion is needed in these backscatter simulations. The predominantly meridional diffusivity in the backscatter simulations is comparable to, and in some cases exceeds, that in the 1/32° simulation. The backscatter simulations are unable to match extremes in the distribution of the predominantly zonal diffusivity in the 1/32° simulation (Figure 10a); however, such extremes may arise from zonal shear flows that are unresolved at coarser resolutions, which produce locally intense along-flow transports (Figure 9). The backscatter parameterization also leads to reductions in both mean and variance biases of passive tracers (Figure 12) as well as an improved representation of an idealized ventilation tracer (Figure 13) relative to the 1/32° simulation.

3. Simulations that use a traditional isopycnal diffusion ("Redi") parameterization show reduced mean tracer biases (Figure 12) and increased uptake of the ventilation tracer (Figure 13) relative to unparameterized simulations. However, the isopycnal diffusion parameterization also diffuses the tracer signature of resolved eddy variability, leading to increases in tracer variance biases (Figure 12).

Taken together, these results indicate that isopycnal diffusivities are expected to be low where eddy activity is low, and that, by reenergizing eddies, a backscatter parameterization can lead to an improved representation of isopycnal mixing. Juricke et al. (2020) showed in a global model configuration that parameterizing backscatter can reduce tracer biases where eddy activity is better represented, while biases can *increase* in regions where eddy activity is over-intensified. An important result from the present study is that the strength of backscatter-parameterized isopycnal mixing is affected not only by the eddy kinetic energy but also by the dominant eddy length scale, as anticipated from mixing length arguments. In the 1/2° backscatter simulation, the energy-containing scale is generally larger than in the 1/32° simulation by about 10–20 km (Figure 3g), which likely occurs because the energy-containing scale in the 1/32° simulation is at or below the 1/2° grid spacing; this contributes to isopycnal diffusivities being too large at 1/2° (Figure 6i). In the 1/4° backscatter simulation, the energy-containing scale is more in line with the 1/32° simulation (Figure 3g), and isopycnal diffusivities are in turn more similar between these simulations (Section 3.2). Joint consideration should thus be given to both the eddy energy *and* eddy length scales when parameterizing isopycnal mixing via backscatter. Encouragingly, results from simulations that varied the strength of backscatter via the magnitude of the negative viscosity (Equation (5)) demonstrated that the energy-containing scale did not vary much at fixed resolution, and that increases in isopycnal diffusivities generally followed increases in eddy energy (Figure 11). These results suggest that the magnitude of the negative viscosity could be a useful knob to control the strength of isopycnal mixing in more realistic global configurations where eddy activity is partially resolved but spuriously low. Further work is, of course, needed to confirm the degree to which this holds in realistic global models, and we hope the results in the present study motivate such work.

Due to our idealized model configuration, several important effects remain to be explored to achieve implementation in realistic global models. Our model is purely adiabatic with a single thermodynamic constituent, while temperature and salinity gradients can compensate and thus coexist along isopycnals in the ocean. Recent studies (Holmes et al., 2022; Neumann & Jones, 2025) have shown that enhanced isopycnal mixing can have indirect diabatic impacts through interactions with surface buoyancy fluxes and via nonlinear equation of state effects, in particular in the Southern Ocean, thus modifying circulation and water mass transformation processes. It will thus be important to understand the dual effect of backscatter-parameterized eddies to modify stratification via adiabatic APE extraction versus diabatic effects that arise from enhanced isopycnal mixing, especially in the Southern Ocean where a backscatter parameterization already likely generates strong responses (Juricke et al., 2020; Chang et al., 2023; Yassin et al., 2025). Further work is needed to test sensitivity to other aspects of the parameterization, such as the vertical structure, which has been shown to influence the resolved stratification in idealized models (Yankovsky et al., 2024) and whose effects may differ in more realistic models. Interactions with other processes absent from the model used in this study, such as mixed layer and vertical mixing processes and their parameterizations, are another important consideration for global model implementation and warrant future attention. It would also be of interest to assess the implications of elevated tracer variability at the mesoscale via a backscatter parameterization for air–sea fluxes (Bishop et al., 2017; Gehlen et al., 2020) as well as reactive biogeochemical tracers (Lévy et al., 2014).

Finally, we note that the backscatter scheme used in this study is primarily a numerical, rather than a physical, backscatter parametrization, as it acts to counteract the excessive dissipation resulting from the biharmonic viscous closure. Recent work (Silvestri et al., 2024; Zhang et al., 2025) has suggested that improved numerics could obviate the need for an explicit viscous closure. This may reduce the spurious damping of resolved kinetic energy and thereby increase the effective resolution of eddy-permitting simulations. Even with such improved numerical schemes, however, there is likely still to be some excessive dissipation at small scales relative to a higher resolution simulation, which may affect large-scale fields because of missing energy sources for upscale cascades. A numerical backscatter parameterization could thus still be of use in this scenario (e.g., Zhang et al., 2025). Moreover, physical backscatter parameterizations which target missing *physics*, such as the energization of mesoscale flows via submesoscale inverse cascades (Steinberg et al., 2022; Garabato et al., 2022), will remain relevant as long as such processes are partially or not resolved.

Our study has demonstrated that a resolved flow, appropriately energized by a backscatter parameterization, can generate realistic isopycnal mixing. Many open questions remain regarding how to optimally implement such a parameterization in a global model to balance the various effects that increased eddy activity may have. However, backscatter parameterizations can likely contribute to a more faithful representation of mesoscale eddy activity and associated eddy-induced mixing effects in the challenging eddy-permitting regime of ocean climate models.

A. Further results for thickness-weighted eddy tracer fluxes

Here, we present equations for the thickness-weighted mean and eddy tracer variances, $\hat{c}^2$ and $\widehat{c''^2}$, that follow from Equation (11). Following these equations, we discuss the effect of the eddy tracer flux $\mathbf{F}^c$ (Equation (12)) on tracer variance in order to clarify our focus on the symmetric part of the eddy tracer flux (see Section 2.3.2).

A.1. Mean and eddy tracer variance equations

The mean tracer variance equation is found by first rewriting the TWA tracer equation (Equation (11)) in an advective form, multiplying by $\overline{h}\hat{c}$, and then making use of the averaged thickness equation (Equation (2)).

The result is

$$\partial_t\left(\overline{h}\frac{\hat{c}^2}{2}\right) + \nabla\cdot\left(\overline{h}\hat{\mathbf{u}}\frac{\hat{c}^2}{2}\right) + \nabla\cdot\left(\overline{h}\hat{c}\mathbf{F}^c\right) = \overline{h}\nabla\hat{c}\cdot\mathbf{F}^c. \tag{30}$$

The eddy tracer variance can be written as $\widehat{c''^2} = \widehat{c^2} - \hat{c}^2$ following usual Reynolds assumptions (see Young, 2012). An equation for $\widehat{c^2}$ is found by noting that c^2 also satisfies Equation (3), averaging this equation for c^2, and again applying Reynolds assumptions to simplify the triple products. Subtracting Equation (30) from the resulting equation yields the eddy tracer variance equation

$$\partial_t\left(\overline{h}\frac{\widehat{c''^2}}{2}\right) + \nabla\cdot\left(\overline{h}\hat{\mathbf{u}}\frac{\widehat{c''^2}}{2}\right) + \nabla\cdot\left(\overline{h}\frac{\widehat{\mathbf{u}''c''^2}}{2}\right) = -\overline{h}\nabla\hat{c}\cdot\mathbf{F}^c. \tag{31}$$

Equations (30) and (31) are similar to Equations (89) and (90) in Young (2012), except that Young's equations are defined in a basis which differs to the basis that defines the numerical model's coordinate system (Section 2.1) (see also Jansen et al., 2024); this difference is the reason we present these equations here.

The main point here is that the right hand sides of Equations (30) and (31) differ by a sign and sum to zero. These are the eddy-mean transfer terms in a thickness-weighted framework. As discussed next, if a flux-gradient relationship is assumed (Equation (13)), then only the symmetric part of the mixing tensor affects these eddy-mean transfer terms.

A.2. Antisymmetric and symmetric eddy tracer fluxes

Of the four degrees of freedom in the mixing tensor $\mathsf{K} \in \mathbb{R}^{2\times2}$, only one comes from the antisymmetric part $\mathsf{A} = (\mathsf{K} - \mathsf{K}^{\mathrm{T}})/2$; namely,

$$\mathsf{A} = \begin{bmatrix} 0 & \psi \\ -\psi & 0 \end{bmatrix},$$

where ψ is a scalar. The eddy flux associated with the antisymmetric part of K, i.e., $\mathbf{F}^c_{\mathsf{A}} \equiv -\mathsf{A}\nabla\hat{c}$, can therefore be written as

$$-\mathsf{A}\nabla\hat{c} = \psi\nabla^{\perp}\hat{c}, \tag{32}$$

where $\nabla^{\perp} = -\partial_y\mathbf{i} + \partial_x\mathbf{j}$. Since $\nabla\hat{c}\cdot\left(\psi\nabla^{\perp}\hat{c}\right) = 0$, Equations (30) and (31) imply that $\mathbf{F}^c_{\mathsf{A}}$ has no effect on tracer variance.

It is thus clear that only the eddy flux associated with the symmetric part of K, i.e., $\mathbf{F}^c_{\mathsf{S}} \equiv -\mathsf{S}\nabla\hat{c}$, can affect tracer variance (Equations (30) and (31)). Denoting rotation of a vector into the coordinate system defined by the orthonormal columns of U as

$$\tilde{\mathbf{a}} \equiv \mathsf{U}^{\mathrm{T}}\mathbf{a}, \tag{33}$$

then it follows that the right hand side of the mean tracer variance equation (Equation (30)) can be written as

$$\overline{h}\nabla\hat{c}\cdot\mathbf{F}^c = -\overline{h}\widetilde{\nabla\hat{c}}\cdot\left(\mathsf{D}\widetilde{\nabla\hat{c}}\right), \tag{34}$$

which is negative-definite if the entries of D, i.e., the isopycnal diffusivities (Equation (15)), are positive. When globally integrated, the right hand side of Equation (34) in fact *must* be negative to balance dissipation of tracer variance. (Dissipation is not written explicitly in Equations (30) or (31) but is achieved through the action of molecular or numerical diffusion.) The effect of S is therefore referred to as "mixing" as it acts as a global sink of mean tracer variance. It is this variance-reducing mixing that is targeted by typical isopycnal mixing parameterizations (e.g., Redi, 1982).

B. Error estimation from the Method of Multiple Tracers

Here, we describe an error estimation method for the Method of Multiple Tracers inversion described in Section 2.3.3. Since the inversion is a least squares regression, the error estimation method amounts to computing the standard errors of the coefficients (i.e., the standard deviation on the estimated coefficients) that define the least squares solution K_{lsq} (Equation (18)).

To render the overdetermined matrix equation (Equation (17)) in a more intuitive matrix-vector formulation to apply ordinary least squares results, we vectorize Equation (17) to become

$$\mathbf{F} = \mathsf{M}\mathbf{K}, \tag{35}$$

where $\mathbf{F} \equiv \text{vec}(\mathsf{F}) \in \mathbb{R}^{2m}$, $\mathbf{K} \equiv \text{vec}(\mathsf{K}) \in \mathbb{R}^4$ and $\mathsf{M} \equiv -(\mathsf{G}^{\text{T}} \bigotimes I_2) \in \mathbb{R}^{2m\times 4}$, where $\bigotimes$ is the Kronecker product and I_2 is the 2×2 identity matrix. As in Equation (18), the least squares estimates for the entries of $\mathbf{K}$ can be expressed as

$$\mathbf{K}_{\text{lsq}} = \mathsf{M}^{\dagger}\mathbf{F}, \tag{36}$$

with residuals then given by

$$\mathbf{r} = \mathbf{F} - \mathsf{M}\mathbf{K}_{\text{lsq}}. \tag{37}$$

To proceed, we assume that the residuals (i.e., errors) are independent and identically distributed as well as homoskedastic. The sample variance of the errors is then

$$s^2 = \frac{1}{2m-4}\|\mathbf{r}\|^2, \tag{38}$$

where $2m - 4$ are the statistical degrees of freedom from Equation (35), and the covariance matrix of $\mathbf{K}$ is

$$\text{cov}(\mathbf{K}) = s^2(\mathsf{M}^{\text{T}}\mathsf{M})^{-1}. \tag{39}$$

The standard errors of the entries K_i of $\mathbf{K}$ are then

$$\text{se}(K_i) = \sqrt{\left(\text{cov}(\mathbf{K})\right)_{ii}}, \tag{40}$$

for $i = 1, \ldots, 4$.

We then relate this expression for the standard errors in $\mathbf{K}$ to the standard errors in the eigenvalues $\varkappa_1$ and $\varkappa_2$ of S (Equation (15)). To do this, we first define a function $\mathbf{f}$ that maps the entries of $\mathbf{K}$ to the eigenvalues $\varkappa_1$ and $\varkappa_2$, i.e., $\mathbf{k} = \mathbf{f}(\mathbf{K})$ where $\mathbf{k} \equiv (\varkappa_1, \varkappa_2)^{\text{T}}$ and (via a simple exercise in linear algebra)

$$\varkappa_1 = \frac{K_{11} + K_{22}}{2} + \sqrt{\left(\frac{K_{11} - K_{22}}{2}\right)^2 + K_{12}^2}, \tag{41}$$

$$\varkappa_2 = \frac{K_{11} + K_{22}}{2} - \sqrt{\left(\frac{K_{11} - K_{22}}{2}\right)^2 + K_{12}^2}, \tag{42}$$

where the K_{ij} are the elements of the unvectorized matrix K. We then assume that errors propagate to first-order by

$$\text{cov}(\mathbf{k}) = \mathsf{J}\text{cov}(\mathbf{K})\mathsf{J}^{\text{T}}, \tag{43}$$

where $\mathsf{J} = \partial\mathbf{f}/\partial\mathbf{K} \in \mathbb{R}^{2\times 4}$. The standard errors in the eigenvalues are then, as in Equation (40),

$$\text{se}(\varkappa_i) = \sqrt{\left(\text{cov}(\mathbf{k})\right)_{ii}} \tag{44}$$

for $i = 1, 2$. Figure B1 shows the depth-averaged standard errors for $\varkappa_1$ and $\varkappa_2$, which can be compared to Figure 6.

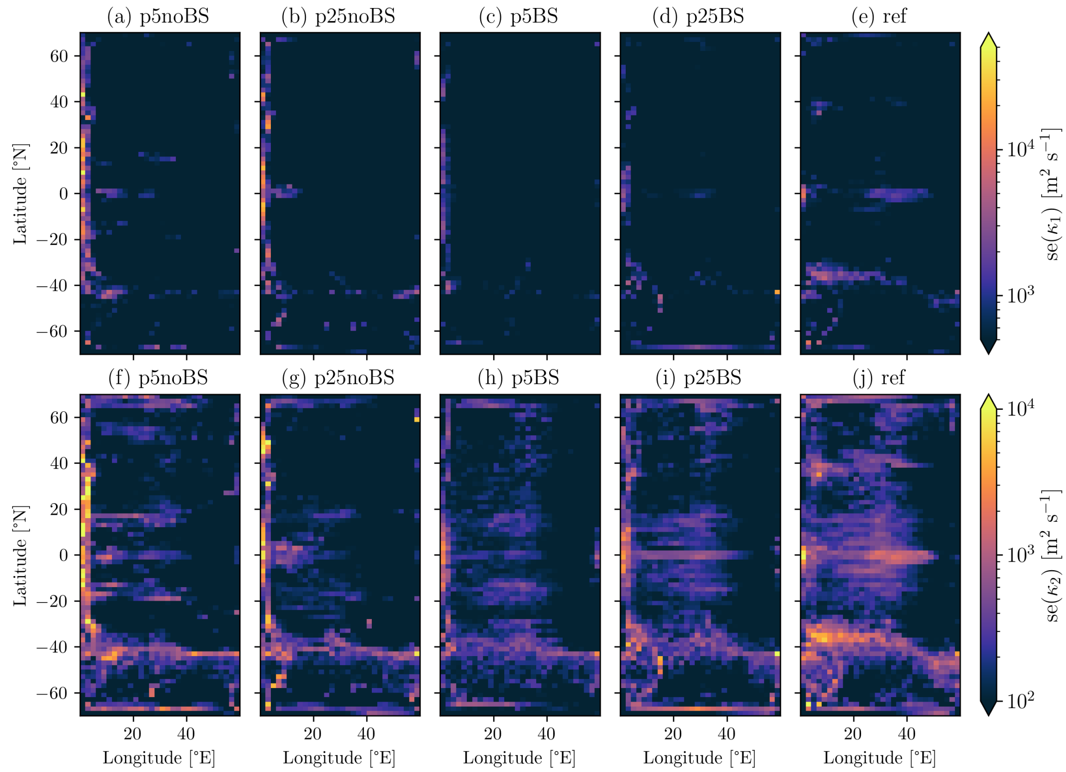

Figure B1: Depth-averaged standard errors (se) for the isopycnal diffusivities from Equation (44). (a–e) se(κ_1) (on a log color scale) in the (a) p5noBS, (b) p25noBS, (c) p5BS, (d) p25BS, and (e) ref simulations. (f–k) As in (a–e) but for se(κ_2).

Open Research Statement

The MOM6 source code used to run the simulations is frozen in a Zenodo repository (Hallberg et al., 2025). Configuration files for the simulations and python scripts to reproduce the figures in this article are also available at Pudig (2025).

Acknowledgements:
The authors acknowledge support from the National Science Foundation (NSF) and National Oceanic and Atmospheric Administration (NOAA) grant "Climate Process Team: Ocean Transport and Eddy Energy" (NSF OCE 1912357 and NOAA CVP NA19OAR4310364), and thank the entire CPT team for useful input on this work. This work was supported by the New York University IT High Performance Computing resources, services and staff expertise.

References

Abernathey, R., & Ferreira, D. (2015). Southern Ocean isopycnal mixing and ventilation changes driven by winds. *Geophysical Research Letters*, *42*(23), 10,357–10,365. doi: 10.1002/2015GL066238

Abernathey, R., Ferreira, D., & Klocker, A. (2013). Diagnostics of isopycnal mixing in a circumpolar channel. *Ocean Modelling*, *72*, 1–16. doi: 10.1016/j.ocemod.2013.07.004

Abernathey, R., Gnanadesikan, A., Pradal, M.-A., & Sundermeyer, M. A. (2022). Chapter 9 - Isopycnal mixing. In M. Meredith & A. Naveira Garabato (Eds.), *Ocean Mixing* (pp. 215–256). Elsevier.

Abernathey, R., & Marshall, J. (2013). Global surface eddy diffusivities derived from satellite altimetry. *Journal of Geophysical Research: Oceans*, *118*(2), 901–916. doi: 10.1002/jgrc.20066

Adcroft, A., Anderson, W., Balaji, V., Blanton, C., Bushuk, M., Dufour, C. O., ... Zhang, R. (2019). The GFDL Global Ocean and Sea Ice Model OM4.0: Model Description and Simulation Features. *Journal of Advances in Modeling Earth Systems*, *11*(10), 3167–3211. doi: 10.1029/2019MS001726

Andrews, D. G. (1983). A Finite-Amplitude Eliassen-Palm Theorem in Isentropic Coordinates. *Journal of the Atmospheric Sciences*, *40*(8), 1877–1883. doi: 10.1175/1520-0469(1983)040<1877:AFAEPT>2.0.CO;2

Bachman, S., & Fox-Kemper, B. (2013). Eddy parameterization challenge suite I: Eady spindown. *Ocean Modelling*, *64*, 12–28. doi: 10.1016/j.ocemod.2012.12.003

Bachman, S., Fox-Kemper, B., & Bryan, F. O. (2015). A tracer-based inversion method for diagnosing eddy-induced diffusivity and advection. *Ocean Modelling*, *86*, 1–14. doi: 10.1016/j.ocemod.2014.11.006

Balwada, D., Smith, K. S., & Abernathey, R. (2018). Submesoscale Vertical Velocities Enhance Tracer Subduction in an Idealized Antarctic Circumpolar Current. *Geophysical Research Letters*, *45*(18), 9790–9802. doi: 10.1029/2018GL079244

Balwada, D., Speer, K. G., LaCasce, J. H., Owens, W. B., Marshall, J., & Ferrari, R. (2016). Circulation and Stirring in the Southeast Pacific Ocean and the Scotia Sea Sectors of the Antarctic Circumpolar Current. *Journal of Physical Oceanography*, *46*(7), 2005–2027. doi:

10.1175/JPO-D-15-0207.1

Bishop, S. P., Small, R. J., Bryan, F. O., & Tomas, R. A. (2017). Scale Dependence of Midlatitude Air–Sea Interaction. *Journal of Climate*, *30*(20), 8207–8221. doi: 10.1175/JCLI-D-17-0159.1

Bisits, J. I., Stanley, G. J., & Zika, J. D. (2023). Can We Accurately Quantify a Lateral Diffusivity from a Single Tracer Release? *Journal of Physical Oceanography*, *53*(2), 647–659. doi: 10.1175/JPO-D-22-0145.1

Bratseth, A. M. (1998). On the estimation of transport characteristics of atmospheric data sets. *Tellus A: Dynamic Meteorology and Oceanography*, *50*(4), 451. doi: 10.3402/tellusa.v50i4.14538

Cessi, P. (2008). An Energy-Constrained Parameterization of Eddy Buoyancy Flux. *Journal of Physical Oceanography*, *38*(8), 1807–1819. doi: 10.1175/2007JPO3812.1

Chang, C.-Y., Adcroft, A., Zanna, L., Hallberg, R., & Griffies, S. M. (2023). Remote Versus Local Impacts of Energy Backscatter on the North Atlantic SST Biases in a Global Ocean Model. *Geophysical Research Letters*, *50*(21), e2023GL105757. doi: 10.1029/2023GL105757

Chelton, D. B., Schlax, M. G., & Samelson, R. M. (2011). Global observations of nonlinear mesoscale eddies. *Progress in Oceanography*, *91*(2), 167–216. doi: 10.1016/j.pocean.2011.01.002

Chen, R., McClean, J. L., Gille, S. T., & Griesel, A. (2014, August). Isopycnal Eddy Diffusivities and Critical Layers in the Kuroshio Extension from an Eddying Ocean Model. *Journal of Physical Oceanography*, *44*(8), 2191–2211. doi: 10.1175/JPO-D-13-0258.1

Chouksey, A., Griesel, A., Chouksey, M., & Eden, C. (2022). Changes in Global Ocean Circulation due to Isopycnal Diffusion. *Journal of Physical Oceanography*, *52*(9), 2219–2235. doi: 10.1175/JPO-D-21-0205.1

Cole, S. T., Wortham, C., Kunze, E., & Owens, W. B. (2015). Eddy stirring and horizontal diffusivity from Argo float observations: Geographic and depth variability. *Geophysical Research Letters*, *42*(10), 3989–3997. doi: 10.1002/2015GL063827

Couespel, D., Lévy, M., & Bopp, L. (2021). Oceanic primary production decline halved in eddy-resolving simulations of global warming. *Biogeosciences*, *18*(14), 4321–4349. doi: 10.5194/bg-18-4321-2021

Danabasoglu, G., McWilliams, J. C., & Gent, P. R. (1994). The Role of Mesoscale Tracer Transports in the Global Ocean Circulation. *Science*, *264*(5162), 1123–1126. doi: 10.1126/science.264.5162.1123

Delworth, T. L., Rosati, A., Anderson, W., Adcroft, A. J., Balaji, V., Benson, R., … Zhang, R. (2012). Simulated Climate and Climate Change in the GFDL CM2.5 High-Resolution Coupled Climate Model. *Journal of Climate*, *25*(8), 2755–2781. doi: 10.1175/JCLI-D-11-00316.1

de Szoeke, R. A., & Bennett, A. F. (1993). Microstructure Fluxes across Density Surfaces. *Journal of Physical Oceanography*, *23*(10), 2254–2264. doi: 10.1175/1520-0485(1993)023<2254:MFADS>2.0.CO;2

Eden, C., & Greatbatch, R. J. (2008). Towards a mesoscale eddy closure. *Ocean Modelling*, *20*(3), 223–239. doi: 10.1016/j.ocemod.2007.09.002

England, M. H. (1995). The Age of Water and Ventilation Timescales in a Global Ocean Model. *Journal of Physical Oceanography*, *25*(11), 2756–2777. doi: 10.1175/1520-0485(1995)025<2756:TAOWAV>2.0.CO;2

England, M. H., & Rahmstorf, S. (1999). Sensitivity of Ventilation Rates and Radiocarbon Uptake to Subgrid-Scale Mixing in Ocean Models. *Journal of Physical Oceanography*, *29*(11), 2802–2828. doi: 10.1175/1520-0485(1999)029<2802:SOVRAR>2.0.CO;2

Ferrari, R., & Nikurashin, M. (2010). Suppression of Eddy Diffusivity across Jets in the Southern Ocean. *Journal of Physical Oceanography*, *40*(7), 1501–1519. doi: 10.1175/2010JPO4278.1

Fox-Kemper, B., Adcroft, A., Böning, C. W., Chassignet, E. P., Curchitser, E., Danabasoglu, G., … Yeager, S. G. (2019). Challenges and Prospects in Ocean Circulation Models. *Frontiers in Marine Science*, *6*. doi: 10.3389/fmars.2019.00065

Fox-Kemper, B., Lumpkin, R., & Bryan, F. O. (2013). Chapter 8 - Lateral Transport in the Ocean Interior. In G. Siedler, S. M. Griffies, J. Gould, & J. A. Church (Eds.), *International Geophysics* (Vol. 103, pp. 185–209). Academic Press. doi: 10.1016/B978-0-12-391851-2.00008-8

Garabato, A. C. N., Yu, X., Callies, J., Barkan, R., Polzin, K. L., Frajka-Williams, E. E., … Griffies, S. M. (2022). Kinetic Energy Transfers between Mesoscale and Submesoscale Motions in the Open Ocean's Upper Layers. *Journal of Physical Oceanography*, *52*(1), 75–97. (Section: Journal of Physical Oceanography) doi: 10.1175/JPO-D-21-0099.1

Gehlen, M., Berthet, S., Séférian, R., Ethé, C., & Penduff, T. (2020). Quantification of Chaotic Intrinsic Variability of Sea-Air CO2 Fluxes at Interannual Timescales. *Geophysical Research Letters*, *47*(22), e2020GL088304. doi: 10.1029/2020GL088304

Gent, P. R. (2011). The Gent–McWilliams parameterization: 20/20 hindsight. *Ocean Modelling*, *39*(1), 2–9. doi: 10.1016/j.ocemod.2010.08.002

Gent, P. R., & McWilliams, J. C. (1990). Isopycnal Mixing in Ocean Circulation Models. *Journal of Physical Oceanography*, *20*(1), 150–155. doi: 10.1175/1520-0485(1990)020<0150:IMIOCM>2.0.CO;2

Gent, P. R., Willebrand, J., McDougall, T. J., & McWilliams, J. C. (1995). Parameterizing Eddy-Induced Tracer Transports in Ocean Circulation Models. *Journal of Physical Oceanography*, *25*(4), 463–474. doi: 10.1175/1520-0485(1995)025<0463:PEITTI>2.0.CO;2

Gnanadesikan, A., Bianchi, D., & Pradal, M.-A. (2013). Critical role for mesoscale eddy diffusion in supplying oxygen to hypoxic ocean waters. *Geophysical Research Letters*, *40*(19), 5194–5198. doi: 10.1002/grl.50998

Gnanadesikan, A., Pradal, M.-A., & Abernathey, R. (2015a). Exploring the isopycnal mixing and helium–heat paradoxes in a suite of Earth system models. *Ocean Science*, *11*(4), 591–605. doi: 10.5194/os-11-591-2015

Gnanadesikan, A., Pradal, M.-A., & Abernathey, R. (2015b). Isopycnal mixing by mesoscale eddies significantly impacts oceanic anthropogenic carbon uptake. *Geophysical Research Letters*, *42*(11), 4249–4255. doi: 10.1002/2015GL064100

Gnanadesikan, A., Russell, A., Pradal, M.-A., & Abernathey, R. (2017). Impact of Lateral Mixing in the Ocean on El Nino in a Suite of Fully Coupled Climate Models. *Journal of Advances in Modeling Earth Systems*, *9*(7), 2493–2513. doi: 10.1002/2017MS000917

Gough, W., & Lin, C. (1995). Isopycnal mixing and the Veronis effect in an ocean general circulation model. *Journal of Marine Research*, *53*(2).

Gower, J. F. R., Denman, K. L., & Holyer, R. J. (1980). Phytoplankton patchiness indicates the fluctuation spectrum of mesoscale oceanic structure. *Nature*, *288*(5787), 157–159. doi: 10.1038/288157a0

Griffies, S. M. (1998). The Gent–McWilliams Skew Flux. *Journal of Physical Oceanography*, *28*(5), 831–841. doi: 10.1175/1520-0485(1998)028<0831:TGMSF>2.0.CO;2

Griffies, S. M., Adcroft, A., Beadling, R. L., Bushuk, M., Chang, C.-Y., Drake, H. F., … Zhao, M. (2024). The GFDL-CM4X climate model hierarchy, Part I: model description and thermal properties. *Authorea Preprints*. doi: 10.22541/essoar.173282145.53065190/v1

Griffies, S. M., Adcroft, A., & Hallberg, R. W. (2020). A Primer on the Vertical Lagrangian-Remap Method in Ocean Models Based on Finite Volume Generalized Vertical Coordinates. *Journal of Advances in Modeling Earth Systems*, *12*(10), e2019MS001954. doi: 10.1029/2019MS001954

Griffies, S. M., & Hallberg, R. W. (2000). Biharmonic Friction with a Smagorinsky-Like Viscosity for Use in Large-Scale Eddy-Permitting Ocean Models. *Monthly Weather Review*, *128*(8), 2935–2946. doi: 10.1175/1520-0493(2000)128<2935:BFWASL>2.0.CO;2

Griffies, S. M., Winton, M., Anderson, W. G., Benson, R., Delworth, T. L., Dufour, C. O., … Zhang, R. (2015). Impacts on Ocean Heat from Transient Mesoscale Eddies in a Hierarchy of Climate Models. *Journal of Climate*, *28*(3), 10.1175/JCLI–D–14–00353.1. doi:

10.1175/JCLI-D-14-00353.1

Groeskamp, S., LaCasce, J. H., McDougall, T. J., & Rogé, M. (2020). Full-Depth Global Estimates of Ocean Mesoscale Eddy Mixing From Observations and Theory. *Geophysical Research Letters*, *47*(18), e2020GL089425. doi: 10.1029/2020GL089425

Groeskamp, S., Sloyan, B. M., Zika, J. D., & McDougall, T. J. (2017). Mixing Inferred from an Ocean Climatology and Surface Fluxes. *Journal of Physical Oceanography*, *47*(3), 667–687. doi: 10.1175/JPO-D-16-0125.1

Hallberg, R. (2013). Using a resolution function to regulate parameterizations of oceanic mesoscale eddy effects. *Ocean Modelling*, *72*, 92–103. doi: 10.1016/j.ocemod.2013.08.007

Hallberg, R., Adcroft, A., Ward, M., Marques, G., Hedstrom, K., Altuntas, A., … Jansen, M. (2025). *mpudig/MOM6-GFDL: JAMES_isopycnalmixingbackscatter.* Zenodo. doi: 10.5281/zenodo.17087553

Hewitt, H. T., Roberts, M., Mathiot, P., Biastoch, A., Blockley, E., Chassignet, E. P., … Zhang, Q. (2020). Resolving and Parameterising the Ocean Mesoscale in Earth System Models. *Current Climate Change Reports*, *6*(4), 137–152. doi: 10.1007/s40641-020-00164-w

Holmes, R. M., Groeskamp, S., Stewart, K. D., & McDougall, T. J. (2022). Sensitivity of a Coarse-Resolution Global Ocean Model to a Spatially Variable Neutral Diffusivity. *Journal of Advances in Modeling Earth Systems*, *14*(3), e2021MS002914. doi: 10.1029/2021MS002914

Iselin, C. O. (1939). The influence of vertical and lateral turbulence on the characteristics of the waters at mid-depths. *Eos, Transactions American Geophysical Union*, *20*(3), 414–417. doi: 10.1029/TR020i003p00414

Jansen, M. F., Adcroft, A., Griffies, S. M., & Grooms, I. (2024). The Averaged Hydrostatic Boussinesq Ocean Equations in Generalized Vertical Coordinates. *Journal of Advances in Modeling Earth Systems*, *16*(12), e2024MS004506. doi: 10.1029/2024MS004506

Jansen, M. F., Adcroft, A., Khani, S., & Kong, H. (2019). Toward an Energetically Consistent, Resolution Aware Parameterization of Ocean Mesoscale Eddies. *Journal of Advances in Modeling Earth Systems*, *11*(8), 2844–2860. doi: 10.1029/2019MS001750

Jansen, M. F., & Held, I. M. (2014). Parameterizing subgrid-scale eddy effects using energetically consistent backscatter. *Ocean Modelling*, *80*, 36–48. doi: 10.1016/j.ocemod.2014.06.002

Jansen, M. F., Held, I. M., Adcroft, A., & Hallberg, R. (2015). Energy budget-based backscatter in an eddy permitting primitive equation model. *Ocean Modelling*, *94*, 15–26. doi: 10.1016/j.ocemod.2015.07.015

Jones, C. S., & Abernathey, R. P. (2019). Isopycnal Mixing Controls Deep Ocean Ventilation. *Geophysical Research Letters*, *46*(22), 13144–13151. doi: 10.1029/2019GL085208

Juricke, S., Danilov, S., Koldunov, N., Oliver, M., & Sidorenko, D. (2020). Ocean Kinetic Energy Backscatter Parametrization on Unstructured Grids: Impact on Global Eddy-Permitting Simulations. *Journal of Advances in Modeling Earth Systems*, *12*(1), e2019MS001855. doi: 10.1029/2019MS001855

Juricke, S., Danilov, S., Kutsenko, A., & Oliver, M. (2019). Ocean kinetic energy backscatter parametrizations on unstructured grids: Impact on mesoscale turbulence in a channel. *Ocean Modelling*, *138*, 51–67. doi: 10.1016/j.ocemod.2019.03.009

Kiss, A. E., Hogg, A. M., Hannah, N., Boeira Dias, F., Brassington, G. B., Chamberlain, M. A., … Zhang, X. (2020). ACCESS-OM2 v1.0: a global ocean–sea ice model at three resolutions. *Geoscientific Model Development*, *13*(2), 401–442. doi: 10.5194/gmd-13-401-2020

Kjellsson, J., & Zanna, L. (2017). The Impact of Horizontal Resolution on Energy Transfers in Global Ocean Models. *Fluids*, *2*(3), 45. doi: 10.3390/fluids2030045

Klocker, A., & Abernathey, R. (2014). Global Patterns of Mesoscale Eddy Properties and Diffusivities. *Journal of Physical Oceanography*, *44*(3), 1030–1046. doi: 10.1175/JPO-D-13-0159.1

Klocker, A., Ferrari, R., & LaCasce, J. H. (2012). Estimating Suppression of Eddy Mixing by Mean Flows. *Journal of Physical Oceanography*, *42*(9), 1566–1576. doi: 10.1175/JPO-D-11-0205.1

Klocker, A., & Marshall, D. P. (2014). Advection of baroclinic eddies by depth mean flow. *Geophysical Research Letters*, *41*(10), 3517–3521. doi: 10.1002/2014GL060001

Klöwer, M., Jansen, M. F., Claus, M., Greatbatch, R. J., & Thomsen, S. (2018). Energy budget-based backscatter in a shallow water model of a double gyre basin. *Ocean Modelling*, *132*, 1–11. doi: 10.1016/j.ocemod.2018.09.006

LaCasce, J. H. (2008). Statistics from Lagrangian observations. *Progress in Oceanography*, *77*(1), 1–29. doi: 10.1016/j.pocean.2008.02.002

Larichev, V. D., & Held, I. M. (1995). Eddy Amplitudes and Fluxes in a Homogeneous Model of Fully Developed Baroclinic Instability. *Journal of Physical Oceanography*, *25*(10), 2285–2297. doi: 10.1175/1520-0485(1995)025<2285:EAAFIA>2.0.CO;2

Ledwell, J. R., Watson, A. J., & Law, C. S. (1998). Mixing of a tracer in the pycnocline. *Journal of Geophysical Research: Oceans*, *103*(C10), 21499–21529. doi: 10.1029/98JC01738

Loose, N., Marques, G. M., Adcroft, A., Bachman, S., Griffies, S. M., Grooms, I., … Jansen, M. F. (2023). Comparing Two Parameterizations for the Restratification Effect of Mesoscale Eddies in an Isopycnal Ocean Model. *Journal of Advances in Modeling Earth Systems*, *15*(12), e2022MS003518. doi: 10.1029/2022MS003518

Lumpkin, R., & Flament, P. (2001). Lagrangian statistics in the central North Pacific. *Journal of Marine Systems*, *29*(1), 141–155. doi: 10.1016/S0924-7963(01)00014-8

Lévy, M., Jahn, O., Dutkiewicz, S., Follows, M. J., & d'Ovidio, F. (2015). The dynamical landscape of marine phytoplankton diversity. *Journal of The Royal Society Interface*, *12*(111), 20150481. doi: 10.1098/rsif.2015.0481

Lévy, M., Resplandy, L., & Lengaigne, M. (2014). Oceanic mesoscale turbulence drives large biogeochemical interannual variability at middle and high latitudes. *Geophysical Research Letters*, *41*(7), 2467–2474. doi: 10.1002/2014GL059608

Mak, J., Maddison, J. R., Marshall, D. P., Ruan, X., Wang, Y., & Yeow, L. (2023). Scale-Awareness in an Eddy Energy Constrained Mesoscale Eddy Parameterization. *Journal of Advances in Modeling Earth Systems*, *15*(12), e2023MS003886. doi: 10.1029/2023MS003886

Marques, G. M., Loose, N., Yankovsky, E., Steinberg, J. M., Chang, C.-Y., Bhamidipati, N., … Zanna, L. (2022). NeverWorld2: an idealized model hierarchy to investigate ocean mesoscale eddies across resolutions. *Geoscientific Model Development*, *15*(17), 6567–6579. doi: 10.5194/gmd-15-6567-2022

Marshall, D., & Adcroft, A. (2010). Parameterization of ocean eddies: Potential vorticity mixing, energetics and Arnold's first stability theorem. *Ocean Modelling*, *32*(3), 188–204. doi: 10.1016/j.ocemod.2010.02.001

Marshall, J., Scott, J. R., Romanou, A., Kelley, M., & Leboissetier, A. (2017). The dependence of the ocean's MOC on mesoscale eddy diffusivities: A model study. *Ocean Modelling*, *111*, 1–8. doi: 10.1016/j.ocemod.2017.01.001

McDougall, T. J., & Church, J. A. (1986). Pitfalls with the Numerical Representation of Isopycnal Diapycnal Mixing.

Montgomery, R. B. (1940). The Present Evidence on the Importance of Lateral Mixing Processes in the Ocean. *Bulletin of the American Meteorological Society*, *21*(3), 87–94.

Morrison, A. K., Waugh, D. W., Hogg, A. M., Jones, D. C., & Abernathey, R. P. (2022). Ventilation of the Southern Ocean Pycnocline. *Annual Review of Marine Science*, *14*(1), 405–430. doi: 10.1146/annurev-marine-010419-011012

Neumann, N. K., & Jones, C. S. (2025). Effects of Wind and Isopycnal Mixing on Southern Ocean Surface Buoyancy Flux and Antarctic Bottom Water Formation. *Geophysical Research Letters*, *52*(7), e2024GL112133. doi: 10.1029/2024GL112133

Nummelin, A., & Isachsen, P. E. (2024). Parameterizing Mesoscale Eddy Buoyancy Transport Over Sloping Topography. *Journal of Advances* *in Modeling Earth Systems*, *16*(3), e2023MS003806. doi: 10.1029/2023MS003806

Plumb, R. A., & Mahlman, J. D. (1987). The Zonally Averaged Transport Characteristics of the GFDL General Circulation/Transport Model. *Journal of the Atmospheric Sciences*, *44*(2), 298–327. doi: 10.1175/1520-0469(1987)044<0298:TZATCO>2.0.CO;2

Pradal, M.-A., & Gnanadesikan, A. (2014). How does the Redi parameter for mesoscale mixing impact global climate in an Earth System Model? *Journal of Advances in Modeling Earth Systems*, *6*(3), 586–601. doi: 10.1002/2013MS000273

Pudig, M. (2025). *mpudig/JAMES_isopycnalmixingbackscatter: Submission.* Zenodo. doi: 10.5281/zenodo.17088720

Redi, M. H. (1982). Oceanic Isopycnal Mixing by Coordinate Rotation. *Journal of Physical Oceanography*, *12*(10), 1154–1158. doi: 10.1175/1520-0485(1982)012<1154:OIMBCR>2.0.CO;2

Resplandy, L., Lévy, M., Madec, G., Pous, S., Aumont, O., & Kumar, D. (2011). Contribution of mesoscale processes to nutrient budgets in the Arabian Sea. *Journal of Geophysical Research: Oceans*, *116*(C11). doi: 10.1029/2011JC007006

Sijp, W. P., & England, M. H. (2009). The Control of Polar Haloclines by Along-Isopycnal Diffusion in Climate Models. *Journal of Climate*, *22*(3), 486–498. doi: 10.1175/2008JCLI2513.1

Silvestri, S., Wagner, G. L., Campin, J.-M., Constantinou, N. C., Hill, C. N., Souza, A., & Ferrari, R. (2024). A New WENO-Based Momentum Advection Scheme for Simulations of Ocean Mesoscale Turbulence. *Journal of Advances in Modeling Earth Systems*, *16*(7), e2023MS004130. doi: 10.1029/2023MS004130

Smith, K. S. (2005). Tracer transport along and across coherent jets in two-dimensional turbulent flow. *Journal of Fluid Mechanics*, *544*(-1), 133. doi: 10.1017/S0022112005006750

Smith, K. S., & Marshall, J. (2009). Evidence for Enhanced Eddy Mixing at Middepth in the Southern Ocean. *Journal of Physical Oceanography*, *39*(1), 50–69. doi: 10.1175/2008JPO3880.1

Solomon, H. (1971). On the Representation of Isentropic Mixing in Ocean Circulation Models. *Journal of Physical Oceanography*, *1*(3), 233–234. doi: 10.1175/1520-0485(1971)001<0233:OTROIM>2.0.CO;2

Steinberg, J. M., Cole, S. T., Drushka, K., & Abernathey, R. P. (2022). Seasonality of the Mesoscale Inverse Cascade as Inferred from Global Scale-Dependent Eddy Energy Observations. *Journal of Physical Oceanography*, *52*(8), 1677–1691. doi: 10.1175/JPO-D-21-0269.1

Stewart, A. L., & Thompson, A. F. (2015). Eddy-mediated transport of warm Circumpolar Deep Water across the Antarctic Shelf Break. *Geophysical Research Letters*, *42*(2), 432–440. doi: 10.1002/2014GL062281

Storer, B. A., Buzzicotti, M., Khatri, H., Griffies, S. M., & Aluie, H. (2022). Global energy spectrum of the general oceanic circulation. *Nature Communications*, *13*(1), 5314. doi: 10.1038/s41467-022-33031-3

Taylor, G. I. (1953). The dispersion of matter in turbulent flow through a pipe. *Proceedings of the Royal Society of London. Series A. Mathematical and Physical Sciences*, *223*(1155), 446–468. doi: 10.1098/rspa.1954.0130

Thompson, A. F., Heywood, K. J., Schmidtko, S., & Stewart, A. L. (2014). Eddy transport as a key component of the Antarctic overturning circulation. *Nature Geoscience*, *7*(12), 879–884. doi: 10.1038/ngeo2289

Thompson, A. F., & Young, W. R. (2006). Scaling Baroclinic Eddy Fluxes: Vortices and Energy Balance. *Journal of Physical Oceanography*, *36*(4), 720–738. doi: 10.1175/JPO2874.1

Tulloch, R., Ferrari, R., Jahn, O., Klocker, A., LaCasce, J., Ledwell, J. R., … Watson, A. (2014). Direct Estimate of Lateral Eddy Diffusivity Upstream of Drake Passage. *Journal of Physical Oceanography*, *44*(10), 2593–2616. doi: 10.1175/JPO-D-13-0120.1

Uchida, T., Balwada, D., P. Abernathey, R., A. McKinley, G., K. Smith, S., & Lévy, M. (2020). Vertical eddy iron fluxes support primary production in the open Southern Ocean. *Nature Communications*, *11*(1), 1125. doi: 10.1038/s41467-020-14955-0

Veronis, G. (1975). The role of models in tracer studies. *Numerical Models of Ocean Circulation*, 133–146.

Vollmer, L., & Eden, C. (2013). A global map of meso-scale eddy diffusivities based on linear stability analysis. *Ocean Modelling*, *72*, 198–209. doi: 10.1016/j.ocemod.2013.09.006

Wei, H., & Wang, Y. (2021). Full-Depth Scalings for Isopycnal Eddy Mixing Across Continental Slopes Under Upwelling-Favorable Winds. *Journal of Advances in Modeling Earth Systems*, *13*(6), e2021MS002498. doi: 10.1029/2021MS002498

Whalen, C. B., MacKinnon, J. A., & Talley, L. D. (2018). Large-scale impacts of the mesoscale environment on mixing from wind-driven internal waves. *Nature Geoscience*, *11*(11), 842–847. doi: 10.1038/s41561-018-0213-6

Yankovsky, E., Bachman, S., Smith, K. S., & Zanna, L. (2024). Vertical Structure and Energetic Constraints for a Backscatter Parameterization of Ocean Mesoscale Eddies. *Journal of Advances in Modeling Earth Systems*, *16*(7), e2023MS004093. doi: 10.1029/2023MS004093

Yankovsky, E., Zanna, L., & Smith, K. S. (2022). Influences of Mesoscale Ocean Eddies on Flow Vertical Structure in a Resolution-Based Model Hierarchy. *Journal of Advances in Modeling Earth Systems*, *14*(11), e2022MS003203. doi: 10.1029/2022MS003203

Yassin, H., Marques, G. M., & Grooms, I. (2025). Balancing Backscatter and Diffusion in a 1/4° Forced Global Ocean Model. *Authorea Preprints*. doi: 10.22541/essoar.175700044.45098278/v1

Young, W. R. (2012). An Exact Thickness-Weighted Average Formulation of the Boussinesq Equations. *Journal of Physical Oceanography*, *42*(5), 692–707. doi: 10.1175/JPO-D-11-0102.1

Zhang, W., Griffies, S. M., Hallberg, R. W., Kuo, Y.-H., & Wolfe, C. L. P. (2024). The Role of Surface Potential Vorticity in the Vertical Structure of Mesoscale Eddies in Wind-Driven Ocean Circulations. *Journal of Physical Oceanography*, *54*(6), 1243–1266. doi: 10.1175/JPO-D-23-0203.1

Zhang, W., Kuo, Y.-H., Silvestri, S., Adcroft, A., Hallberg, R. W., & Griffies, S. M. (2025). A WENO finite-volume scheme for the evolution of potential vorticity in isopycnal ocean models. *Authorea Preprints*. doi: 10.22541/essoar.175339141.10871701/v1

Zhang, W., & Wolfe, C. L. P. (2022). On the Vertical Structure of Oceanic Mesoscale Tracer Diffusivities. *Journal of Advances in Modeling Earth Systems*, *14*(6), e2021MS002891. doi: 10.1029/2021MS002891

Zika, J. D., Sallée, J.-B., Meijers, A. J. S., Naveira-Garabato, A. C., Watson, A. J., Messias, M.-J., & King, B. A. (2020). Tracking the spread of a passive tracer through Southern Ocean water masses. *Ocean Science*, *16*(2), 323–336. doi: 10.5194/os-16-323-2020

Journal of Advances in Modeling Earth Systems

RESEARCH ARTICLE

Parameterizing isopycnal mixing via kinetic energy backscatter in an eddy-permitting ocean model

Matthew P. Pudig[1], **Wenda Zhang**[3], **K. Shafer Smith**[1], **Laure Zanna**[1,2]

[1]Center for Atmosphere Ocean Science, Department of Mathematics, Courant Institute of Mathematical Sciences, New York University, New York, NY, USA [2]Center for Data Science, New York University, New York, NY, USA [3]Program in Atmospheric and Oceanic Sciences, Princeton University, Princeton, NJ, USA

Key Points:

- Eddy-permitting simulations with no mesoscale parameterization exhibit isopycnal mixing biases in a basin-scale ocean model
- Eddies energized via backscatter can generate realistic isopycnal mixing without additional isopycnal tracer diffusion
- Comparisons to traditional isopycnal tracer diffusion suggest that parameterizing backscatter is preferred in an eddy-permitting regime

Correspondence to:
Matthew Pudig,
matthew.pudig@nyu.edu

Citation:
Your citation here.

Abstract Representing mesoscale turbulence in eddy-permitting ocean models raises challenges for climate simulations; in such models, eddies and their associated energy and transport effects are resolved either marginally or only over parts of the domain. Kinetic energy backscatter parameterizations have recently shown promise as both a momentum *and* a buoyancy closure for partially resolved mesoscale turbulence—energizing eddies which can themselves maintain accurate large-scale stratification by slumping steep isopycnals. However, it has not been systematically explored whether such backscatter parameterizations can also serve as a closure for tracer mixing along isopycnals. Here, we present simulations using GFDL-MOM6 in an idealized basin-scale configuration to assess whether isopycnal mixing is improved, at 1/2° and 1/4° eddy-permitting resolutions, through the addition of a backscatter parameterization. We assess the representation of isopycnal mixing principally through diagnosing the three-dimensional structure of isopycnal diffusivities via a multiple tracer inversion method. Isopycnal mixing via backscatter alone shows significant improvement and closely resembles a 1/32° eddy-resolving simulation. Backscatter-parameterized mixing also outperforms simulations with no mesoscale parameterization or with an isopycnal diffusion parameterization alone, with the latter damping the tracer signature of partially resolved eddy variability. Simulations that vary the magnitude of backscatter show that increases in isopycnal diffusivities largely track increases in eddy energy. Our results suggest that parameterizing backscatter can plausibly capture key mesoscale physics in a unified framework: the inverse cascade of kinetic energy, the slumping of steep isopycnals, and the along-isopycnal mixing of tracers.

Plain Language Summary Turbulent ocean currents ("eddies") are an important component of Earth's ocean and climate system. Eddies play a major role in turbulently mixing quantities such as temperature, salinity, and oxygen along surfaces of constant density in the ocean, known as isopycnals. However, eddies are only marginally resolved by state-of-the-art numerical ocean and climate models. Marginally resolved eddies are not energetic enough, which can lead to weak large-scale currents as well as inaccurate temperature, salinity, and oxygen distributions. In this study, we show that making eddies more energetic, in a manner consistent with ocean dynamics, can improve the representation of along-isopycnal mixing in a numerical model that marginally resolves eddies. The improved along-isopycnal mixing in this model compares well to that in a high-resolution simulation where eddies are fully resolved. Our results suggest that energizing eddies may help to improve the representation of along-isopycnal mixing in more realistic global ocean and climate models.

1. Introduction

Mesoscale turbulence—with a horizontal scale of order 10–100 km, varying as a function of latitude, depth, and stratification—is a ubiquitous feature of Earth's ocean (Chelton et al., 2011; Storer et al., 2022). It plays critical roles in driving the ocean's large-scale state (e.g., J. Marshall et al., 2017; Whalen et al., 2018); setting water mass distributions (e.g., Danabasoglu et al., 1994; Thompson et al., 2014); transporting heat, salt, carbon, and other tracers (e.g., England & Rahmstorf, 1999; Resplandy et al., 2011; Gnanadesikan et al., 2015b; Stewart & Thompson, 2015; Griffies et al., 2024); and modulating ocean ecosystems (e.g., Gower et al., 1980; Lévy et al., 2015; Uchida et al., 2020; Couespel et al., 2021). As the ocean is strongly stratified in density, turbulent stirring at the mesoscale and the resultant homogenization of oceanic tracers ("mixing") occur preferentially along surfaces of constant neutral density ("isopycnal") (Iselin, 1939; Montgomery, 1940;

Abernathey et al., 2022). Isopycnal mixing is largely unresolved in coarse-resolution global ocean models (1° or coarser), as is the case for other mesoscale processes. Accounting for the net effects of these processes via parameterizations is leading order for ensuring model fidelity (Fox-Kemper et al., 2019; Hewitt et al., 2020). As modern global ocean models increasingly adopt a horizontal grid spacing that "permits" the mesoscale—that is, only marginally or only over parts of the domain—there is a pressing need to revisit the mesoscale parameterizations designed for coarse resolutions; in this "eddy-permitting" regime, these parameterizations may no longer be appropriate (e.g., Hallberg, 2013), while the absence of any parameterization may contribute to model biases (e.g., Griffies et al., 2015). In this study, we address the problem of parameterizing isopycnal mixing in such a regime.

In coarse-resolution ocean models, isopycnal mixing is typically parameterized by a rotated diffusion operator, introduced by Solomon (1971) and Redi (1982), oriented to align with local isopycnals with a prescribed isopycnal diffusion ("Redi") coefficient κ_{Redi}; this ensures mixing across isopycnals remains small thereby minimizing the "Veronis effect" (Veronis, 1975; McDougall & Church, 1986; Gough & Lin, 1995). The appropriate magnitude for κ_{Redi}, however, is poorly constrained, and differences in its magnitude have potentially significant impacts on climate-relevant simulations (e.g., Sijp & England, 2009; Gnanadesikan et al., 2013, 2015a, 2017; Jones & Abernathey, 2019; Chouksey et al., 2022). In coupled climate model simulations, varying κ_{Redi} between 400 $m^2\ s^{-1}$ and 2400 $m^2\ s^{-1}$ has been shown to induce global sea surface temperature changes of roughly 1°C and regional variations as large as 7°C (Pradal & Gnanadesikan, 2014), as well as a roughly 15% difference in the uptake of historical anthropogenic carbon (Gnanadesikan et al., 2015b). An appropriate spatial structure for κ_{Redi} may also be a source of uncertainty in coarse-resolution ocean models, where introducing three-dimensional spatial structure into κ_{Redi} has been shown to reduce tracer biases and alter the global overturning circulation (Holmes et al., 2022). Uncertainty around appropriate values for κ_{Redi} is due in part to the widely varying observational estimates for isopycnal diffusivities from tracer release experiments (Ledwell et al., 1998; Tulloch et al., 2014; Zika et al., 2020; Bisits et al., 2023), float dispersion (Lumpkin & Flament, 2001; LaCasce, 2008; Balwada et al., 2016), and satellite altimetry (Abernathey & Marshall, 2013; Klocker & Abernathey, 2014). Estimates range from local values of order 10,000 $m^2\ s^{-1}$ in energetic western boundary current regions (Cole et al., 2015) to globally averaged values of order 10 $m^2\ s^{-1}$ (Groeskamp et al., 2017). In sum, specifying an appropriate magnitude and spatial structure for isopycnal diffusion is a source of uncertainty in coarse-resolution global ocean models. Further uncertainty is introduced when ocean models adopt eddy-permitting resolutions, as it is unclear whether isopycnal diffusion remains an appropriate parameterization: should κ_{Redi} simply be scaled down as horizontal resolution is increased and eddies become more resolved (e.g., Kjellsson & Zanna, 2017; Kiss et al., 2020)? Or should the parameterization be turned off altogether once eddies are deemed sufficiently resolved (e.g., Delworth et al., 2012; Adcroft et al., 2019)? The present study instead examines a possible alternative parameterization for isopycnal mixing in the eddy-permitting regime.

The other essential effect of mesoscale turbulence parameterized at coarse resolutions is the adiabatic slumping of steep isopycnals—mimicking the unresolved restratifying effect of baroclinic instability, the primary generation mechanism for mesoscale eddies. This is typically parameterized by the Gent-McWilliams (GM) parameterization (Gent & McWilliams, 1990; Gent et al., 1995), and in coarse-resolution simulations GM is essential for maintaining accurate large-scale stratification and circulation (Danabasoglu et al., 1994; Gent, 2011). The scheme involves the prescription of a GM coefficient κ_{GM}, with units of a diffusivity, and typically the GM and Redi schemes are implemented together (Griffies, 1998), with some models making the choice that $\kappa_{\text{GM}} = \kappa_{\text{Redi}}$ despite theory and modeling results suggesting they should in general differ (Smith & Marshall, 2009; Abernathey et al., 2013; Vollmer & Eden, 2013). At eddy-permitting resolutions, however, it has long been recognized that GM can have unwanted effects, damping partially resolved mesoscale flows (Hallberg, 2013), although approaches to remedy this have been proposed (Mak et al., 2023).

Because of this lack of a clear path forward with the extant coarse-resolution parameterizations, an increasing amount of attention has been directed towards developing parameterizations specific to the eddy-permitting regime. In particular, when the mesoscale is marginally resolved and a viscous dissipative closure is used (generally necessary for numerical stability to ensure dissipation of enstrophy, but not energy, at the grid scale), there can exist a *spurious* depletion of resolved eddy kinetic energy (EKE) (Jansen & Held, 2014). This is due to a lack of scale separation between the eddy and viscous scales, resulting in a depletion of eddy energy close to the grid scale and thus reduced energy at all scales because of an incompletely resolved inverse cascade. One promising method to remedy this spurious energy dissipation is the use of a prognostic budget for subgrid mesoscale eddy kinetic energy (MEKE) (Cessi, 2008; Eden & Greatbatch, 2008; D. Marshall & Adcroft, 2010; Jansen et al., 2019), which can then be recycled to the resolved scales to mimic the energy "backscatter" from small to large scales associated with an inverse cascade (Jansen & Held, 2014; Jansen et al., 2015; Klöwer et al., 2018; Juricke et al., 2019; Jansen et al., 2019; Juricke et al., 2020; Yankovsky et al., 2024). Early proposals for an energy budget-based backscatter scheme employed GM concurrently, alongside the biharmonic viscous closure and a negative harmonic viscosity to represent backscatter (Jansen et al., 2019). In this case, GM served as a source for subgrid MEKE as GM models the conversion of mean available potential energy (APE) to EKE. Recent work has suggested, however, that backscatter alone can achieve both the EKE and APE effects of the unresolved mesoscale turbulence in an eddy-permitting regime (Yankovsky et al., 2024). Yankovsky et al. (2024) found specifically, using a basin-scale ocean model in an idealized configuration, that a backscatter parameterization could both sufficiently elevate resolved EKE and, through energizing eddies that then extract mean APE, relax overly steep isopycnals with GM turned off altogether. These results thus suggest that a backscatter parameterization can plausibly replace the need for GM in an eddy-permitting regime. However, they do not address whether such a backscatter parameterization also eliminates the need for an isopycnal diffusion parameterization, as suggested by Redi (1982).

The primary goal of this study is to determine whether a kinetic energy backscatter parameterization can generate sufficient isopycnal mixing, thereby eliminating the need for supplemental isopycnal diffusion, in the eddy-permitting regime. Secondary goals include evaluating whether backscatter-driven isopycnal mixing outperforms a traditional isopycnal diffusion parameterization as well as quantifying biases that arise when no mesoscale parameterization is used at these resolutions. Towards the first goal, we test the hypothesis that no supplemental isopycnal diffusion parameterization is necessary when resolved eddies are sufficiently energized via an appropriate backscatter parameterization. We test this hypothesis using an idealized adiabatic ocean model (Marques et al., 2022), designed to serve as a testbed for mesoscale parameterization, with the backscatter scheme detailed in Yankovsky et al. (2024). The results we present suggest three main conclusions when compared to a high-resolution reference simulation: (i) that eddy-permitting simulations with no mesoscale parameterization show subdued levels of isopycnal mixing and consequent biases in tracer distributions relative to the reference simulation, (ii) that a backscatter parameterization can generate realistic isopycnal mixing to match the reference simulation, and (iii) that a traditional isopycnal diffusion parameterization is largely undesirable at eddy-permitting resolutions as it damps the tracer signature of resolved eddy variability. This study thus presents a proof of concept for a mesoscale backscatter parameterization that unifies the key physics one hopes to parameterize at eddy-permitting resolutions: a well-resolved inverse cascade, the slumping of steep isopycnals, and the along-isopycnal mixing of tracers.

In section 2, we introduce the model and backscatter parameterization, and outline the method used to diagnose the three-dimensional structure of isopycnal diffusivities in simulations with this model. Section 3 evaluates the simulations, comparing 1/2° and 1/4° eddy-permitting simulations to a 1/32° eddy-resolving simulation. Section 4 concludes and discusses the results in the context of guiding parameterization development for global ocean models.

2. Methods

2.1. Model configuration

We use the GFDL Modular Ocean Model version 6 (MOM6) in the NeverWorld2 (NW2) configuration, detailed in Marques et al. (2022). NW2 is a hydrostatic, Boussinesq, and fully adiabatic configuration with an isopycnal vertical coordinate of 15 layers. The model domain is a 60°–wide sector, extending from 70°S to 70°N, with a southern reentrant channel representing the Southern Ocean. The model is forced by a meridionally-varying, zonally- and temporally-constant wind stress at the surface (Figure 1a). The model geometry includes idealized continental shelves on all sides of the domain (except in the channel) as well as a topographic ridge extending through the middle of the domain—a simplified mid-Atlantic ridge—and a semi-circular ridge centered in the channel's western opening—a simplified Scotia Arc (Figure 1b).

The NW2 configuration solves the stacked shallow-water equations, which describe equations of motion for the horizontal velocity $\mathbf{u}_n \equiv u_n\mathbf{i} + v_n\mathbf{j}$ and thickness h_n in layers $1 \leq n \leq N$ (here $N = 15$) of constant

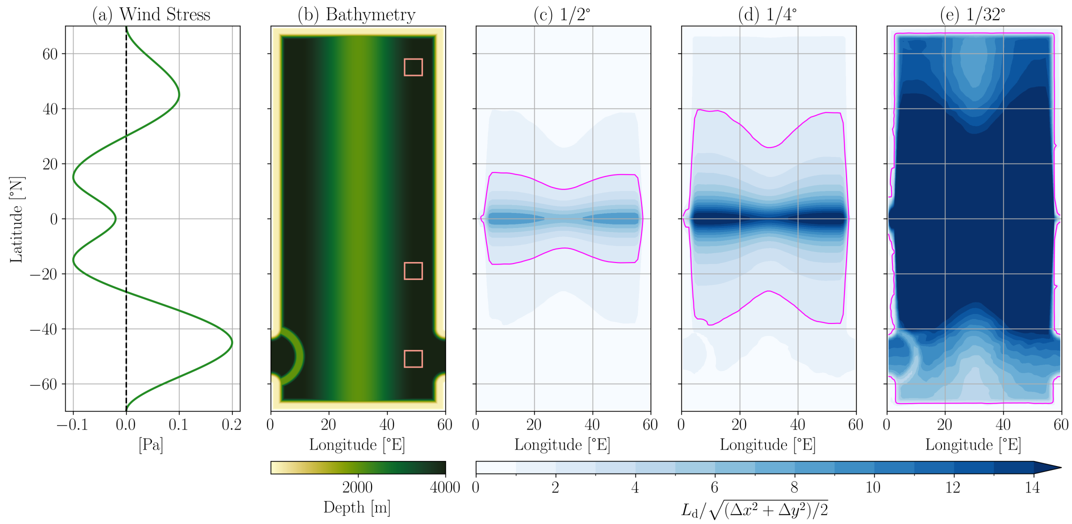

Figure 1: NeverWorld2 model configuration summary. (a) Zonal wind stress forcing. (b) Bathymetry. The boxes in (b) are regions where vertical structures are analyzed in Figure 8. (c–e) The ratio $L_\mathrm{d}/\sqrt{(\Delta x^2+\Delta y^2)/2}$, where L_d is the first baroclinic Rossby deformation radius and $\Delta x, \Delta y$ are, respectively, the zonal and meridional grid spacings for (c) 1/2°, (d) 1/4°, and (e) 1/32° horizontal resolutions. The pink isoline in (c–e) indicates where $L_\mathrm{d}/\sqrt{(\Delta x^2+\Delta y^2)/2} = 2$, which is an approximate cut-off criterion for whether mesoscale eddies are resolved (Hallberg, 2013).

density ρ_n (suppressing layer index n herein). In vector-invariant form, these equations are

$$\partial_t \mathbf{u} + (f+\zeta)\mathbf{k}\times\mathbf{u} + \nabla(K+M) = \mathbf{F}_v + \mathbf{F}_h, \tag{1}$$
$$\partial_t h + \nabla\cdot(h\mathbf{u}) = 0. \tag{2}$$

Here, $\nabla \equiv \nabla_\rho = \mathbf{i}\partial_x|_\rho + \mathbf{j}\partial_y|_\rho$ is the two-dimensional horizontal gradient operator at constant density; f is the Coriolis parameter; ζ is the relative vorticity; K is the kinetic energy per unit mass; M is the shallow-water Montgomery potential; $\mathbf{F}_v$ represents vertical stresses, including the surface wind stress, a background kinematic vertical viscosity, and a bottom stress following a quadratic drag law; and $\mathbf{F}_h$ represents horizontal stresses, including a biharmonic viscosity and, if present, a negative harmonic viscosity to represent backscatter (detailed in Section 2.2). Further details on the NW2 configuration, including specific parameter choices, can be found in Marques et al. (2022).

An evolution equation is also solved for tracer concentration c_n in each layer (again suppressing layer index n), which in its concentration-conserving, thickness-weighted form (Griffies et al., 2020; Loose et al., 2023) is

$$\partial_t(hc) + \nabla\cdot(h\mathbf{u}c) = 0. \tag{3}$$

In this study, we consider only passive tracers whose dynamics do not feed back on the flow. If an isopycnal diffusion parameterization is used then it is added to the right hand side of Equation (3) with diffusion coefficient κ_Redi (see Section 2.4); otherwise, implicit (numerical) diffusion that arises from discretizing the advection term serves to dissipate tracer variance at the grid scale.

2.2. Backscatter parameterization

The backscatter parameterization, designed to reenergize mesoscale turbulence at eddy-permitting resolution, is strictly only a closure in the momentum equation (Equation 1). The main thrust of this study is to evaluate whether, by energizing eddies, backscatter also enhances tracer mixing along isopycnals, thus potentially obviating the need for an additional eddy closure in the tracer equation (Equation 3).

The parameterization is identical to that detailed in Yankovsky et al. (2024) except for the choice of prescribed vertical structure (Equation 8). We thus describe only its salient features as well as the novel vertical structure parameterization used here; the reader is referred to Yankovsky et al. (2024) for further details. The horizontal stresses in Equation (1) comprise two terms; namely,

$$\mathbf{F}_h = -\nabla \cdot \left[\nu_4 \nabla(\nabla^2 \mathbf{u})\right] + \nabla \cdot (\nu_2 \nabla \mathbf{u}). \tag{4}$$

The dissipative biharmonic viscosity $\nu_4 > 0$ is set via a Smagorinsky scheme (Griffies & Hallberg, 2000; Marques et al., 2022). The harmonic viscosity ν_2, which is negative to represent backscatter, is set by

$$\nu_2(x, y, z, t) = -c_{\text{bs}} \sqrt{2e(x, y, t)} L_{\text{mix}}(x, y, t) \phi(x, y, z, t). \tag{5}$$

The nondimensional constant $c_{\text{bs}} > 0$ is used to tune the parameterization (see Section 2.4). The vertically averaged subgrid mesoscale eddy kinetic energy (MEKE) $e = e(x, y, t)$ informs the local magnitude of backscatter and is set via a prognostic MEKE budget following a similar proposal of Jansen et al. (2019), namely

$$\partial_t e = \dot{e}_{\text{smag}} - \dot{e}_{\text{bs}} - \dot{e}_{\text{diss}} - \dot{e}_{\text{adv}}, \tag{6}$$

where $\dot{e}_{\text{smag}}$ is the energy removed from the resolved flow by the biharmonic Smagorinsky viscosity, $\dot{e}_{\text{bs}}$ is the energy returned to the resolved flow by the negative harmonic viscosity, $\dot{e}_{\text{diss}}$ is the frictional dissipation of MEKE by quadratic drag, and $\dot{e}_{\text{adv}}$ represents horizontal transport of MEKE parameterized as advection by the vertically averaged resolved flow and diffusion (see Jansen et al., 2019).

The subgrid eddy mixing length $L_{\text{mix}} = L_{\text{mix}}(x, y, t)$ in Equation (5) is defined as

$$L_{\text{mix}} = \min(L_\Delta, L_{\beta^*}), \tag{7}$$

where L_Δ is the local horizontal grid spacing and $L_{\beta^*}^2 = \sqrt{2e}/\beta^*$ is a subgrid Rhines scale that takes into account both planetary and topographic vorticity gradients, i.e., $\beta^* = |\beta \mathbf{j} - (f_0/H)\nabla H|$, where $\beta = \partial_y f$ and H is the local depth (Figure 1b); taking the minimum of several candidate mixing length scales is motivated by Jansen et al. (2015) (see also the discussion in Nummelin & Isachsen, 2024).

The subgrid eddy vertical structure $\phi = \phi(x, y, z, t)$ in Equation (5) is based on surface quasi-geostrophic dynamics following Zhang et al. (2024), with

$$\phi(x, y, z, t) = e^{c_{\exp} z_s / L_{\text{mix}}}, \tag{8}$$

where $c_{\exp}$ is a nondimensional constant used to tune the surface-intensification of the vertical structure (see Section 2.4), $z_s(z) = -\int_z^0 N(z')/|f| dz'$ is a stretched vertical coordinate (N is the buoyancy frequency) and L_{mix} is from Equation (7). This formulation differs slightly to that presented in Zhang et al. (2024) in its definition of the "energy containing wavenumber," which here is taken to be the inverse of L_{mix} (multiplied by $c_{\exp}$). This vertical structure parameterization is the main difference to the simulations presented in Yankovsky et al. (2024), who used a vertical structure based on an equivalent barotropic mode. We choose to use the vertical structure parameterization of Zhang et al. (2024) as (i) it leads to slightly better overall results in our parameterized simulations, and (ii) it is the vertical structure being implemented for use in a backscatter parameterization in GFDL's ESM4.5.

2.3. Diagnosing isopycnal diffusivities

We evaluate the effect of this backscatter parameterization on tracers by diagnosing the three-dimensional structure of isopycnal diffusivities associated with eddy tracer fluxes and mean tracer gradients. Doing so in an isopycnal model leads naturally to the thickness-weighted average (TWA) formulation (e.g., Andrews, 1983; de Szoeke & Bennett, 1993; Young, 2012; Loose et al., 2023; Jansen et al., 2024). Diagnosing diffusivities from the resultant flux-gradient statistics is also a non-trivial task in numerical models. Here, we employ the Method of Multiple Tracers to diagnose robust estimates of isopycnal diffusivities in our simulations (Plumb & Mahlman, 1987; Bratseth, 1998; Bachman & Fox-Kemper, 2013; Fox-Kemper et al., 2013; Abernathey et al., 2013; Bachman et al., 2015; Wei & Wang, 2021; Zhang & Wolfe, 2022).

2.3.1. Defining the thickness-weighted average

Denoting $\overline{(\cdot)}$ as an appropriate Reynolds averaging operator (defined in Section 3.2) and averaging the thickness-weighted tracer equation (Equation (3)) naturally gives rise to the TWA, defined as

$$\hat{c} \equiv \frac{\overline{hc}}{\overline{h}}, \tag{9}$$

with eddy terms defined as deviations from this average

$$c'' \equiv c - \hat{c}. \tag{10}$$

The TWA tracer equation is then

$$\partial_t\left(\overline{h}\hat{c}\right) + \nabla \cdot \left(\overline{h}\hat{\mathbf{u}}\hat{c}\right) = -\nabla \cdot \left(\overline{h}\mathbf{F}^c\right), \tag{11}$$

where

$$\mathbf{F}^c \equiv \widehat{\mathbf{u}''c''} \tag{12}$$

is the eddy tracer flux in a thickness-weighted framework. The TWA is key to retaining the eddy tracer flux within the divergence. Mean and eddy tracer variance equations that follow from Equation (11) are presented in Appendix A.

2.3.2. Defining the mixing tensor

A common assumption when studying and parameterizing eddy fluxes is that the eddy tracer flux (Equation (12)) can be written as a mixing tensor K times the mean tracer gradient, i.e.,

$$\widehat{\mathbf{u}''c''} \equiv -\mathsf{K}\nabla\hat{c}, \quad \mathsf{K} \in \mathbb{R}^{2\times 2}. \tag{13}$$

If K is symmetric and positive-definite then the effect of Equation (13) in Equation (11) is that of down-gradient diffusion along isopycnals, which is the effect targeted by typical isopycnal diffusion parameterizations (Redi, 1982). In general, K is not symmetric and positive-definite; however, it can always be uniquely decomposed into symmetric and antisymmetric parts

$$\mathsf{K} = \mathsf{S} + \mathsf{A}, \tag{14}$$

where $\mathsf{S} = \left(\mathsf{K} + \mathsf{K}^{\mathrm{T}}\right)/2$ and $\mathsf{A} = \left(\mathsf{K} - \mathsf{K}^{\mathrm{T}}\right)/2$. This decomposition is physically meaningful as it can be shown (see Appendix A) that the flux associated with the antisymmetric part $\mathbf{F}^c_{\mathsf{A}} \equiv -\mathsf{A}\nabla\hat{c}$ has no effect on tracer variance (see also Griffies, 1998); this flux is often referred to as reversible "stirring." This is in contrast to the flux associated with the symmetric part $\mathbf{F}^c_{\mathsf{S}} \equiv -\mathsf{S}\nabla\hat{c}$ which acts as a global sink of mean tracer variance (see Appendix A), thus behaving like irreversible "mixing." Irreversible mixing is the effect targeted by typical isopycnal mixing parameterizations. Thus the primary focus in this study will be on the symmetric part S.

The symmetry of S implies it can be orthogonally diagonalized as

$$\mathsf{S} = \mathsf{U}\mathsf{D}\mathsf{U}^{\mathrm{T}}, \tag{15}$$

where the orthonormal columns of U are the eigenvectors of S and

$$\mathsf{D} = \begin{bmatrix} \kappa_1 & 0 \\ 0 & \kappa_2 \end{bmatrix}, \tag{16}$$

where κ_1 and κ_2 are the eigenvalues of S with $\kappa_1 \geq \kappa_2$ by definition. The eigenvalues κ_1 and κ_2 represent isopycnal diffusivities along orthogonal mixing directions defined by the columns of U. In this study, we "measure" the diffusivities and directions in our simulations by diagnosing K from Equation (13), the method for which we discuss next.

2.3.3. Diagnosing the mixing tensor

To diagnose the four entries of K by inverting Equation (13) requires two equations—two tracers advected by the same flow (e.g., Plumb & Mahlman, 1987). However, the use of only two tracers can cause the diagnosed K to depend strongly on the particular tracer distributions or to become ill-conditioned (Bratseth, 1998); for instance, if one of the tracer gradients vanishes then inverting Equation (13) becomes indeterminate. This motivates the Method of Multiple Tracers as a way to minimize these effects and to diagnose a robust, tracer-independent mixing tensor.

We consider the simultaneous advection of m passive tracers $c = c_j$ for $j = 1, \ldots, m$, each with its own mean gradient $\nabla \hat{c}_j$. It is assumed that the same mixing tensor in Equation (13) applies to all tracers and thus depends only on the underlying flow, i.e., $\widehat{\mathbf{u}'' c_j''} = -\mathsf{K}\nabla \hat{c}_j$ for all j. If $\mathsf{F} \in \mathbb{R}^{2\times m}$ is a flux matrix with columns $\widehat{\mathbf{u}'' c_j''}$ and $\mathsf{G} \in \mathbb{R}^{2\times m}$ is a gradient matrix with columns $\nabla \hat{c}_j$, then the flux-gradient relationship for each tracer can be combined into a single matrix equation

$$\mathsf{F} = -\mathsf{K}\mathsf{G}. \tag{17}$$

For $m > 2$, Equation (17) is an overdetermined system of equations whose best-fit, least-squares solution is given by

$$\mathsf{K} \simeq \mathsf{K}_{\text{lsq}} = -\mathsf{F}\mathsf{G}^{\dagger} \tag{18}$$

where $(\cdot)^{\dagger}$ is the pseudoinverse. The symmetric part is computed similarly, i.e., $\mathsf{S} \simeq \mathsf{S}_{\text{lsq}} = (\mathsf{K}_{\text{lsq}} + \mathsf{K}_{\text{lsq}}^{\mathrm{T}})/2$.

In summary, by combining flux-gradient information from many tracers advected by the same flow, an optimal estimate for K (Equation (18)) can be diagnosed with low errors in the least-squares sense (see Appendix B) and the dependency of K on the particular tracer distributions is reduced (see Zhang & Wolfe, 2022).

The mean tracer gradients are maintained in statistically steady state through the addition of a slow restoring in the tracer equation (Equation (3)), so that

$$\partial_t(hc) + \nabla \cdot (h\mathbf{u}c) = \frac{1}{\tau} h\left(c^* - c\right), \tag{19}$$

where τ is a prescribed time scale and c^* is a prescribed target profile. This ensures that once the turbulent flow reaches statistically steady state, eddy fluxes will continuously feed off the mean gradients that each tracer has been reorganized into. The restoring time scales are slow with respect to typical eddy turnover times. Here we use two time scales and four target profiles; namely,

$$\tau \in \{2, 6\} \text{ years},$$
$$c^* \in \{\sin(2\pi x), \cos(2\pi x), \cos(\pi y), y\},$$

where x and y are normalized longitude and latitude coordinates; each tracer varies between −1 and 1. The combinations from these two sets results in $m = 8$ unique tracers, each with its own mean gradient, which makes Equation (17) overdetermined and available for pseudoinversion. Finally, to account for the effect that the weak restoring has on the flux-gradient relationship (Equation (13)), we here also incorporate the correction to Equation (18) described in Section 5.2 of Bachman et al. (2015).

2.4. Simulations

The simulations considered in this study are summarized in Table 1. A 1/32° reference simulation (ref) is "eddy-resolving" over most of the domain, except over the shelves along the edge of the domain (Figure 1e). All other simulations are "eddy-permitting" over most of the domain (Figure 1c, d), with horizontal grid spacings of 1/2° (p5) and 1/4° (p25). The eddy-permitting simulations use either no mesoscale parameterization (noBS), isopycnal tracer diffusion (noBS-Redi), or the backscatter parameterization outlined in Section 2.2 (BS). Except for the horizontal grid spacing, time step, and choice of mesoscale parameterization, all model parameters are the same across the simulations.

Simulation	Grid [°]	Backscatter	κ_{Redi} max, volume-mean [$\text{m}^2\ \text{s}^{-1}$]	c_{bs}	c_{exp}
p5noBS	1/2	No	0	—	—
p5BS	1/2	Yes	0	4	2.5
p5noBS-Redi	1/2	No	2400, 893	—	—
p25noBS	1/4	No	0	—	—
p25BS	1/4	Yes	0	2	1.75
p25noBS-Redi	1/4	No	2400, 516	—	—
ref	1/32	No	0	—	—

Table 1: Main simulations performed in this study. "Grid" refers to the horizontal grid spacing. "Backscatter" (BS) refers to whether the backscatter parameterization of Section 2.2 is used. If isopycnal tracer diffusion is used, its maximum value is given by "κ_{Redi} max"; this value is then scaled horizontally and vertically (see Section 2.4). If the backscatter parameterization is used, the tuning coefficients are given by c_{bs} (Equation (5)) and c_{exp} (Equation (8)).

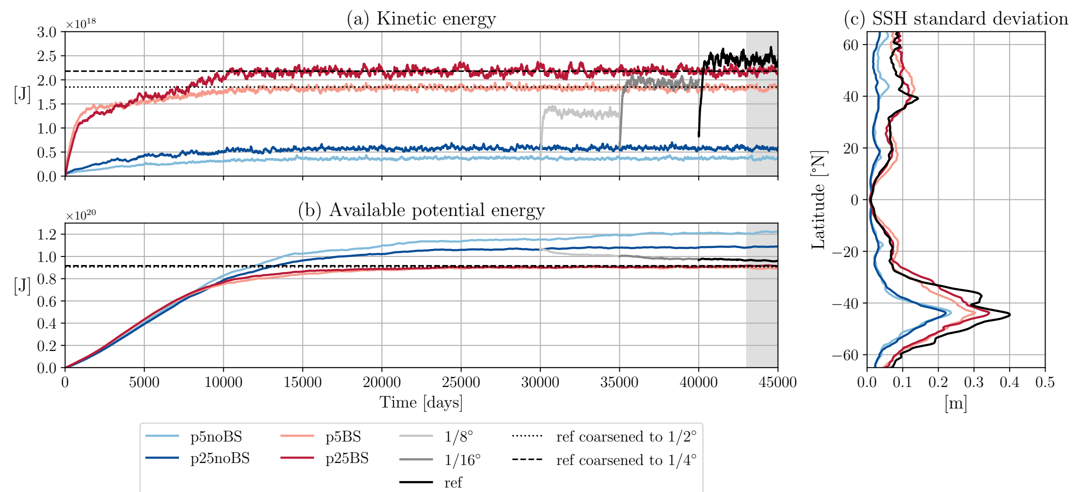

Figure 2: (a, b) Time series of globally integrated (a) kinetic energy and (b) available potential energy for the main simulations outlined in Table 1. The 1/8° and 1/16° simulations are not included in Table 1 as they are performed only as part of the spin-up of the 1/32° (ref) simulation (see text). The gray shading represents the 2,000–day window used for analysis throughout this study. (c) Zonally averaged sea surface height (SSH) standard deviation with respect to a 2,000–day climatology.

In the noBS-Redi simulations, the parameterized isopycnal tracer diffusivity has a maximum value of 2,400 $\text{m}^2\ \text{s}^{-1}$, a value based on the diagnosed diffusivities in the ref simulation (see Section 3.2). This maximum value is reduced horizontally by a step function resolution criterion (Hallberg, 2013)—set to zero where the mesoscale is deemed resolved (within the pink isoline in Figure 1) and unscaled otherwise—and vertically by a locally computed equivalent barotropic mode, a structure often used in observational and modeling studies (e.g., Adcroft et al., 2019; Groeskamp et al., 2020; Holmes et al., 2022). As tracers are passive in the NW2 configuration, isopycnal tracer diffusion does not affect the flow, and thus velocities and stratification are identical between the noBS and noBS-Redi simulations at each resolution. The noBS-Redi simulations will therefore only be considered in Sections 3.4 and 3.5 where passive tracer-only results are discussed.

Following Yankovsky et al. (2024), the backscatter simulations were tuned so that the globally integrated KE and APE simultaneously match those of the coarsened ref simulation (Figure 2a, b) via the parameterization's two main tuning parameters: c_{bs} (Equation (5)) and c_{exp} (Equation (8)); the values are given in Table 1. Other flow metrics were also checked when tuning, including the KE distribution throughout the domain as well as the stratification, especially in the reentrant channel (see Section 3.1). The values of c_{bs} differ to those in Yankovsky et al. (2024) as here we employ a different vertical structure for backscatter. However, they are consistent with these authors' analysis where the transition from 1/2° to 1/4° required a roughly halved c_{bs}

coefficient. In the regime where L_{mix} (Equation (7)) is set by the grid scale, then the vertical structure (Equation (8)) is more surface-intensified at 1/4° than at 1/2°, which is also consistent with the recommendations of Yankovsky et al. (2024). Finally, we employ the backscatter shut-off criterion described in Yankovsky et al. (2024): here, whenever the biharmonic viscosity ν_4 reaches 0.45 of its CFL limit, the viscous-source and backscatter-sink terms in the MEKE budget (Equation (6)) are turned off (until ν_4 settles back below the shut-off criterion). This mitigates a positive feedback cycle that can emerge between the biharmonic viscosity and harmonic negative viscosity (see Yankovsky et al., 2024); its use ensures numerical stability and obviates the need to substantially reduce the time step. Like the other tuning parameters, this value was chosen empirically when tuning.

The 1/2° and 1/4° simulations were spun up from rest for 45,000 days, which was sufficiently long for there to be minimal drift in globally integrated KE and APE (Figure 2a, b). More intensive diagnostics were saved over the final 2,000–day window, which will be the period used for analysis throughout the study. The spin-up procedure for the 1/32° simulation follows that described in Marques et al. (2022). First, a 1/8° simulation is branched from the 1/4° unparameterized simulation after 30,000 days by interpolating interface height and tracer fields, and setting velocities and transports to zero; the 1/8° simulation is run for 5,000 days with mechanical equilibrium quickly re-achieved. This procedure is then repeated at 1/16° and at 1/32°. The globally integrated KE and APE of the 1/32° simulation show minimal drift by the end of this procedure (Figure 2a, b).

3. Results

3.1. Evaluating the backscatter parameterization

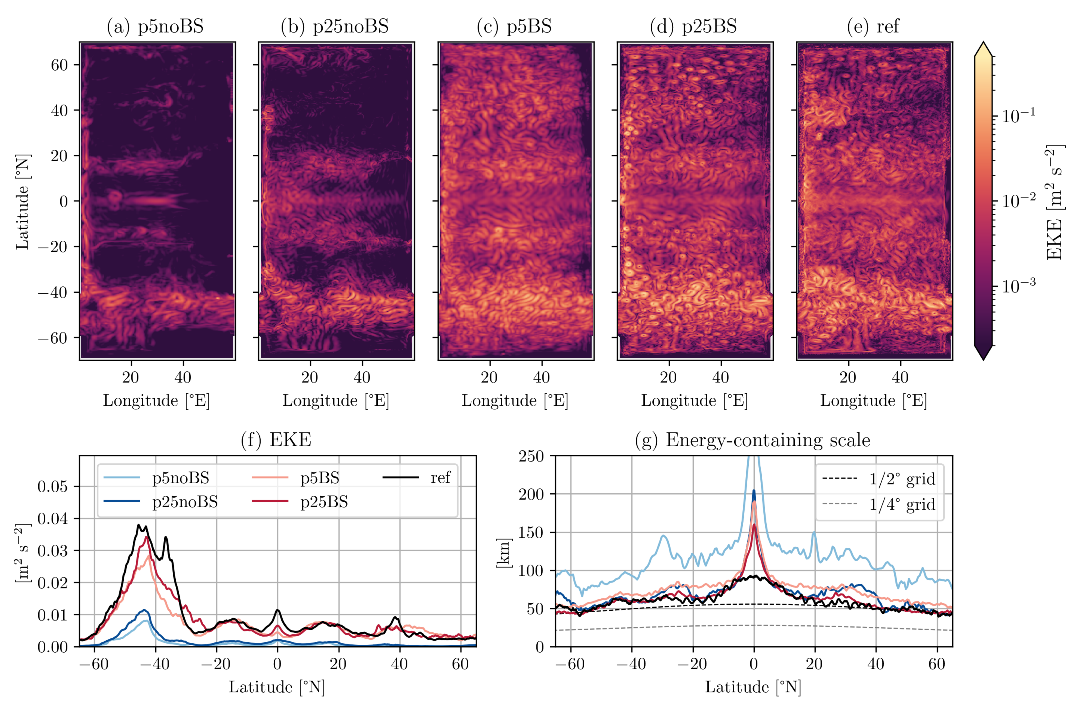

Figure 3: (a–e) Snapshots of depth-averaged EKE (on a log color scale) in the (a) p5noBS, (b) p25noBS, (c) p5BS, (d) p25BS, and (e) ref simulations (see Table 1). (f) Time-, depth-, and zonally averaged EKE in the same simulations. (g) Energy-containing scale (Equation (22)) in the same simulations; grid spacing is computed as $\sqrt{(\Delta x^2 + \Delta y^2)/2}$ following Hallberg (2013).

In this first analysis section, we briefly evaluate the effect of the backscatter parameterization on energetics and stratification, before focussing on tracer mixing in the following sections. We first examine the distribution of depth-averaged EKE. Denoting $(\cdot)'$ as a deviation from a 2,000–day time average $\overline{(\cdot)}^t$, then EKE is here defined as

$$\text{EKE} \equiv \frac{1}{2}\|\mathbf{u}'\|^2, \quad \mathbf{u}' \equiv \mathbf{u} - \overline{\mathbf{u}}^t, \tag{20}$$

and is computed from 10–day snapshots. Depth-averages are defined as

$$\overline{f}^z \equiv \frac{\sum_n h_n f_n}{\sum_n h_n} \tag{21}$$

for any field $f = f_n(x, y, t)$ (recall n is the layer index). Throughout much of the domain, depth-averaged EKE is an order of magnitude or larger in the backscatter simulations over unparameterized simulations (Figure 3); these results are similar to those in Yankovsky et al. (2024). Depth-averaged EKE in the channel ("Southern Ocean") is more commensurate across the simulation but is still between three to four times smaller in both p5noBS and p25noBS than in the p5BS, p25BS, and ref simulations (Figure 3f).

Although eddy activity is improved in the backscatter simulations, the lateral scale of eddies appears too large at 1/2° resolution (p5BS) (Figure 3c). To demonstrate this quantitively, we compute the energy-containing scale L_e from the sea surface height (SSH) deviation η'_{SSH} (e.g., Zhang & Wolfe, 2022; Yankovsky et al., 2024) via

$$L_e = \sqrt{\frac{\overline{\eta'^2_{\text{SSH}}}^t}{\overline{|\nabla \eta'_{\text{SSH}}|^2}^t}}. \tag{22}$$

When eddies are present, L_e is a good approximation to the peak of the surface kinetic energy spectrum (Zhang & Wolfe, 2022) and is thus indicative of the lateral eddy scale. However, in the limit of minimal eddy activity, L_e can become very large where spatial gradients become small, as occurs here for the p5noBS simulation. Figure 3g demonstrates that the eddy scale is larger in p5BS than in ref, especially in mid- and high northern latitudes. Overly large eddies also manifest as an overly large SSH standard deviation (Figure 2c). We hypothesize that the eddy scale is too large at 1/2° resolution since smaller eddies are too close to the grid scale (Figure 3g) and are dissipated by the biharmonic viscosity. This issue is mitigated at 1/4° resolution (p25BS), where the eddy scale is more in line with the ref simulation.

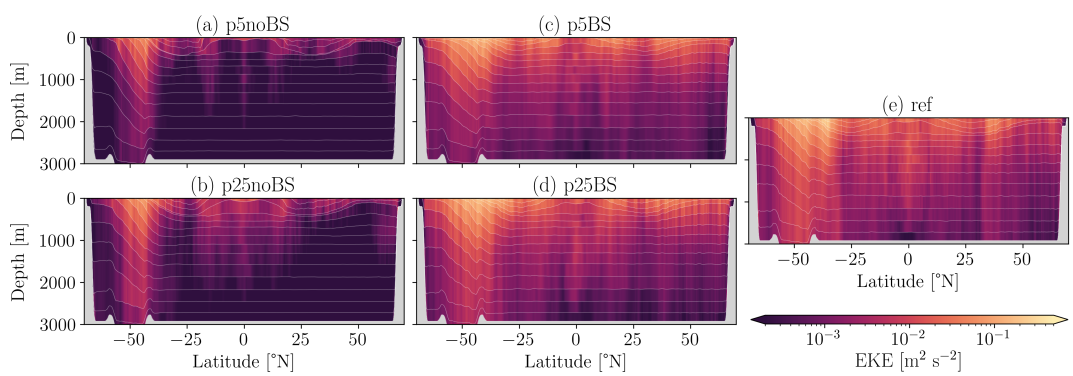

Figure 4: Snapshots of zonally averaged EKE (on a log color scale) in the (a) p5noBS, (b) p25noBS, (c) p5BS, (d) p25BS, and (e) ref simulations (see Table 1). Thin white lines show zonally averaged isopycnal interfaces; gray shading shows bathymetry.

We next consider the zonally averaged vertical structure of EKE. The EKE is too weak at depth in the unparameterized simulations (Figure 4a, b); the exception is in the Southern Ocean zonal jet where EKE, although still too weak, penetrates to depth more accurately, consistent with the findings of Yankovsky et al. (2022). In the p5BS simulation, EKE is too weak in the Southern Ocean at depths below roughly 1,500 m compared to the ref simulation (Figure 4c, e). However, throughout the rest of the domain, the vertical structure of EKE is largely in line across the p5BS, p25BS, and ref simulations. This suggests that backscatter is helping to liberate energy being trapped in higher baroclinic modes, which occurs when the baroclinic energy cycle is

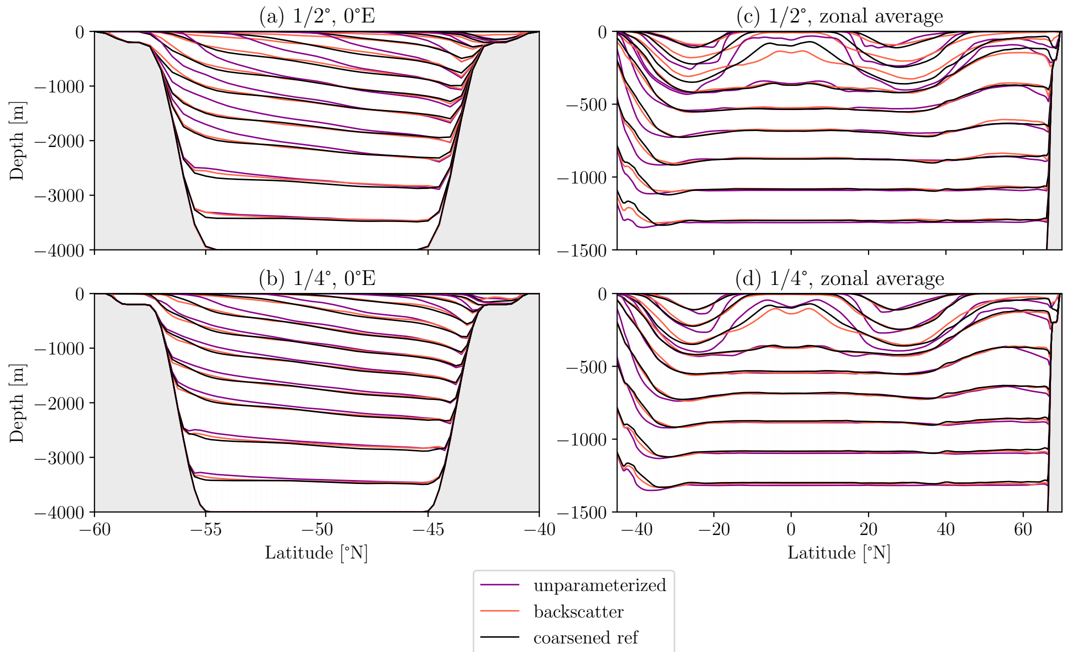

Figure 5: Time-averaged isopycnal interfaces in unparameterized (purple), backscatter (pink) and ref (black) simulations; gray shading shows bathymetry. (a–b) Meridional section over the reentrant channel at 0°E in (a) 1/2° simulations (p5noBS and p5BS) and (b) 1/4° simulations (p25noBS and p25BS). (c–d) Zonal average shown between 45°S and 70°N in (c) 1/2° simulations (p5noBS and p5BS) and (d) 1/4° simulations (p25noBS and p25BS). The ref simulation has been coarsened from 1/32° to either 1/2° (a, c) or 1/4° (b, d).

poorly resolved (Kjellsson & Zanna, 2017; Yankovsky et al., 2022), thereby allowing more barotropic eddies to form.

Finally, we evaluate the mean stratification in the simulations. Isopycnals are generally overly steep in the unparameterized simulations (Figure 5) due to the poorly resolved energy cycle of baroclinic eddies, which extract mean APE and convert it to EKE. A lack of mean APE extraction results in excessively steep isopycnals. Isopycnals in the backscatter simulations are closer to the ref simulation due to higher EKE and thus more efficient mean APE extraction (Figure 5). However, at 1/2° resolution (p5BS) the isopycnals are in some cases overly flat with respect to the ref simulation, largely in the upper ocean (Figure 5c). This is consistent with the eddies in this simulation being too large (Figure 3g), with larger baroclinic eddies being more efficient at extracting mean APE (Larichev & Held, 1995). The locations of the isopycnal outcrops in the Southern Ocean are inaccurate in the unparameterized simulations, whereas the outcrop locations in the backscatter simulations are closer to the ref simulation, which has consequences for Southern Ocean ventilation (see Section 3.5).

In summary, the backscatter parameterization leads to both elevated eddy activity, manifesting as larger EKE and larger SSH variability, as well as improved mean stratification over simulations without a backscatter parameterization, which have subdued eddy activity and overly steep isopycnals. Following the interpretation of Yankovsky et al. (2024), this joint effect of backscatter to both energize eddies and, thereby, lead to accurate large-scale stratification suggests that no additional GM-like thickness diffusion parameterization is necessary in these simulations. In the following sections, we seek to determine whether this backscatter parameterization also has a positive effect on along-isopycnal tracer mixing, suggesting that no additional Redi-like isopycnal diffusion parameterization is needed.

3.2. Diagnosed isopycnal diffusivities

In this section, we assess the results of the Method of Multiple Tracer (MMT) inversion outlined in Section 2.3.3, which diagnoses two isopycnal diffusivities and associated mixing directions. The averaging operator $\overline{(\cdot)}$ in the MMT inversion (Equations (9) and (10)) is a combination of online time averaging over a 2,000–day window and offline spatial coarsening onto a 2° × 2° grid. The diffusivities and mixing directions are thus defined on this 2° × 2° grid. Eddy products are computed by assuming the averaging operator obeys standard Reynolds assumptions, i.e., $\widehat{\mathbf{u}''c''} = \widehat{\mathbf{u}c} - \hat{\mathbf{u}}\hat{c}$ (see Section 2.3.1). Note that the simulations with isopycnal tracer diffusion (p5noBS-Redi and p25noBS-Redi) are not discussed here.

3.2.1. Spatial distribution of diffusivities

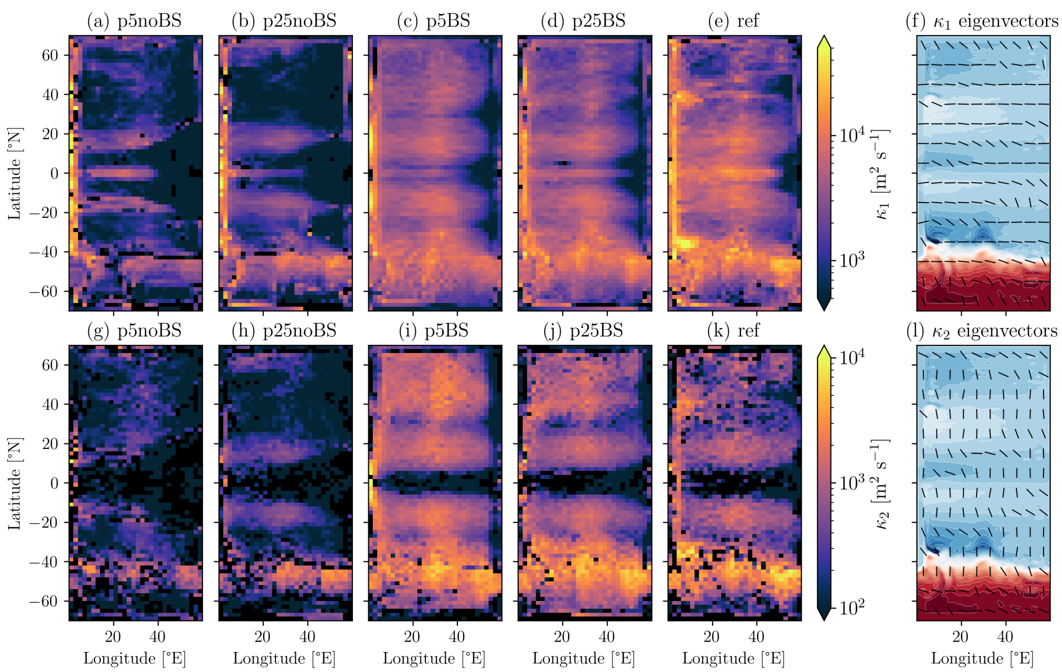

Figure 6: Depth-averaged isopycnal diffusivities and eigenvectors (mixing directions) from the Method of Multiple Tracers inversion (see Section 2.3.3). (a–e) κ_1 (on a log color scale) in the (a) p5noBS, (b) p25noBS, (c) p5BS, (d) p25BS, and (e) ref simulations. (f) Eigenvectors associated with κ_1 in the ref simulation (the other simulations are similar), and the time-mean barotropic stream function is shown in contours. (g–l) As in (a–f) but for κ_2. Negative values of κ_1 and κ_2 are plotted in black. Note that the colorbar limits differ for κ_1 and κ_2. The eigenvectors in (f, l) are shown on a coarser grid than the diffusivities for ease of viewing.

Figure 6 shows the depth-averaged isopycnal diffusivities κ_1 and κ_2 (Equation (15)) as well as their mixing directions (eigenvectors). The larger diffusivity κ_1 generally has its mixing direction aligned with the mean flow, while κ_2 is generally directed across it (Figure 6f, l). That κ_1 tends to represent an along-mean flow diffusivity suggests that its larger values may be the result of mean flow-induced shear dispersion (Taylor, 1953; Smith, 2005). Similarly, that κ_2 represents an across-mean flow diffusivity suggests that it may be affected by mean flow suppression (Ferrari & Nikurashin, 2010; Groeskamp et al., 2020). These hypotheses are tested in Section 3.2.2.

Similar to EKE (see Section 3.1), depth-averaged isopycnal diffusivities are subdued in the p5noBS and p25noBS simulations over much of the domain compared to the p5BS, p25BS, and ref simulations, and are smaller in many regions by an order of magnitude or more (Figure 6). In the backscatter and ref simulations, depth-averaged diffusivities are generally $\mathcal{O}$(100–1,000) m^2 s^{-1} and tend to be larger on or downstream of the meridional ridge. Diffusivities are elevated in the energetic western boundary current regions at ±40°N in the ref simulation as well as in a mixing hotspot in the channel downstream of the ridge at roughly 50°E; this is less pronounced in the backscatter simulations, which showed weaker EKE in these regions (Figure 3). In contrast, diffusivities are larger in the p5BS simulation than in the ref simulation at northern mid- and high latitudes. This may stem from the overly large eddies in this region (Figure 3g): from a mixing length argument, eddies with larger lateral scales but commensurate energy levels will generate larger diffusivities.

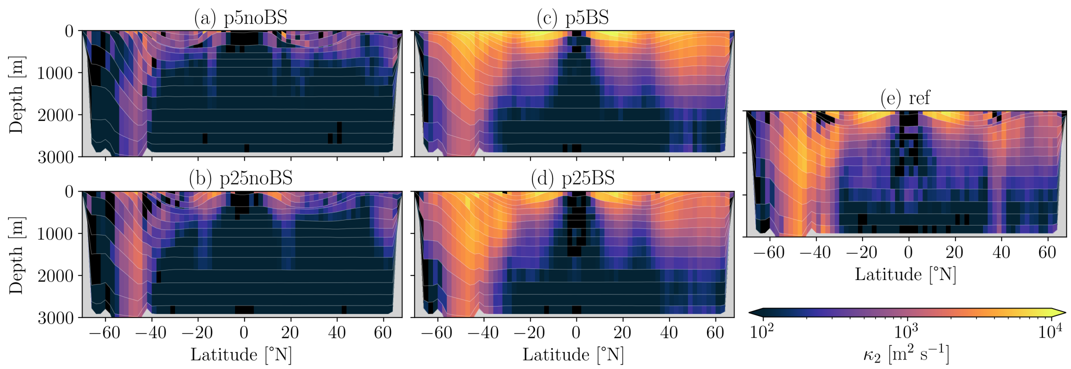

Figure 7: Zonally averaged isopycnal diffusivity κ_2 (on a log color scale) in the (a) p5noBS, (b) p25noBS, (c) p5BS, (d) p25BS, and (e) ref simulations. Thin white lines show zonally and time-averaged isopycnal interfaces (coarsened to the same horizontal grid as the diffusivities); gray shading shows bathymetry. Negative values are plotted in black.

We next examine the zonally averaged vertical structure of the diffusivities, focussing on the mostly meridionally directed κ_2 diffusivity (Figure 7). In the unparameterized simulations, the vertical damping of mixing largely follows the vertical damping of EKE (cf. Figures 4 and 7). In the backscatter simulations, the vertical structure of mixing is remarkably similar to the ref simulation in the subtropics. However, in the ref simulation there are subsurface maxima in the Southern Ocean zonal jet and in the western boundary current region (roughly 40°N), whereas the diffusivity appears more surface-intensified in the backscatter simulations, particularly in p5BS.

Figure 8 shows the vertical structures of κ_1 and κ_2 averaged over three regions highlighted in Figure 1b: in the southeastern subtropics, in the northeastern subpolar region, and in the Southern Ocean. In all regions, the magnitude of κ_1 is generally too low in p5BS and p25BS compared to ref, especially in the Southern Ocean region (Figure 8a, b, c). Agreement in magnitude is generally stronger in κ_2, with excellent similarity in the subtropical region in both magnitude and e-folding depth (Figure 8d). However, as noted in the previous paragraph, there are differences in the vertical structures of κ_2, particularly between the p5BS and ref simulations in the subpolar and Southern Ocean regions shown in Figure 8. We next test possible hypotheses to explain (i) the enhancement of κ_1 and (ii) the surface suppression of κ_2 in the ref simulation; our main goal is to explain the differences between the backscatter and ref simulations.

3.2.2. Shear dispersion enhancement and mean flow suppression

Mixing length theory proposes that an eddy diffusivity $\mathcal{K}$ be written as

$$\mathcal{K} \equiv \Gamma u_{\mathrm{rms}} \ell, \tag{23}$$

where Γ is the mixing efficiency, u_{rms} is the root-mean-square (rms) eddy velocity, and ℓ is an eddy mixing length. Here, we assume that $\Gamma = 0.35$ (e.g., Klocker & Abernathey, 2014; Groeskamp et al., 2020), that the eddy velocity is given by the time-averaged and vertically-dependent EKE (Equation (20)), i.e.,

$$u_{\mathrm{rms}}(x, y, z) = \sqrt{2\,\overline{\mathrm{EKE}}^{t}}, \tag{24}$$

that the eddy mixing length is given by the vertically-independent energy-containing scale (Equation (22)), i.e., $\ell = L_{\mathrm{e}}$, and that $\mathcal{K}$ represents a background eddy diffusivity.

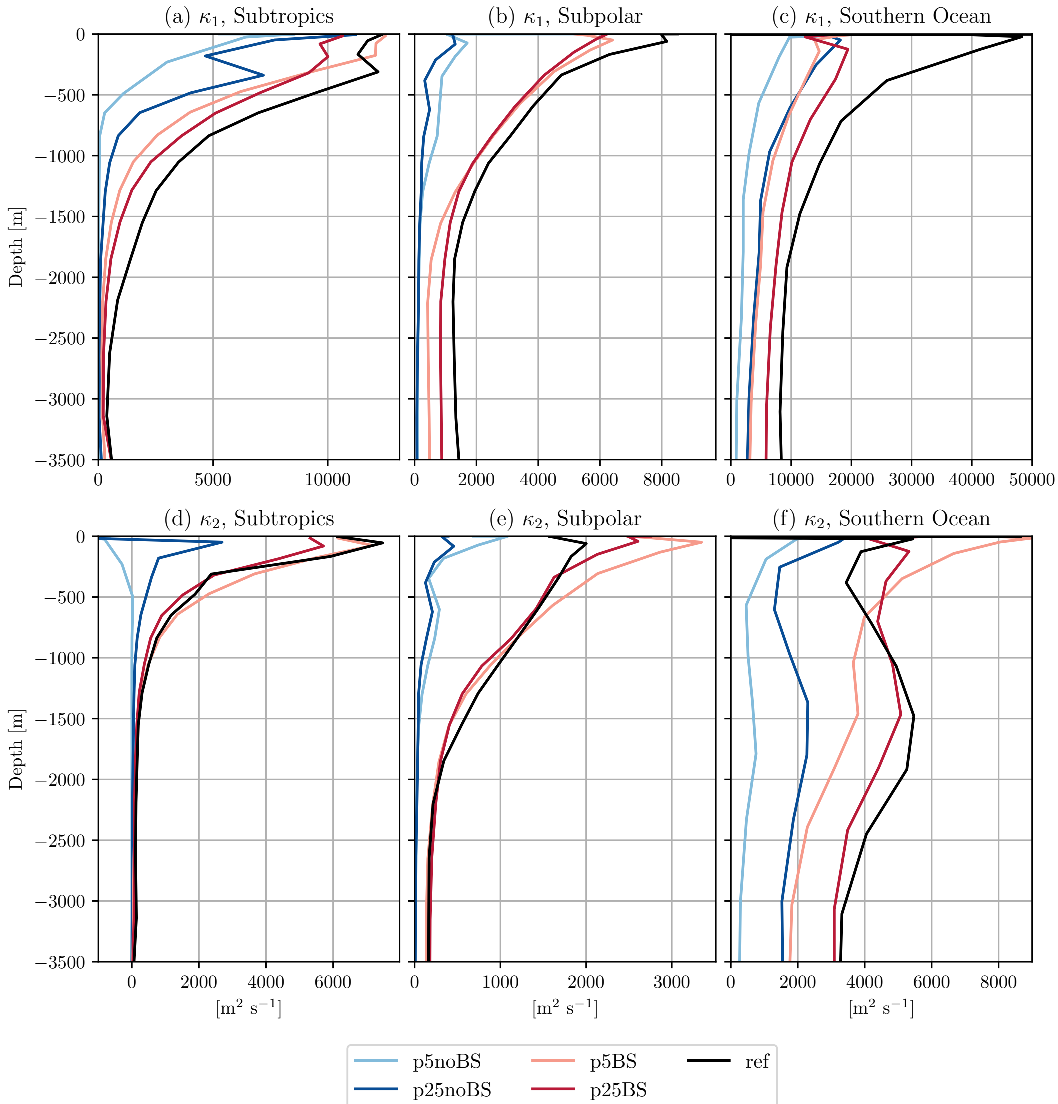

Figure 8: Vertical structure of (a–c) κ_1 and (d–f) κ_2. Regions shown (see boxes in Figure 1b) are (a, d) subtropics, averaged over (46°E to 52°E, −22°N to −16°N); (b, e) subpolar, averaged over (46°E to 52°E, 52°N to 58°N); and (c, f) Southern Ocean averaged over (46°E to 52°E, −54°N to −48°N). Averages over the regions are thickness-weighted averages (Equation (9)) using the time-mean thickness $\overline{h}$ (which is necessary where layer thicknesses vary over the spatial region); negative diffusivities are included in the average.

We first assess why κ_1 tends to be larger in the ref simulation than in the backscatter simulations. Shear dispersion (Taylor, 1953) suggests that a diffusivity in the along-mean flow direction $\mathcal{K}_\parallel$ should be enhanced over a background diffusivity, with the prediction (up to a scaling constant)

$$\mathcal{K}_\parallel \equiv \frac{\mathcal{U}^2 \ell_{\mathcal{U}}^2}{\mathcal{K}}, \tag{25}$$

where $\mathcal{U}$ is a scale for the mean flow magnitude and $\ell_{\mathcal{U}}$ is a length scale for the mean flow shear. Smith (2005) showed this prediction to hold reasonably accurately in jet-dominated two-dimensional turbulence. We therefore compute Equation (25) with depth-averaged fields by defining a mean flow scale and a shear length scale as

$$\mathcal{U}^2 \equiv \left\langle \left(\overline{u}^{z,t}\right)^2 + \left(\overline{v}^{z,t}\right)^2 \right\rangle, \quad \ell_{\mathcal{U}}^2 \equiv \frac{\mathcal{U}^2}{\left\langle \left(\partial_y \overline{u}^{z,t}\right)^2 + \left(\partial_x \overline{v}^{z,t}\right)^2 \right\rangle}, \tag{26}$$

where $\overline{(\cdot)}^{z,t}$ is a depth- and time-average and $\langle \cdot \rangle$ is a spatial coarsening onto a 2° × 2° grid. We also use the depth-averaged mixing length diffusivity $\langle \overline{\mathcal{K}}^z \rangle$ in Equation (25). Figure 9 shows the result plotted against $\overline{\kappa_1}^z$ averaged over the three regions in Figure 8. The prediction is imperfect, especially in the subtropics region, which is possibly related to the neglect of vertical variations in the flow. However, the results suggest, at least in the subpolar and Southern Ocean regions, that enhanced dispersion along strong barotropic shear flows may contribute to the increases in κ_1 across the resolutions.

We next assess whether mean flow suppression theory can explain the differences in the vertical structure of κ_2, in particular, between p5BS and ref, which showed larger discrepancies (Figure 8e, f). Such theory (Ferrari & Nikurashin, 2010; Klocker et al., 2012) proposes that the diffusivity in the across-mean flow direction $\mathcal{K}_\perp$ be suppressed over a background diffusivity in the presence of mean flows. We write the result of Ferrari and Nikurashin (2010) in the general form

$$\mathcal{K}_\perp \equiv S_\perp \mathcal{K}, \tag{27}$$

where

$$S_\perp \equiv \frac{1}{1 + \gamma^{-2} k_\mathrm{e}^2 \left(c_{w,\parallel} - U_\parallel\right)^2} \tag{28}$$

is the suppression factor in the cross-stream direction. Here, γ is an eddy decorrelation rate, which we assume to be depth-independent and is found by a least squares approach similar to previous studies (e.g., Klocker et al., 2012; Groeskamp et al., 2020; Zhang & Wolfe, 2022); k_e is an eddy wavenumber, here computed as $k_\mathrm{e} = 1/\ell_\mathrm{e}$, where ℓ_e is the energy-containing scale (Equation (22)); and $c_{w,\parallel}$ and $U_\parallel$ are, respectively, the eddy phase speed and time-averaged flow projected onto the eigenvector associated with κ_1 (recall that this is orthogonal to the direction associated with κ_2). The eddy phase velocity is calculated using the long planetary Rossby wave dispersion relation, Doppler-shifted by the depth- and time-averaged flow as suggested by Klocker and Marshall (2014), so that

$$\mathbf{c}_w = \overline{\mathbf{u}}^{z,t} - \beta L_\mathrm{d}^2 \mathbf{i}. \tag{29}$$

We then project the time-averaged flow $\overline{\mathbf{u}}^t$ and $\mathbf{c}_w$ onto the eigenvector associated with κ_1 to calculate $U_\parallel$ and $c_{w,\parallel}$, respectively. From this construction, the only depth-varying component of Equation (28) comes from $U_\parallel$. As noted above, γ is found via a least squares approach by minimizing the vertical integral of the squared difference between profiles of κ_2 and $\mathcal{K}_\perp$. This is done for each profile in each region shown in Figure 8 (results were similar if γ was instead found by fitting the averaged profile in each region). We show only the results for the subpolar and Southern Ocean regions in Figure 9 as Equation (27) was not a good model for κ_2 in the subtropics region (not shown).

The suppressed diffusivity $\mathcal{K}_\perp$ generally captures the vertical structure of κ_2 in both the subpolar and Southern Ocean regions in the upper 1,000 m (Figure 9), though performs less well at depths below this (see Zhang & Wolfe, 2022). In the subpolar region, the mixing length diffusivity $\mathcal{K}$ is similar to both $\mathcal{K}_\perp$ and κ_2. This demonstrates that, in this region, the differences in κ_2 between the backscatter and ref simulations arise largely from differences in the eddy scale and EKE. In contrast, in the Southern Ocean region, $\mathcal{K}_\perp$ is systematically smaller than κ_2 at the surface, and is increasingly so as resolution increases. In this region, the mean flow $U_\parallel$ at the surface is in fact slightly stronger in p5BS than in ref (not shown), so differences between these simulations arise from the $\gamma^{-2} k_\mathrm{e}^2$ prefactor (Equation (28)). The eddy decorrelation time scale from the fitting procedure is found to be $\gamma^{-1} = 3.6, 4.7$, and 5.5 days, and the energy-containing scale is $k_\mathrm{e}^{-1} = 60, 55$, and 58 km in the p5BS, p25BS, and ref simulations, respectively. The $\gamma^{-2} k_\mathrm{e}^2$ prefactor is thus indeed smaller in p5BS than in ref. Ferrari and Nikurashin (2010) suggest that γ^{-1} is proportional to the eddy strain rate $\left(k_\mathrm{e}^2 \mathrm{EKE}\right)^{-1/2}$. However, computing γ^{-1} as such using the energy-containing scale (Equation (22)) and EKE here implies the opposite tendency, i.e., γ^{-1} decreases as resolution increases (not shown), largely since the

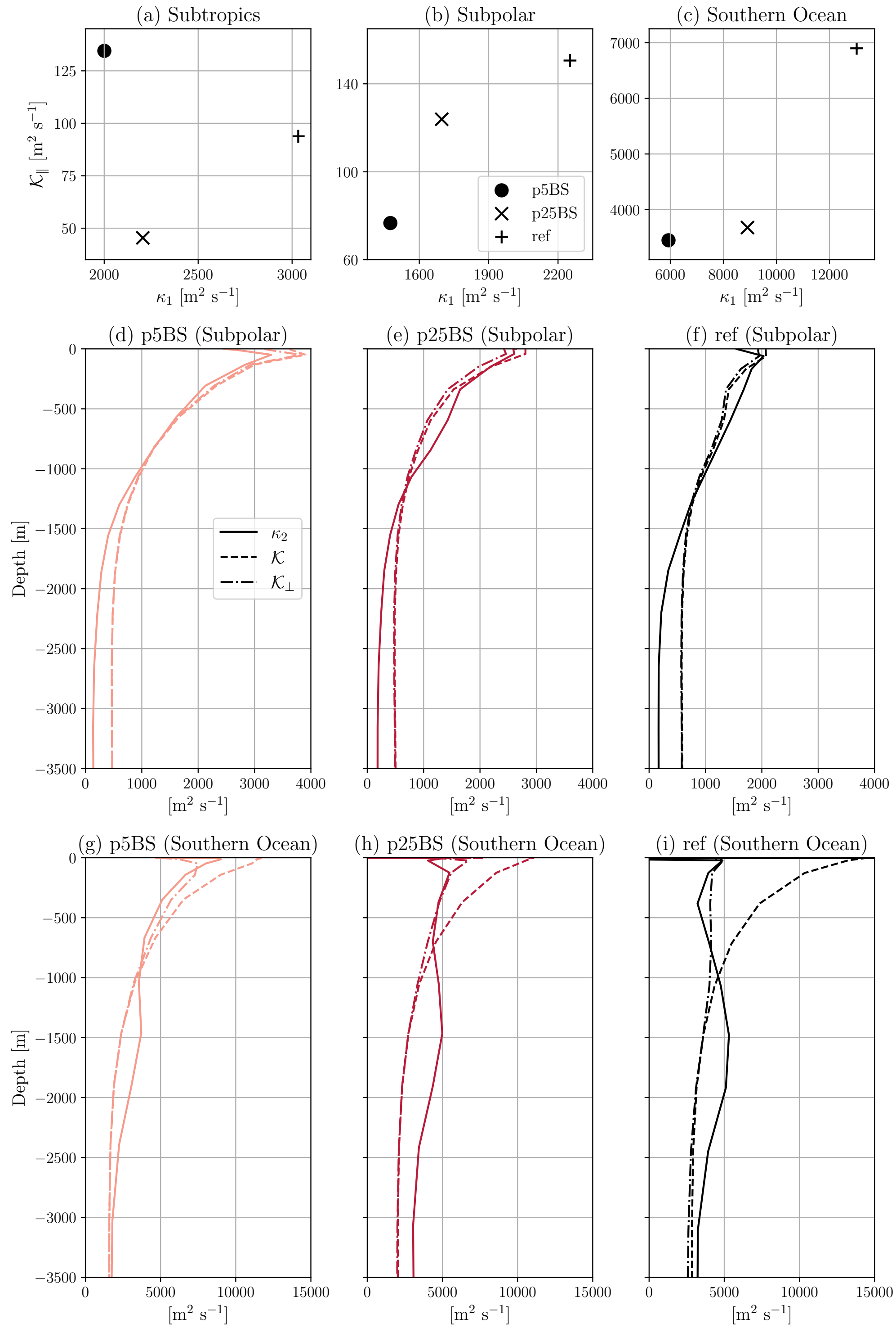

Figure 9: (a–c) Depth-averaged shear dispersion diffusivity (Equation (25)) against depth-averaged κ_1, averaged over the same three regions as in Figure 8. (d–f) Vertical structure of κ_2 (solid), mixing length diffusivity $\mathcal{K}$ (Equation (23); dashed) and suppressed mixing length diffusivity $\mathcal{K}_\perp$ (Equation (27); dashdot) in the subpolar region in the (d) p5BS, (e) p25BS, and (f) ref simulations (cf. Figure 8b, e). (g–i) As in (d–f) except in the Southern Ocean region (cf. Figure 8c, f).

eddies become more energetic as resolution increases (Figure 6f). This discrepancy between the time scale estimated from fitting and the time scale estimated from the eddy strain rate may come from the assumption that mixing is dominated by the energy-containing scale, as the true mixing length may be different (Thompson & Young, 2006; Klocker et al., 2012). Mixing is also likely driven by an increasingly multichromatic eddy field as resolution (and thus the number of scales that contribute to mixing) increases, which may modify estimates based on a single scale (Chen et al., 2014). A detailed examination of these effects and the dependencies on elements of the parameterization is left for future work, as it is beyond the scope of the present study. However, we take it to be an interesting empirical result that the mixing suppression function from Ferrari and Nikurashin (2010) is able to explain the smaller degree of surface suppression in p5BS relative to ref, possibly due to larger eddies that decorrelate more quickly.

3.2.3. Statistical distribution of diffusivities

An additional question to address is how backscatter modifies the statistical distribution of the isopycnal diffusivities throughout the domain. Backscatter leads to improvements over unparameterized simulations, shifting the distributions of κ_1 and κ_2 towards larger values and more closely matching the ref simulation (Figure 10). Neither the p5BS nor p25BS simulation matches the extremes in the tail of the κ_1 distribution in the ref simulation, which is possibly related to horizontal shear flows that are weaker or unresolved at coarser resolutions as suggested by the analysis in the previous section (Figure 9). The κ_2 distributions show much closer agreement between the p5BS, p25BS, and ref simulations (Figure 10b), which is reflected in their near-equal globally averaged values (Figure 10d). Although κ_1 is smaller in the backscatter simulations, typical isopycnal diffusion parameterizations act isotropically within the isopycnal plane. These near-equal global values of κ_2 thus suggest that no supplemental isopycnal diffusion is desirable in the backscatter simulations, at least in the global average.

3.3. Sensitivity to backscatter strength

In this section, we determine the sensitivity of isopycnal mixing to the strength of the parameterized backscatter. Here, we deviate from the main simulations summarized in Table 1 and assess a set of simulations that vary the magnitude of c_{bs} (Equation (5)), which modulates the amplitude of the negative viscosity. We show only simulations at 1/4° resolution; results were similar at 1/2° resolution (not shown). The particular emphasis is on how the isopycnal diffusivities vary as a function of eddy energy and length scales as c_{bs} is varied.

The results of the 1/4° simulations are summarized in Figure 11. Globally integrated KE increases as c_{bs} increases (Figure 11a), although the changes in KE become smaller for larger values of c_{bs}. Globally integrated APE decreases as c_{bs} increases (Figure 11a) since a more active eddy field extracts APE more effectively from the mean flow, thereby flattening isopycnals (Figure 5). The magnitudes of the isopycnal diffusivities generally increase as c_{bs} increases (Figure 11d), and these increases follow a similar pattern to increases in the EKE (Figure 11c). Notably, the energy-containing scale (Equation (22)) does not vary in a systematic fashion as c_{bs} varies (not shown), which is implied by the isopycnal diffusivities increasing at roughly the same rate as eddy velocities. If the energy-containing scale of the eddies increased as c_{bs} increased, then diffusivities would likely increase at a faster rate than eddy velocities from mixing length arguments (see Equation (23)). That the energy-containing scale does not change dramatically suggests it is more constrained by large-scale processes such as bottom drag and stratification, which are not modified as strongly by changes in c_{bs} compared to the strong changes in EKE. We note that we have not investigated the effects of changes in the vertical structure via c_{exp} (Equation (8)), which influences the resultant stratification (Yankovsky et al., 2024). Nevertheless, our results indicate that, at least with the present backscatter scheme, the strength of isopycnal mixing is strongly controlled by the strength of eddy energy as modulated by the magnitude of the backscatter.

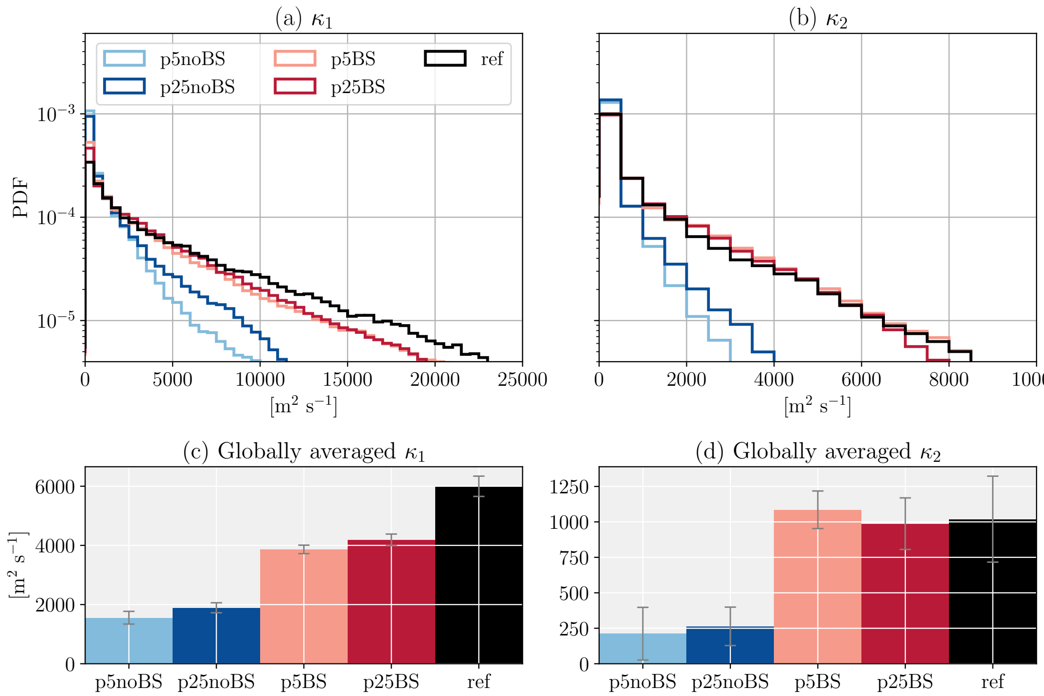

Figure 10: (a–b) Histograms (plotted as probability densities) of (a) κ_1 and (b) κ_2 for the p5noBS, p25noBS, p5BS, p25BS, and ref simulations; histograms are computed by linearly interpolating the diffusivities onto a uniform vertical grid with 25 m spacing and then binning into 500 m^2 s^{-1} bins, with only positive values shown. (c–d) Globally averaged values of (c) κ_1 and (d) κ_2 for the same simulations; averages are taken over positive values only. Error bars in (c, d) denote $\pm\sigma$, where σ is the estimated standard deviation from the least squares inversion (see Appendix B.)

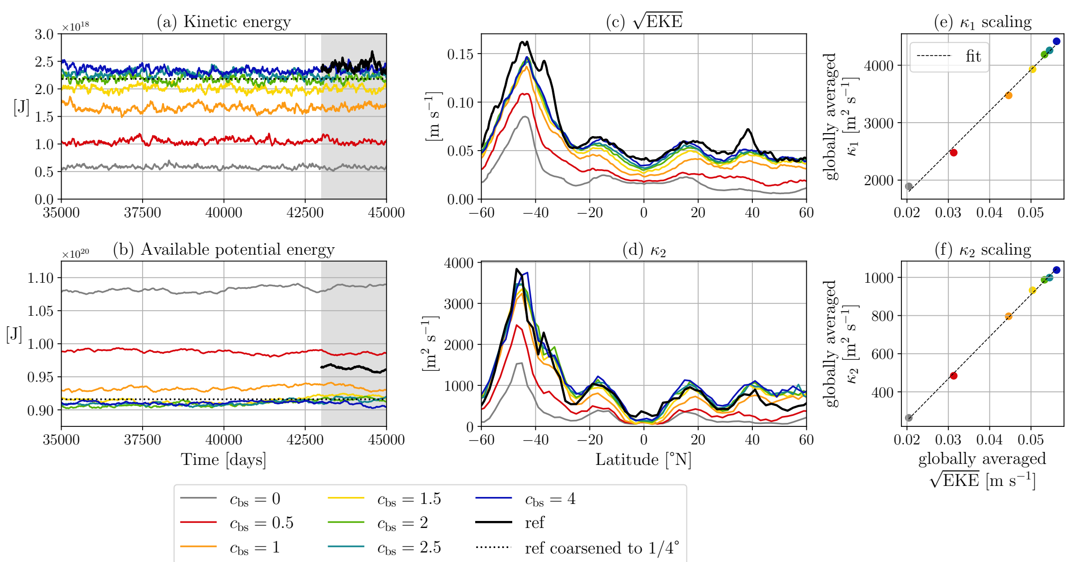

Figure 11: Summary of simulations varying c_{bs}. (a, b) Time series of globally integrated (a) kinetic energy and (b) available potential energy; the gray shading is the 2,000–day window used for analysis through this study. (c, d) Zonally and depth-averaged (c) time-averaged eddy velocity scale $\sqrt{\mathrm{EKE}}$ and (d) κ_2. (e, f) Globally averaged (e) κ_1 and (f) κ_2 against the globally and time-averaged eddy velocity scale.

3.4. Tracer biases

In this section, we return to the main simulations (Table 1) and examine how improved isopycnal mixing from backscatter impacts tracer biases relative to the ref simulation. We here also seek to compare the effect of backscatter-driven isopycnal mixing to the effect of parameterized isopycnal diffusion. The isopycnal diffusion simulations (Redi) are described in Section 2.4 and summarized in Table 1.

Figure 12 shows depth-averaged snapshots of one of the tracers used in the MMT inversion. The unparameterized simulations (Figure 12a, d) show stronger gradients in the tracer where restoring gradients are largest (at 15°E and 45°E in Figure 12) compared to the ref simulation. This is a consequence of the subdued eddy activity which, if present, would act to mix away these gradients. Adding isopycnal diffusion improves mean biases by diffusing overly large gradients (Figure 12b, e, h) [note that the impact of the abrupt resolution function is seen in Figure 12, but a smooth transition is not necessarily more suitable (Hallberg, 2013)]. However, with isopycnal diffusion these mean bias reductions are at the expense of variance biases, as diffusion also washes away the tracer signature of the partially resolved eddy variability (Figure 12h). The backscatter simulations, by enhancing the eddy activity that stirs tracers, show reductions in both mean and variance biases with respect to the ref simulation (Figure 12c, f, h). That backscatter improves both mean and variance biases suggests that it is a preferable parameterization for tracer mixing in an eddy-permitting regime. The mean bias reductions from isopycnal diffusion might be improved through tuning of the tracer diffusion coefficient, a different choice of resolution function or a different prescribed vertical structure. However, the worsening of variance biases is likely a general result whenever some eddy variability is resolved and isopycnal diffusion applied to total resolved fields is added. It is possible that a splitting procedure, such as that proposed by Mak et al. (2023) for the GM parameterization, could be applied to a Redi parameterization and lead to better results in this sense. However, how to implement such a procedure (see Mak et al., 2023) and comparisons to the approach we take here is beyond the scope of our study and is left for future work.

3.5. Ventilation tracer

In this final analysis section, we assess the impact of the backscatter parameterization on ocean ventilation. Eddy-driven isopycnal mixing plays an important role in ventilating the interior ocean, especially in the Southern Ocean where isopycnals outcrop at the surface, providing an adiabatic pathway from the ocean surface into the interior (Morrison et al., 2022). We have shown there to be differences in how our simulations represent both outcrop locations and the strength of isopycnal mixing in the Southern Ocean region of the model (Sections 3.1 and 3.2). To investigate the effect of these differences, we performed an idealized ventilation tracer experiment with a similar configuration to previous studies (e.g., England, 1995; Abernathey & Ferreira, 2015; Balwada et al., 2018).

The ventilation tracer is initialized first everywhere to 0. At every time step, it is then set to a value of 1 if the center of an isopycnal layer in a grid cell lies above a prescribed constant depth of 100 m. Otherwise, it is passively stirred into the interior. This experiment was performed over the 2,000–day window once the flow in each simulation had already reached statistically steady state (Figure 2), and output is saved as 5–day averages.

The results of this experiment are summarized in Figure 13. It is readily seen that in all simulations the ventilation tracer is taken up at the surface and mixed into the interior by eddy stirring alone (there is no diapycnal mixing in the model), which is indicated by values of tracer spanning the range between 0 and 1. The uppermost layers, which are mostly shallower than the 100 m depth value, are almost saturated with tracer after 2,000 days, while eddy stirring ventilates deeper layers more slowly. The highlighted isopycnal layer (Figure 13a–g) is the first layer to outcrop only in the Southern Ocean (i.e., it does not also outcrop in the northern part of the domain) and examining the tracer on this layer provides a clear picture of Southern Ocean ventilation in these simulations (Figure 13h, i).

Tracer concentration grows more slowly in the p5noBS and p25noBS simulations, which is a result of the subdued eddy activity that stirs the tracer into the interior (Figure 13h). This is mostly a result of subdued eddy stirring rather than incorrect outcropping, as confirmed by the simulations with added isopycnal tracer diffusion, which have the identical underlying flow and stratification to the corresponding unparameterized

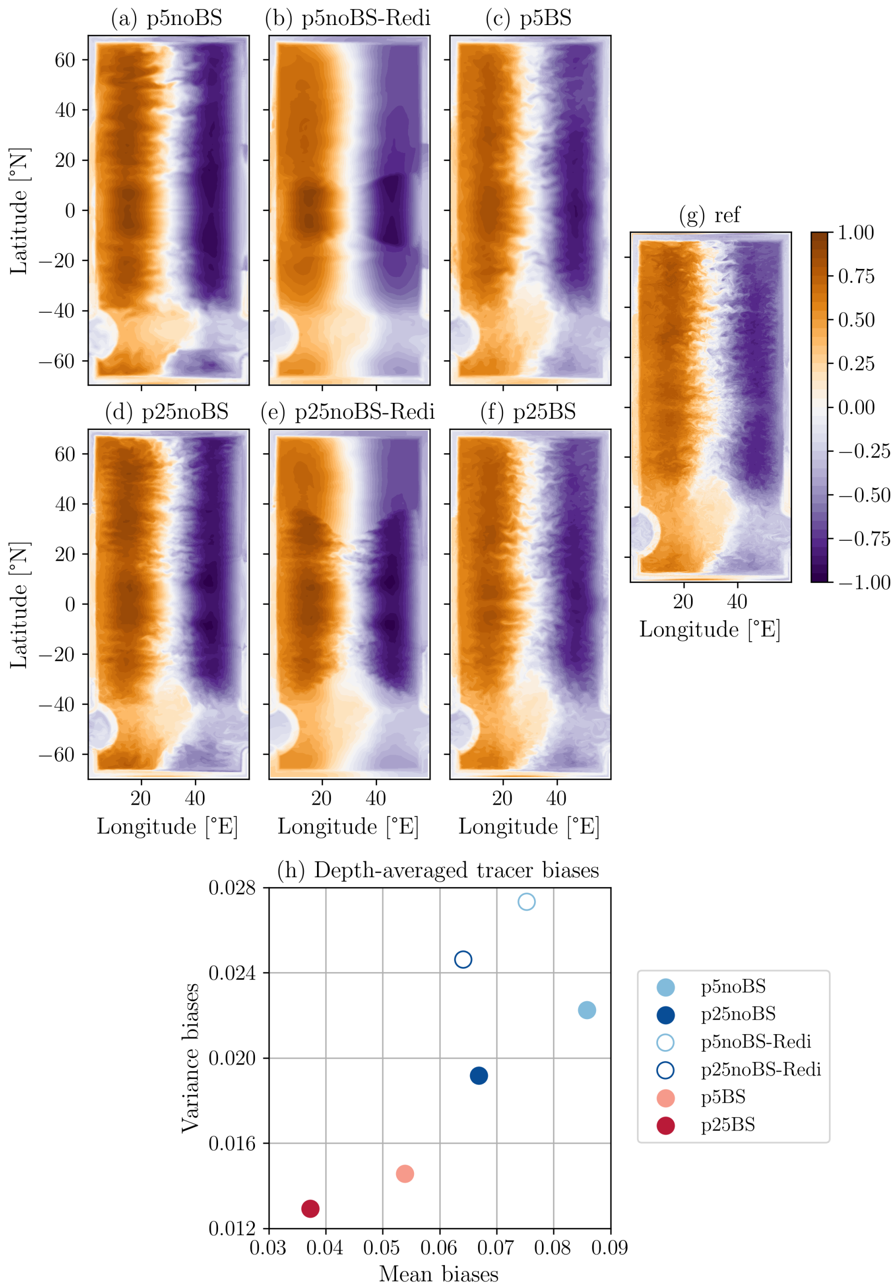

Figure 12: (a–g) Snapshots of depth-averaged tracer restored to target profile $c^* = \cos(2\pi x)$ with restoring time scale $\tau = 6$ years (see Section 2.3.3) in the (a) p5noBS, (b) p5noBS-Redi, (c), p5BS, (d) p25noBS, (e), p25noBS-Redi, (f) p25BS, and (g) ref simulations. (h) Depth-averaged biases averaged over all tracers in the MMT inversion (see Section 2.3.3). For each tracer for each simulation: mean biases are computed by depth-averaging, then time-averaging, and then taking the root-mean-square of the difference between the given simulation and the ref simulation coarsened to either 1/2° or 1/4°; variance biases are computed by depth-averaging, then taking the temporal standard deviation, and then taking the root-mean-square of the difference between the given simulation and the ref simulation coarsened to either 1/2° or 1/4°. An average is then taken over all tracers in each simulation to obtain the values in (h).

simulation: p5noBS-Redi and p25noBS-Redi show growth in tracer concentration on this layer more in line with the ref simulation. However, this victory is pyrrhic as these simulations exhibit too high tracer con-

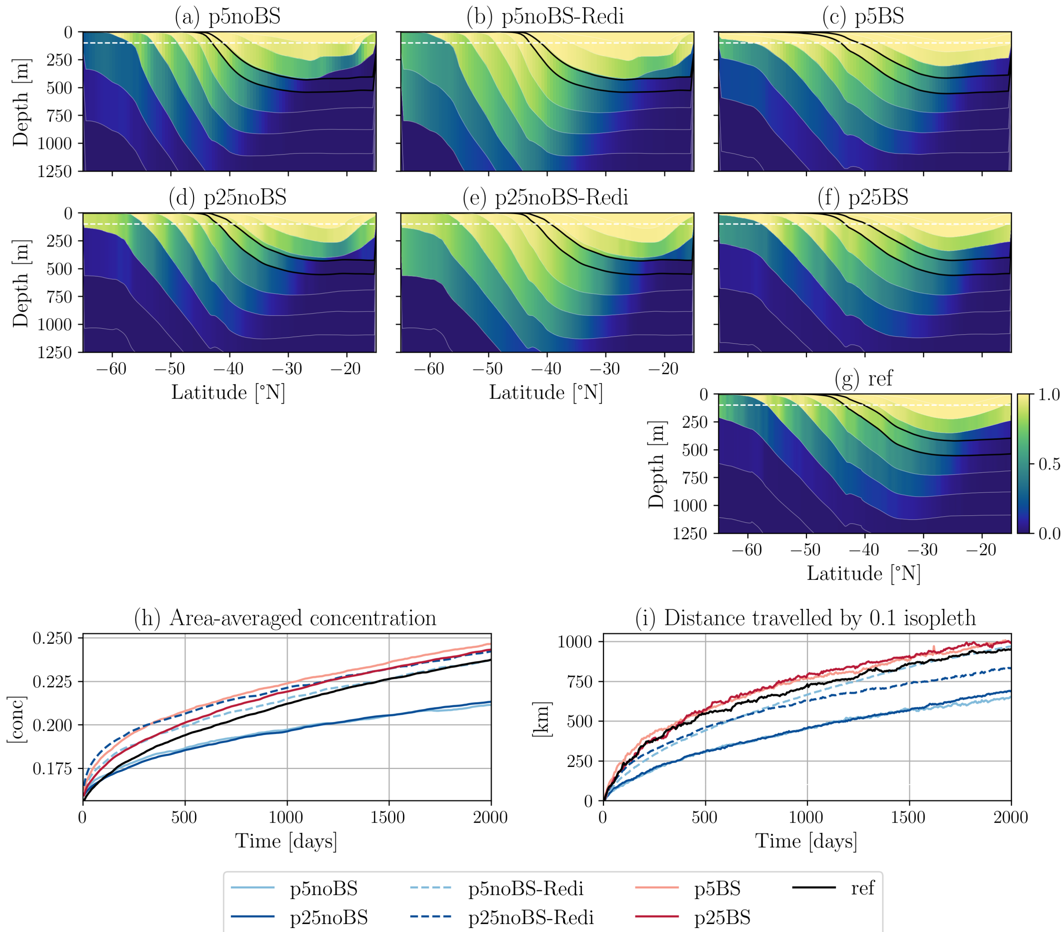

Figure 13: (a–g) Zonally averaged ventilation tracer after 2,000 days shown between −65°N and −15°N in the (a) p5noBS, (b) p5noBS-Redi, (c) p5BS, (d) p25noBS, (e) p25noBS-Redi, (f) p25BS, and (g) ref simulations. Thin white lines show zonally averaged isopycnal interfaces, and the black contoured isopycnal is the first layer to outcrop only in the Southern Ocean. Quantities on this layer are shown in (h–i): (h) the area-averaged tracer concentration and (i) the average meridional distance travelled by the 0.1 isopleth of the tracer.

centration on the deeper outcropping layers (Figure 13b, e) due to an inaccurate vertical structure for the parameterized diffusivity; this might be mitigated by a different choice of vertical structure (see Section 2.4). The p5BS and p25BS simulations show the closest resemblance to the ref simulation in terms of both growth over time and the vertical distribution of the tracer (Figure 13c, f, g, h).

The northward advance of the 0.1 tracer isopleth gives a clear indication of tracer *mixing* across the simulations (Figure 13i). The 0.1 isopleth advances into the interior more slowly for the unparameterized simulations, showing a bias of roughly 300 km after 2,000 days. Adding isopycnal tracer diffusion generally reduces this bias, although the effect of the horizontal resolution function is clearly seen in the p25noBS-Redi simulation at roughly 1,000 days, where the procession slows. The backscatter simulations show the closest resemblance to the ref simulation overall, although slightly overestimate the mean distance travelled after 2,000 days by about 30 km. These results are consistent with the findings of Abernathey and Ferreira (2015), where higher eddy activity (in their case due to stronger winds) drives enhanced ventilation through intensified isopycnal mixing.

4. Summary and discussion

We have evaluated the effect of a kinetic energy backscatter parameterization on isopycnal mixing at eddy-permitting resolutions in a basin-scale configuration of MOM6. In this study, the backscatter parameterization is formulated as a negative harmonic viscosity in the momentum equations, whose magnitude is informed by a local prognostic subgrid energy budget, and acts to reenergize eddies that are spuriously dissipated by a biharmonic viscosity. Importantly, the backscatter parameterization is not combined with additional GM or Redi parameterizations for eddy-driven overturning and eddy-induced along-isopycnal tracer diffusion, respectively. We have assessed the representation of isopycnal mixing by diagnosing the three-dimensional structure of isopycnal diffusivities via a multiple tracer inversion method.

The main results are summarized here:

1. Simulations with no mesoscale parameterization in this model, at both 1/2° and 1/4° resolutions, show subdued isopycnal mixing (Figure 6) and consequent tracer biases (Figures 12 and 13), largely as a result of subdued eddy activity (Figure 3). In these simulations, the globally integrated kinetic energy is roughly four times smaller than a coarsened 1/32° simulation (Figure 2a), and the predominantly meridional diffusivity is similarly four times too small on the global average compared to the 1/32° simulation (Figure 10d). Isopycnals are also too steep in the unparameterized simulations, due to a poorly resolved baroclinic energy cycle, which leads to inaccurate outcrop locations in the reentrant channel that mimics the Southern Ocean in the model (Figure 5).

2. Simulations employing the backscatter parameterization show elevated isopycnal diffusivities, which largely track the increases in eddy kinetic energy (compare Figures 3 and 6, and Figures 4 and 7). When compared to the 1/32° reference simulation, the results overall suggest that no supplemental isopycnal diffusion is needed in these backscatter simulations. The predominantly meridional diffusivity in the backscatter simulations is comparable to, and in some cases exceeds, that in the 1/32° simulation. The backscatter simulations are unable to match extremes in the distribution of the predominantly zonal diffusivity in the 1/32° simulation (Figure 10a); however, such extremes may arise from zonal shear flows that are unresolved at coarser resolutions, which produce locally intense along-flow transports (Figure 9). The backscatter parameterization also leads to reductions in both mean and variance biases of passive tracers (Figure 12) as well as an improved representation of an idealized ventilation tracer (Figure 13) relative to the 1/32° simulation.

3. Simulations that use a traditional isopycnal diffusion ("Redi") parameterization show reduced mean tracer biases (Figure 12) and increased uptake of the ventilation tracer (Figure 13) relative to unparameterized simulations. However, the isopycnal diffusion parameterization also diffuses the tracer signature of resolved eddy variability, leading to increases in tracer variance biases (Figure 12).

Taken together, these results indicate that isopycnal diffusivities are expected to be low where eddy activity is low, and that, by reenergizing eddies, a backscatter parameterization can lead to an improved representation of isopycnal mixing. Juricke et al. (2020) showed in a global model configuration that parameterizing backscatter can reduce tracer biases where eddy activity is better represented, while biases can *increase* in regions where eddy activity is over-intensified. An important result from the present study is that the strength of backscatter-parameterized isopycnal mixing is affected not only by the eddy kinetic energy but also by the dominant eddy length scale, as anticipated from mixing length arguments. In the 1/2° backscatter simulation, the energy-containing scale is generally larger than in the 1/32° simulation by about 10–20 km (Figure 3g), which likely occurs because the energy-containing scale in the 1/32° simulation is at or below the 1/2° grid spacing; this contributes to isopycnal diffusivities being too large at 1/2° (Figure 6i). In the 1/4° backscatter simulation, the energy-containing scale is more in line with the 1/32° simulation (Figure 3g), and isopycnal diffusivities are in turn more similar between these simulations (Section 3.2). Joint consideration should thus be given to both the eddy energy *and* eddy length scales when parameterizing isopycnal mixing via backscatter. Encouragingly, results from simulations that varied the strength of backscatter via the magnitude of the negative viscosity (Equation (5)) demonstrated that the energy-containing scale did not vary much at fixed resolution, and that increases in isopycnal diffusivities generally followed increases in eddy energy (Figure 11). These results suggest that the magnitude of the negative viscosity could be a useful knob to control the strength of isopycnal mixing in more realistic global configurations where eddy activity is partially resolved but spuriously low. Further work is, of course, needed to confirm the degree to which this holds in realistic global models, and we hope the results in the present study motivate such work.

Due to our idealized model configuration, several important effects remain to be explored to achieve implementation in realistic global models. Our model is purely adiabatic with a single thermodynamic constituent, while temperature and salinity gradients can compensate and thus coexist along isopycnals in the ocean. Recent studies (Holmes et al., 2022; Neumann & Jones, 2025) have shown that enhanced isopycnal mixing can have indirect diabatic impacts through interactions with surface buoyancy fluxes and via nonlinear equation of state effects, in particular in the Southern Ocean, thus modifying circulation and water mass transformation processes. It will thus be important to understand the dual effect of backscatter-parameterized eddies to modify stratification via adiabatic APE extraction versus diabatic effects that arise from enhanced isopycnal mixing, especially in the Southern Ocean where a backscatter parameterization already likely generates strong responses (Juricke et al., 2020; Chang et al., 2023; Yassin et al., 2025). Further work is needed to test sensitivity to other aspects of the parameterization, such as the vertical structure, which has been shown to influence the resolved stratification in idealized models (Yankovsky et al., 2024) and whose effects may differ in more realistic models. Interactions with other processes absent from the model used in this study, such as mixed layer and vertical mixing processes and their parameterizations, are another important consideration for global model implementation and warrant future attention. It would also be of interest to assess the implications of elevated tracer variability at the mesoscale via a backscatter parameterization for air–sea fluxes (Bishop et al., 2017; Gehlen et al., 2020) as well as reactive biogeochemical tracers (Lévy et al., 2014).

Finally, we note that the backscatter scheme used in this study is primarily a numerical, rather than a physical, backscatter parametrization, as it acts to counteract the excessive dissipation resulting from the biharmonic viscous closure. Recent work (Silvestri et al., 2024; Zhang et al., 2025) has suggested that improved numerics could obviate the need for an explicit viscous closure. This may reduce the spurious damping of resolved kinetic energy and thereby increase the effective resolution of eddy-permitting simulations. Even with such improved numerical schemes, however, there is likely still to be some excessive dissipation at small scales relative to a higher resolution simulation, which may affect large-scale fields because of missing energy sources for upscale cascades. A numerical backscatter parameterization could thus still be of use in this scenario (e.g., Zhang et al., 2025). Moreover, physical backscatter parameterizations which target missing *physics*, such as the energization of mesoscale flows via submesoscale inverse cascades (Steinberg et al., 2022; Garabato et al., 2022), will remain relevant as long as such processes are partially or not resolved.

Our study has demonstrated that a resolved flow, appropriately energized by a backscatter parameterization, can generate realistic isopycnal mixing. Many open questions remain regarding how to optimally implement such a parameterization in a global model to balance the various effects that increased eddy activity may have. However, backscatter parameterizations can likely contribute to a more faithful representation of mesoscale eddy activity and associated eddy-induced mixing effects in the challenging eddy-permitting regime of ocean climate models.

A. Further results for thickness-weighted eddy tracer fluxes

Here, we present equations for the thickness-weighted mean and eddy tracer variances, $\hat{c}^2$ and $\widehat{c''^2}$, that follow from Equation (11). Following these equations, we discuss the effect of the eddy tracer flux $\mathbf{F}^c$ (Equation (12)) on tracer variance in order to clarify our focus on the symmetric part of the eddy tracer flux (see Section 2.3.2).

A.1. Mean and eddy tracer variance equations

The mean tracer variance equation is found by first rewriting the TWA tracer equation (Equation (11)) in an advective form, multiplying by $\overline{h}\hat{c}$, and then making use of the averaged thickness equation (Equation (2)).

The result is

$$\partial_t\left(\overline{h}\frac{\hat{c}^2}{2}\right) + \nabla\cdot\left(\overline{h}\hat{\mathbf{u}}\frac{\hat{c}^2}{2}\right) + \nabla\cdot\left(\overline{h}\hat{c}\mathbf{F}^c\right) = \overline{h}\nabla\hat{c}\cdot\mathbf{F}^c. \tag{30}$$

The eddy tracer variance can be written as $\widehat{c''^2} = \widehat{c^2} - \hat{c}^2$ following usual Reynolds assumptions (see Young, 2012). An equation for $\widehat{c^2}$ is found by noting that c^2 also satisfies Equation (3), averaging this equation for c^2, and again applying Reynolds assumptions to simplify the triple products. Subtracting Equation (30) from the resulting equation yields the eddy tracer variance equation

$$\partial_t\left(\overline{h}\frac{\widehat{c''^2}}{2}\right) + \nabla\cdot\left(\overline{h}\hat{\mathbf{u}}\frac{\widehat{c''^2}}{2}\right) + \nabla\cdot\left(\overline{h}\frac{\widehat{\mathbf{u}''c''^2}}{2}\right) = -\overline{h}\nabla\hat{c}\cdot\mathbf{F}^c. \tag{31}$$

Equations (30) and (31) are similar to Equations (89) and (90) in Young (2012), except that Young's equations are defined in a basis which differs to the basis that defines the numerical model's coordinate system (Section 2.1) (see also Jansen et al., 2024); this difference is the reason we present these equations here.

The main point here is that the right hand sides of Equations (30) and (31) differ by a sign and sum to zero. These are the eddy-mean transfer terms in a thickness-weighted framework. As discussed next, if a flux-gradient relationship is assumed (Equation (13)), then only the symmetric part of the mixing tensor affects these eddy-mean transfer terms.

A.2. Antisymmetric and symmetric eddy tracer fluxes

Of the four degrees of freedom in the mixing tensor $\mathsf{K} \in \mathbb{R}^{2\times 2}$, only one comes from the antisymmetric part $\mathsf{A} = (\mathsf{K} - \mathsf{K}^{\mathrm{T}})/2$; namely,

$$\mathsf{A} = \begin{bmatrix} 0 & \psi \\ -\psi & 0 \end{bmatrix},$$

where ψ is a scalar. The eddy flux associated with the antisymmetric part of K, i.e., $\mathbf{F}^c_{\mathsf{A}} \equiv -\mathsf{A}\nabla\hat{c}$, can therefore be written as

$$-\mathsf{A}\nabla\hat{c} = \psi\nabla^{\perp}\hat{c}, \tag{32}$$

where $\nabla^{\perp} = -\partial_y\mathbf{i} + \partial_x\mathbf{j}$. Since $\nabla\hat{c}\cdot\left(\psi\nabla^{\perp}\hat{c}\right) = 0$, Equations (30) and (31) imply that $\mathbf{F}^c_{\mathsf{A}}$ has no effect on tracer variance.

It is thus clear that only the eddy flux associated with the symmetric part of K, i.e., $\mathbf{F}^c_{\mathsf{S}} \equiv -\mathsf{S}\nabla\hat{c}$, can affect tracer variance (Equations (30) and (31)). Denoting rotation of a vector into the coordinate system defined by the orthonormal columns of U as

$$\tilde{\mathbf{a}} \equiv \mathsf{U}^{\mathrm{T}}\mathbf{a}, \tag{33}$$

then it follows that the right hand side of the mean tracer variance equation (Equation (30)) can be written as

$$\overline{h}\nabla\hat{c}\cdot\mathbf{F}^c = -\overline{h}\widetilde{\nabla\hat{c}}\cdot\left(\mathsf{D}\widetilde{\nabla\hat{c}}\right), \tag{34}$$

which is negative-definite if the entries of D, i.e., the isopycnal diffusivities (Equation (15)), are positive. When globally integrated, the right hand side of Equation (34) in fact *must* be negative to balance dissipation of tracer variance. (Dissipation is not written explicitly in Equations (30) or (31) but is achieved through the action of molecular or numerical diffusion.) The effect of S is therefore referred to as "mixing" as it acts as a global sink of mean tracer variance. It is this variance-reducing mixing that is targeted by typical isopycnal mixing parameterizations (e.g., Redi, 1982).

B. Error estimation from the Method of Multiple Tracers

Here, we describe an error estimation method for the Method of Multiple Tracers inversion described in Section 2.3.3. Since the inversion is a least squares regression, the error estimation method amounts to computing the standard errors of the coefficients (i.e., the standard deviation on the estimated coefficients) that define the least squares solution K_{lsq} (Equation (18)).

To render the overdetermined matrix equation (Equation (17)) in a more intuitive matrix-vector formulation to apply ordinary least squares results, we vectorize Equation (17) to become

$$\mathbf{F} = \mathsf{M}\mathbf{K}, \tag{35}$$

where $\mathbf{F} \equiv \text{vec}(\mathsf{F}) \in \mathbb{R}^{2m}$, $\mathbf{K} \equiv \text{vec}(\mathsf{K}) \in \mathbb{R}^4$ and $\mathsf{M} \equiv -(\mathsf{G}^{\text{T}} \bigotimes I_2) \in \mathbb{R}^{2m\times 4}$, where $\bigotimes$ is the Kronecker product and I_2 is the 2×2 identity matrix. As in Equation (18), the least squares estimates for the entries of $\mathbf{K}$ can be expressed as

$$\mathbf{K}_{\text{lsq}} = \mathsf{M}^{\dagger}\mathbf{F}, \tag{36}$$

with residuals then given by

$$\mathbf{r} = \mathbf{F} - \mathsf{M}\mathbf{K}_{\text{lsq}}. \tag{37}$$

To proceed, we assume that the residuals (i.e., errors) are independent and identically distributed as well as homoskedastic. The sample variance of the errors is then

$$s^2 = \frac{1}{2m-4}\|\mathbf{r}\|^2, \tag{38}$$

where $2m - 4$ are the statistical degrees of freedom from Equation (35), and the covariance matrix of $\mathbf{K}$ is

$$\text{cov}(\mathbf{K}) = s^2(\mathsf{M}^{\text{T}}\mathsf{M})^{-1}. \tag{39}$$

The standard errors of the entries K_i of $\mathbf{K}$ are then

$$\text{se}(K_i) = \sqrt{\left(\text{cov}(\mathbf{K})\right)_{ii}}, \tag{40}$$

for $i = 1, \ldots, 4$.

We then relate this expression for the standard errors in $\mathbf{K}$ to the standard errors in the eigenvalues $\varkappa_1$ and $\varkappa_2$ of S (Equation (15)). To do this, we first define a function $\mathbf{f}$ that maps the entries of $\mathbf{K}$ to the eigenvalues $\varkappa_1$ and $\varkappa_2$, i.e., $\mathbf{k} = \mathbf{f}(\mathbf{K})$ where $\mathbf{k} \equiv (\varkappa_1, \varkappa_2)^{\text{T}}$ and (via a simple exercise in linear algebra)

$$\varkappa_1 = \frac{K_{11}+K_{22}}{2} + \sqrt{\left(\frac{K_{11}-K_{22}}{2}\right)^2 + K_{12}^2}, \tag{41}$$

$$\varkappa_2 = \frac{K_{11}+K_{22}}{2} - \sqrt{\left(\frac{K_{11}-K_{22}}{2}\right)^2 + K_{12}^2}, \tag{42}$$

where the K_{ij} are the elements of the unvectorized matrix K. We then assume that errors propagate to first-order by

$$\text{cov}(\mathbf{k}) = \mathsf{J}\text{cov}(\mathbf{K})\mathsf{J}^{\text{T}}, \tag{43}$$

where $\mathsf{J} = \partial\mathbf{f}/\partial\mathbf{K} \in \mathbb{R}^{2\times 4}$. The standard errors in the eigenvalues are then, as in Equation (40),

$$\text{se}(\varkappa_i) = \sqrt{\left(\text{cov}(\mathbf{k})\right)_{ii}} \tag{44}$$

for $i = 1, 2$. Figure B1 shows the depth-averaged standard errors for $\varkappa_1$ and $\varkappa_2$, which can be compared to Figure 6.

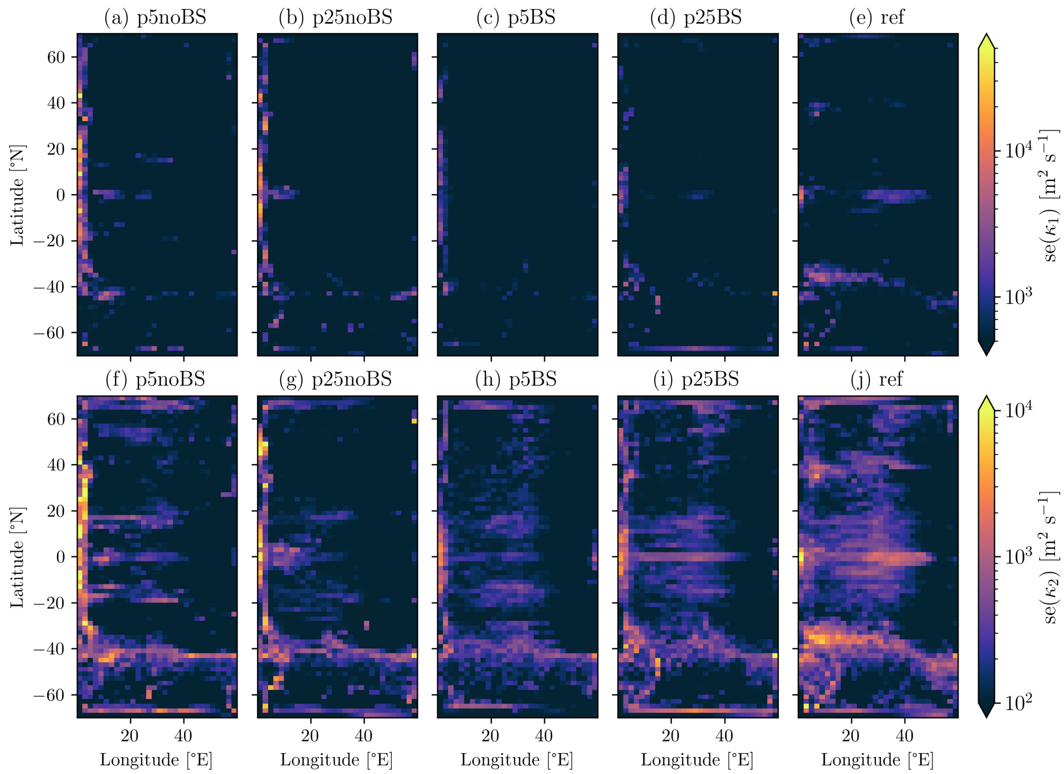

Figure B1: Depth-averaged standard errors (se) for the isopycnal diffusivities from Equation (44). (a–e) se(κ_1) (on a log color scale) in the (a) p5noBS, (b) p25noBS, (c) p5BS, (d) p25BS, and (e) ref simulations. (f–k) As in (a–e) but for se(κ_2).

Open Research Statement

The MOM6 source code used to run the simulations is frozen in a Zenodo repository (Hallberg et al., 2025). Configuration files for the simulations and python scripts to reproduce the figures in this article are also available at Pudig (2025).

Acknowledgements:
The authors acknowledge support from the National Science Foundation (NSF) and National Oceanic and Atmospheric Administration (NOAA) grant "Climate Process Team: Ocean Transport and Eddy Energy" (NSF OCE 1912357 and NOAA CVP NA19OAR4310364), and thank the entire CPT team for useful input on this work. This work was supported by the New York University IT High Performance Computing resources, services and staff expertise.

References

Abernathey, R., & Ferreira, D. (2015). Southern Ocean isopycnal mixing and ventilation changes driven by winds. *Geophysical Research Letters*, *42*(23), 10,357–10,365. doi: 10.1002/2015GL066238

Abernathey, R., Ferreira, D., & Klocker, A. (2013). Diagnostics of isopycnal mixing in a circumpolar channel. *Ocean Modelling*, *72*, 1–16. doi: 10.1016/j.ocemod.2013.07.004

Abernathey, R., Gnanadesikan, A., Pradal, M.-A., & Sundermeyer, M. A. (2022). Chapter 9 - Isopycnal mixing. In M. Meredith & A. Naveira Garabato (Eds.), *Ocean Mixing* (pp. 215–256). Elsevier.

Abernathey, R., & Marshall, J. (2013). Global surface eddy diffusivities derived from satellite altimetry. *Journal of Geophysical Research: Oceans*, *118*(2), 901–916. doi: 10.1002/jgrc.20066

Adcroft, A., Anderson, W., Balaji, V., Blanton, C., Bushuk, M., Dufour, C. O., ... Zhang, R. (2019). The GFDL Global Ocean and Sea Ice Model OM4.0: Model Description and Simulation Features. *Journal of Advances in Modeling Earth Systems*, *11*(10), 3167–3211. doi: 10.1029/2019MS001726

Andrews, D. G. (1983). A Finite-Amplitude Eliassen-Palm Theorem in Isentropic Coordinates. *Journal of the Atmospheric Sciences*, *40*(8), 1877–1883. doi: 10.1175/1520-0469(1983)040<1877:AFAEPT>2.0.CO;2

Bachman, S., & Fox-Kemper, B. (2013). Eddy parameterization challenge suite I: Eady spindown. *Ocean Modelling*, *64*, 12–28. doi: 10.1016/j.ocemod.2012.12.003

Bachman, S., Fox-Kemper, B., & Bryan, F. O. (2015). A tracer-based inversion method for diagnosing eddy-induced diffusivity and advection. *Ocean Modelling*, *86*, 1–14. doi: 10.1016/j.ocemod.2014.11.006

Balwada, D., Smith, K. S., & Abernathey, R. (2018). Submesoscale Vertical Velocities Enhance Tracer Subduction in an Idealized Antarctic Circumpolar Current. *Geophysical Research Letters*, *45*(18), 9790–9802. doi: 10.1029/2018GL079244

Balwada, D., Speer, K. G., LaCasce, J. H., Owens, W. B., Marshall, J., & Ferrari, R. (2016). Circulation and Stirring in the Southeast Pacific Ocean and the Scotia Sea Sectors of the Antarctic Circumpolar Current. *Journal of Physical Oceanography*, *46*(7), 2005–2027. doi:

10.1175/JPO-D-15-0207.1

Bishop, S. P., Small, R. J., Bryan, F. O., & Tomas, R. A. (2017). Scale Dependence of Midlatitude Air–Sea Interaction. *Journal of Climate*, *30*(20), 8207–8221. doi: 10.1175/JCLI-D-17-0159.1

Bisits, J. I., Stanley, G. J., & Zika, J. D. (2023). Can We Accurately Quantify a Lateral Diffusivity from a Single Tracer Release? *Journal of Physical Oceanography*, *53*(2), 647–659. doi: 10.1175/JPO-D-22-0145.1

Bratseth, A. M. (1998). On the estimation of transport characteristics of atmospheric data sets. *Tellus A: Dynamic Meteorology and Oceanography*, *50*(4), 451. doi: 10.3402/tellusa.v50i4.14538

Cessi, P. (2008). An Energy-Constrained Parameterization of Eddy Buoyancy Flux. *Journal of Physical Oceanography*, *38*(8), 1807–1819. doi: 10.1175/2007JPO3812.1

Chang, C.-Y., Adcroft, A., Zanna, L., Hallberg, R., & Griffies, S. M. (2023). Remote Versus Local Impacts of Energy Backscatter on the North Atlantic SST Biases in a Global Ocean Model. *Geophysical Research Letters*, *50*(21), e2023GL105757. doi: 10.1029/2023GL105757

Chelton, D. B., Schlax, M. G., & Samelson, R. M. (2011). Global observations of nonlinear mesoscale eddies. *Progress in Oceanography*, *91*(2), 167–216. doi: 10.1016/j.pocean.2011.01.002

Chen, R., McClean, J. L., Gille, S. T., & Griesel, A. (2014, August). Isopycnal Eddy Diffusivities and Critical Layers in the Kuroshio Extension from an Eddying Ocean Model. *Journal of Physical Oceanography*, *44*(8), 2191–2211. doi: 10.1175/JPO-D-13-0258.1

Chouksey, A., Griesel, A., Chouksey, M., & Eden, C. (2022). Changes in Global Ocean Circulation due to Isopycnal Diffusion. *Journal of Physical Oceanography*, *52*(9), 2219–2235. doi: 10.1175/JPO-D-21-0205.1

Cole, S. T., Wortham, C., Kunze, E., & Owens, W. B. (2015). Eddy stirring and horizontal diffusivity from Argo float observations: Geographic and depth variability. *Geophysical Research Letters*, *42*(10), 3989–3997. doi: 10.1002/2015GL063827

Couespel, D., Lévy, M., & Bopp, L. (2021). Oceanic primary production decline halved in eddy-resolving simulations of global warming. *Biogeosciences*, *18*(14), 4321–4349. doi: 10.5194/bg-18-4321-2021

Danabasoglu, G., McWilliams, J. C., & Gent, P. R. (1994). The Role of Mesoscale Tracer Transports in the Global Ocean Circulation. *Science*, *264*(5162), 1123–1126. doi: 10.1126/science.264.5162.1123

Delworth, T. L., Rosati, A., Anderson, W., Adcroft, A. J., Balaji, V., Benson, R., … Zhang, R. (2012). Simulated Climate and Climate Change in the GFDL CM2.5 High-Resolution Coupled Climate Model. *Journal of Climate*, *25*(8), 2755–2781. doi: 10.1175/JCLI-D-11-00316.1

de Szoeke, R. A., & Bennett, A. F. (1993). Microstructure Fluxes across Density Surfaces. *Journal of Physical Oceanography*, *23*(10), 2254–2264. doi: 10.1175/1520-0485(1993)023<2254:MFADS>2.0.CO;2

Eden, C., & Greatbatch, R. J. (2008). Towards a mesoscale eddy closure. *Ocean Modelling*, *20*(3), 223–239. doi: 10.1016/j.ocemod.2007.09.002

England, M. H. (1995). The Age of Water and Ventilation Timescales in a Global Ocean Model. *Journal of Physical Oceanography*, *25*(11), 2756–2777. doi: 10.1175/1520-0485(1995)025<2756:TAOWAV>2.0.CO;2

England, M. H., & Rahmstorf, S. (1999). Sensitivity of Ventilation Rates and Radiocarbon Uptake to Subgrid-Scale Mixing in Ocean Models. *Journal of Physical Oceanography*, *29*(11), 2802–2828. doi: 10.1175/1520-0485(1999)029<2802:SOVRAR>2.0.CO;2

Ferrari, R., & Nikurashin, M. (2010). Suppression of Eddy Diffusivity across Jets in the Southern Ocean. *Journal of Physical Oceanography*, *40*(7), 1501–1519. doi: 10.1175/2010JPO4278.1

Fox-Kemper, B., Adcroft, A., Böning, C. W., Chassignet, E. P., Curchitser, E., Danabasoglu, G., … Yeager, S. G. (2019). Challenges and Prospects in Ocean Circulation Models. *Frontiers in Marine Science*, *6*. doi: 10.3389/fmars.2019.00065

Fox-Kemper, B., Lumpkin, R., & Bryan, F. O. (2013). Chapter 8 - Lateral Transport in the Ocean Interior. In G. Siedler, S. M. Griffies, J. Gould, & J. A. Church (Eds.), *International Geophysics* (Vol. 103, pp. 185–209). Academic Press. doi: 10.1016/B978-0-12-391851-2.00008-8

Garabato, A. C. N., Yu, X., Callies, J., Barkan, R., Polzin, K. L., Frajka-Williams, E. E., … Griffies, S. M. (2022). Kinetic Energy Transfers between Mesoscale and Submesoscale Motions in the Open Ocean's Upper Layers. *Journal of Physical Oceanography*, *52*(1), 75–97. (Section: Journal of Physical Oceanography) doi: 10.1175/JPO-D-21-0099.1

Gehlen, M., Berthet, S., Séférian, R., Ethé, C., & Penduff, T. (2020). Quantification of Chaotic Intrinsic Variability of Sea-Air CO2 Fluxes at Interannual Timescales. *Geophysical Research Letters*, *47*(22), e2020GL088304. doi: 10.1029/2020GL088304

Gent, P. R. (2011). The Gent–McWilliams parameterization: 20/20 hindsight. *Ocean Modelling*, *39*(1), 2–9. doi: 10.1016/j.ocemod.2010.08.002

Gent, P. R., & McWilliams, J. C. (1990). Isopycnal Mixing in Ocean Circulation Models. *Journal of Physical Oceanography*, *20*(1), 150–155. doi: 10.1175/1520-0485(1990)020<0150:IMIOCM>2.0.CO;2

Gent, P. R., Willebrand, J., McDougall, T. J., & McWilliams, J. C. (1995). Parameterizing Eddy-Induced Tracer Transports in Ocean Circulation Models. *Journal of Physical Oceanography*, *25*(4), 463–474. doi: 10.1175/1520-0485(1995)025<0463:PEITTI>2.0.CO;2

Gnanadesikan, A., Bianchi, D., & Pradal, M.-A. (2013). Critical role for mesoscale eddy diffusion in supplying oxygen to hypoxic ocean waters. *Geophysical Research Letters*, *40*(19), 5194–5198. doi: 10.1002/grl.50998

Gnanadesikan, A., Pradal, M.-A., & Abernathey, R. (2015a). Exploring the isopycnal mixing and helium–heat paradoxes in a suite of Earth system models. *Ocean Science*, *11*(4), 591–605. doi: 10.5194/os-11-591-2015

Gnanadesikan, A., Pradal, M.-A., & Abernathey, R. (2015b). Isopycnal mixing by mesoscale eddies significantly impacts oceanic anthropogenic carbon uptake. *Geophysical Research Letters*, *42*(11), 4249–4255. doi: 10.1002/2015GL064100

Gnanadesikan, A., Russell, A., Pradal, M.-A., & Abernathey, R. (2017). Impact of Lateral Mixing in the Ocean on El Nino in a Suite of Fully Coupled Climate Models. *Journal of Advances in Modeling Earth Systems*, *9*(7), 2493–2513. doi: 10.1002/2017MS000917

Gough, W., & Lin, C. (1995). Isopycnal mixing and the Veronis effect in an ocean general circulation model. *Journal of Marine Research*, *53*(2).

Gower, J. F. R., Denman, K. L., & Holyer, R. J. (1980). Phytoplankton patchiness indicates the fluctuation spectrum of mesoscale oceanic structure. *Nature*, *288*(5787), 157–159. doi: 10.1038/288157a0

Griffies, S. M. (1998). The Gent–McWilliams Skew Flux. *Journal of Physical Oceanography*, *28*(5), 831–841. doi: 10.1175/1520-0485(1998)028<0831:TGMSF>2.0.CO;2

Griffies, S. M., Adcroft, A., Beadling, R. L., Bushuk, M., Chang, C.-Y., Drake, H. F., … Zhao, M. (2024). The GFDL-CM4X climate model hierarchy, Part I: model description and thermal properties. *Authorea Preprints*. doi: 10.22541/essoar.173282145.53065190/v1

Griffies, S. M., Adcroft, A., & Hallberg, R. W. (2020). A Primer on the Vertical Lagrangian-Remap Method in Ocean Models Based on Finite Volume Generalized Vertical Coordinates. *Journal of Advances in Modeling Earth Systems*, *12*(10), e2019MS001954. doi: 10.1029/2019MS001954

Griffies, S. M., & Hallberg, R. W. (2000). Biharmonic Friction with a Smagorinsky-Like Viscosity for Use in Large-Scale Eddy-Permitting Ocean Models. *Monthly Weather Review*, *128*(8), 2935–2946. doi: 10.1175/1520-0493(2000)128<2935:BFWASL>2.0.CO;2

Griffies, S. M., Winton, M., Anderson, W. G., Benson, R., Delworth, T. L., Dufour, C. O., … Zhang, R. (2015). Impacts on Ocean Heat from Transient Mesoscale Eddies in a Hierarchy of Climate Models. *Journal of Climate*, *28*(3), 10.1175/JCLI–D–14–00353.1. doi:

10.1175/JCLI-D-14-00353.1

Groeskamp, S., LaCasce, J. H., McDougall, T. J., & Rogé, M. (2020). Full-Depth Global Estimates of Ocean Mesoscale Eddy Mixing From Observations and Theory. *Geophysical Research Letters*, *47*(18), e2020GL089425. doi: 10.1029/2020GL089425

Groeskamp, S., Sloyan, B. M., Zika, J. D., & McDougall, T. J. (2017). Mixing Inferred from an Ocean Climatology and Surface Fluxes. *Journal of Physical Oceanography*, *47*(3), 667–687. doi: 10.1175/JPO-D-16-0125.1

Hallberg, R. (2013). Using a resolution function to regulate parameterizations of oceanic mesoscale eddy effects. *Ocean Modelling*, *72*, 92–103. doi: 10.1016/j.ocemod.2013.08.007

Hallberg, R., Adcroft, A., Ward, M., Marques, G., Hedstrom, K., Altuntas, A., … Jansen, M. (2025). *mpudig/MOM6-GFDL: JAMES_isopycnalmixingbackscatter.* Zenodo. doi: 10.5281/zenodo.17087553

Hewitt, H. T., Roberts, M., Mathiot, P., Biastoch, A., Blockley, E., Chassignet, E. P., … Zhang, Q. (2020). Resolving and Parameterising the Ocean Mesoscale in Earth System Models. *Current Climate Change Reports*, *6*(4), 137–152. doi: 10.1007/s40641-020-00164-w

Holmes, R. M., Groeskamp, S., Stewart, K. D., & McDougall, T. J. (2022). Sensitivity of a Coarse-Resolution Global Ocean Model to a Spatially Variable Neutral Diffusivity. *Journal of Advances in Modeling Earth Systems*, *14*(3), e2021MS002914. doi: 10.1029/2021MS002914

Iselin, C. O. (1939). The influence of vertical and lateral turbulence on the characteristics of the waters at mid-depths. *Eos, Transactions American Geophysical Union*, *20*(3), 414–417. doi: 10.1029/TR020i003p00414

Jansen, M. F., Adcroft, A., Griffies, S. M., & Grooms, I. (2024). The Averaged Hydrostatic Boussinesq Ocean Equations in Generalized Vertical Coordinates. *Journal of Advances in Modeling Earth Systems*, *16*(12), e2024MS004506. doi: 10.1029/2024MS004506

Jansen, M. F., Adcroft, A., Khani, S., & Kong, H. (2019). Toward an Energetically Consistent, Resolution Aware Parameterization of Ocean Mesoscale Eddies. *Journal of Advances in Modeling Earth Systems*, *11*(8), 2844–2860. doi: 10.1029/2019MS001750

Jansen, M. F., & Held, I. M. (2014). Parameterizing subgrid-scale eddy effects using energetically consistent backscatter. *Ocean Modelling*, *80*, 36–48. doi: 10.1016/j.ocemod.2014.06.002

Jansen, M. F., Held, I. M., Adcroft, A., & Hallberg, R. (2015). Energy budget-based backscatter in an eddy permitting primitive equation model. *Ocean Modelling*, *94*, 15–26. doi: 10.1016/j.ocemod.2015.07.015

Jones, C. S., & Abernathey, R. P. (2019). Isopycnal Mixing Controls Deep Ocean Ventilation. *Geophysical Research Letters*, *46*(22), 13144–13151. doi: 10.1029/2019GL085208

Juricke, S., Danilov, S., Koldunov, N., Oliver, M., & Sidorenko, D. (2020). Ocean Kinetic Energy Backscatter Parametrization on Unstructured Grids: Impact on Global Eddy-Permitting Simulations. *Journal of Advances in Modeling Earth Systems*, *12*(1), e2019MS001855. doi: 10.1029/2019MS001855

Juricke, S., Danilov, S., Kutsenko, A., & Oliver, M. (2019). Ocean kinetic energy backscatter parametrizations on unstructured grids: Impact on mesoscale turbulence in a channel. *Ocean Modelling*, *138*, 51–67. doi: 10.1016/j.ocemod.2019.03.009

Kiss, A. E., Hogg, A. M., Hannah, N., Boeira Dias, F., Brassington, G. B., Chamberlain, M. A., … Zhang, X. (2020). ACCESS-OM2 v1.0: a global ocean–sea ice model at three resolutions. *Geoscientific Model Development*, *13*(2), 401–442. doi: 10.5194/gmd-13-401-2020

Kjellsson, J., & Zanna, L. (2017). The Impact of Horizontal Resolution on Energy Transfers in Global Ocean Models. *Fluids*, *2*(3), 45. doi: 10.3390/fluids2030045

Klocker, A., & Abernathey, R. (2014). Global Patterns of Mesoscale Eddy Properties and Diffusivities. *Journal of Physical Oceanography*, *44*(3), 1030–1046. doi: 10.1175/JPO-D-13-0159.1

Klocker, A., Ferrari, R., & LaCasce, J. H. (2012). Estimating Suppression of Eddy Mixing by Mean Flows. *Journal of Physical Oceanography*, *42*(9), 1566–1576. doi: 10.1175/JPO-D-11-0205.1

Klocker, A., & Marshall, D. P. (2014). Advection of baroclinic eddies by depth mean flow. *Geophysical Research Letters*, *41*(10), 3517–3521. doi: 10.1002/2014GL060001

Klöwer, M., Jansen, M. F., Claus, M., Greatbatch, R. J., & Thomsen, S. (2018). Energy budget-based backscatter in a shallow water model of a double gyre basin. *Ocean Modelling*, *132*, 1–11. doi: 10.1016/j.ocemod.2018.09.006

LaCasce, J. H. (2008). Statistics from Lagrangian observations. *Progress in Oceanography*, *77*(1), 1–29. doi: 10.1016/j.pocean.2008.02.002

Larichev, V. D., & Held, I. M. (1995). Eddy Amplitudes and Fluxes in a Homogeneous Model of Fully Developed Baroclinic Instability. *Journal of Physical Oceanography*, *25*(10), 2285–2297. doi: 10.1175/1520-0485(1995)025<2285:EAAFIA>2.0.CO;2

Ledwell, J. R., Watson, A. J., & Law, C. S. (1998). Mixing of a tracer in the pycnocline. *Journal of Geophysical Research: Oceans*, *103*(C10), 21499–21529. doi: 10.1029/98JC01738

Loose, N., Marques, G. M., Adcroft, A., Bachman, S., Griffies, S. M., Grooms, I., … Jansen, M. F. (2023). Comparing Two Parameterizations for the Restratification Effect of Mesoscale Eddies in an Isopycnal Ocean Model. *Journal of Advances in Modeling Earth Systems*, *15*(12), e2022MS003518. doi: 10.1029/2022MS003518

Lumpkin, R., & Flament, P. (2001). Lagrangian statistics in the central North Pacific. *Journal of Marine Systems*, *29*(1), 141–155. doi: 10.1016/S0924-7963(01)00014-8

Lévy, M., Jahn, O., Dutkiewicz, S., Follows, M. J., & d'Ovidio, F. (2015). The dynamical landscape of marine phytoplankton diversity. *Journal of The Royal Society Interface*, *12*(111), 20150481. doi: 10.1098/rsif.2015.0481

Lévy, M., Resplandy, L., & Lengaigne, M. (2014). Oceanic mesoscale turbulence drives large biogeochemical interannual variability at middle and high latitudes. *Geophysical Research Letters*, *41*(7), 2467–2474. doi: 10.1002/2014GL059608

Mak, J., Maddison, J. R., Marshall, D. P., Ruan, X., Wang, Y., & Yeow, L. (2023). Scale-Awareness in an Eddy Energy Constrained Mesoscale Eddy Parameterization. *Journal of Advances in Modeling Earth Systems*, *15*(12), e2023MS003886. doi: 10.1029/2023MS003886

Marques, G. M., Loose, N., Yankovsky, E., Steinberg, J. M., Chang, C.-Y., Bhamidipati, N., … Zanna, L. (2022). NeverWorld2: an idealized model hierarchy to investigate ocean mesoscale eddies across resolutions. *Geoscientific Model Development*, *15*(17), 6567–6579. doi: 10.5194/gmd-15-6567-2022

Marshall, D., & Adcroft, A. (2010). Parameterization of ocean eddies: Potential vorticity mixing, energetics and Arnold's first stability theorem. *Ocean Modelling*, *32*(3), 188–204. doi: 10.1016/j.ocemod.2010.02.001

Marshall, J., Scott, J. R., Romanou, A., Kelley, M., & Leboissetier, A. (2017). The dependence of the ocean's MOC on mesoscale eddy diffusivities: A model study. *Ocean Modelling*, *111*, 1–8. doi: 10.1016/j.ocemod.2017.01.001

McDougall, T. J., & Church, J. A. (1986). Pitfalls with the Numerical Representation of Isopycnal Diapycnal Mixing.

Montgomery, R. B. (1940). The Present Evidence on the Importance of Lateral Mixing Processes in the Ocean. *Bulletin of the American Meteorological Society*, *21*(3), 87–94.

Morrison, A. K., Waugh, D. W., Hogg, A. M., Jones, D. C., & Abernathey, R. P. (2022). Ventilation of the Southern Ocean Pycnocline. *Annual Review of Marine Science*, *14*(1), 405–430. doi: 10.1146/annurev-marine-010419-011012

Neumann, N. K., & Jones, C. S. (2025). Effects of Wind and Isopycnal Mixing on Southern Ocean Surface Buoyancy Flux and Antarctic Bottom Water Formation. *Geophysical Research Letters*, *52*(7), e2024GL112133. doi: 10.1029/2024GL112133

Nummelin, A., & Isachsen, P. E. (2024). Parameterizing Mesoscale Eddy Buoyancy Transport Over Sloping Topography. *Journal of Advances* *in Modeling Earth Systems*, *16*(3), e2023MS003806. doi: 10.1029/2023MS003806

Plumb, R. A., & Mahlman, J. D. (1987). The Zonally Averaged Transport Characteristics of the GFDL General Circulation/Transport Model. *Journal of the Atmospheric Sciences*, *44*(2), 298–327. doi: 10.1175/1520-0469(1987)044<0298:TZATCO>2.0.CO;2

Pradal, M.-A., & Gnanadesikan, A. (2014). How does the Redi parameter for mesoscale mixing impact global climate in an Earth System Model? *Journal of Advances in Modeling Earth Systems*, *6*(3), 586–601. doi: 10.1002/2013MS000273

Pudig, M. (2025). *mpudig/JAMES_isopycnalmixingbackscatter: Submission.* Zenodo. doi: 10.5281/zenodo.17088720

Redi, M. H. (1982). Oceanic Isopycnal Mixing by Coordinate Rotation. *Journal of Physical Oceanography*, *12*(10), 1154–1158. doi: 10.1175/1520-0485(1982)012<1154:OIMBCR>2.0.CO;2

Resplandy, L., Lévy, M., Madec, G., Pous, S., Aumont, O., & Kumar, D. (2011). Contribution of mesoscale processes to nutrient budgets in the Arabian Sea. *Journal of Geophysical Research: Oceans*, *116*(C11). doi: 10.1029/2011JC007006

Sijp, W. P., & England, M. H. (2009). The Control of Polar Haloclines by Along-Isopycnal Diffusion in Climate Models. *Journal of Climate*, *22*(3), 486–498. doi: 10.1175/2008JCLI2513.1

Silvestri, S., Wagner, G. L., Campin, J.-M., Constantinou, N. C., Hill, C. N., Souza, A., & Ferrari, R. (2024). A New WENO-Based Momentum Advection Scheme for Simulations of Ocean Mesoscale Turbulence. *Journal of Advances in Modeling Earth Systems*, *16*(7), e2023MS004130. doi: 10.1029/2023MS004130

Smith, K. S. (2005). Tracer transport along and across coherent jets in two-dimensional turbulent flow. *Journal of Fluid Mechanics*, *544*(-1), 133. doi: 10.1017/S0022112005006750

Smith, K. S., & Marshall, J. (2009). Evidence for Enhanced Eddy Mixing at Middepth in the Southern Ocean. *Journal of Physical Oceanography*, *39*(1), 50–69. doi: 10.1175/2008JPO3880.1

Solomon, H. (1971). On the Representation of Isentropic Mixing in Ocean Circulation Models. *Journal of Physical Oceanography*, *1*(3), 233–234. doi: 10.1175/1520-0485(1971)001<0233:OTROIM>2.0.CO;2

Steinberg, J. M., Cole, S. T., Drushka, K., & Abernathey, R. P. (2022). Seasonality of the Mesoscale Inverse Cascade as Inferred from Global Scale-Dependent Eddy Energy Observations. *Journal of Physical Oceanography*, *52*(8), 1677–1691. doi: 10.1175/JPO-D-21-0269.1

Stewart, A. L., & Thompson, A. F. (2015). Eddy-mediated transport of warm Circumpolar Deep Water across the Antarctic Shelf Break. *Geophysical Research Letters*, *42*(2), 432–440. doi: 10.1002/2014GL062281

Storer, B. A., Buzzicotti, M., Khatri, H., Griffies, S. M., & Aluie, H. (2022). Global energy spectrum of the general oceanic circulation. *Nature Communications*, *13*(1), 5314. doi: 10.1038/s41467-022-33031-3

Taylor, G. I. (1953). The dispersion of matter in turbulent flow through a pipe. *Proceedings of the Royal Society of London. Series A. Mathematical and Physical Sciences*, *223*(1155), 446–468. doi: 10.1098/rspa.1954.0130

Thompson, A. F., Heywood, K. J., Schmidtko, S., & Stewart, A. L. (2014). Eddy transport as a key component of the Antarctic overturning circulation. *Nature Geoscience*, *7*(12), 879–884. doi: 10.1038/ngeo2289

Thompson, A. F., & Young, W. R. (2006). Scaling Baroclinic Eddy Fluxes: Vortices and Energy Balance. *Journal of Physical Oceanography*, *36*(4), 720–738. doi: 10.1175/JPO2874.1

Tulloch, R., Ferrari, R., Jahn, O., Klocker, A., LaCasce, J., Ledwell, J. R., ... Watson, A. (2014). Direct Estimate of Lateral Eddy Diffusivity Upstream of Drake Passage. *Journal of Physical Oceanography*, *44*(10), 2593–2616. doi: 10.1175/JPO-D-13-0120.1

Uchida, T., Balwada, D., P. Abernathey, R., A. McKinley, G., K. Smith, S., & Lévy, M. (2020). Vertical eddy iron fluxes support primary production in the open Southern Ocean. *Nature Communications*, *11*(1), 1125. doi: 10.1038/s41467-020-14955-0

Veronis, G. (1975). The role of models in tracer studies. *Numerical Models of Ocean Circulation*, 133–146.

Vollmer, L., & Eden, C. (2013). A global map of meso-scale eddy diffusivities based on linear stability analysis. *Ocean Modelling*, *72*, 198–209. doi: 10.1016/j.ocemod.2013.09.006

Wei, H., & Wang, Y. (2021). Full-Depth Scalings for Isopycnal Eddy Mixing Across Continental Slopes Under Upwelling-Favorable Winds. *Journal of Advances in Modeling Earth Systems*, *13*(6), e2021MS002498. doi: 10.1029/2021MS002498

Whalen, C. B., MacKinnon, J. A., & Talley, L. D. (2018). Large-scale impacts of the mesoscale environment on mixing from wind-driven internal waves. *Nature Geoscience*, *11*(11), 842–847. doi: 10.1038/s41561-018-0213-6

Yankovsky, E., Bachman, S., Smith, K. S., & Zanna, L. (2024). Vertical Structure and Energetic Constraints for a Backscatter Parameterization of Ocean Mesoscale Eddies. *Journal of Advances in Modeling Earth Systems*, *16*(7), e2023MS004093. doi: 10.1029/2023MS004093

Yankovsky, E., Zanna, L., & Smith, K. S. (2022). Influences of Mesoscale Ocean Eddies on Flow Vertical Structure in a Resolution-Based Model Hierarchy. *Journal of Advances in Modeling Earth Systems*, *14*(11), e2022MS003203. doi: 10.1029/2022MS003203

Yassin, H., Marques, G. M., & Grooms, I. (2025). Balancing Backscatter and Diffusion in a 1/4° Forced Global Ocean Model. *Authorea Preprints*. doi: 10.22541/essoar.175700044.45098278/v1

Young, W. R. (2012). An Exact Thickness-Weighted Average Formulation of the Boussinesq Equations. *Journal of Physical Oceanography*, *42*(5), 692–707. doi: 10.1175/JPO-D-11-0102.1

Zhang, W., Griffies, S. M., Hallberg, R. W., Kuo, Y.-H., & Wolfe, C. L. P. (2024). The Role of Surface Potential Vorticity in the Vertical Structure of Mesoscale Eddies in Wind-Driven Ocean Circulations. *Journal of Physical Oceanography*, *54*(6), 1243–1266. doi: 10.1175/JPO-D-23-0203.1

Zhang, W., Kuo, Y.-H., Silvestri, S., Adcroft, A., Hallberg, R. W., & Griffies, S. M. (2025). A WENO finite-volume scheme for the evolution of potential vorticity in isopycnal ocean models. *Authorea Preprints*. doi: 10.22541/essoar.175339141.10871701/v1

Zhang, W., & Wolfe, C. L. P. (2022). On the Vertical Structure of Oceanic Mesoscale Tracer Diffusivities. *Journal of Advances in Modeling Earth Systems*, *14*(6), e2021MS002891. doi: 10.1029/2021MS002891

Zika, J. D., Sallée, J.-B., Meijers, A. J. S., Naveira-Garabato, A. C., Watson, A. J., Messias, M.-J., & King, B. A. (2020). Tracking the spread of a passive tracer through Southern Ocean water masses. *Ocean Science*, *16*(2), 323–336. doi: 10.5194/os-16-323-2020